Longitudinal Beam Dynamics and Longitudinal Matches in Energy Recovery Linacs

Gustavo Pérez Segurana

This thesis is submitted for the degree of

Doctor of Philosophy

Lancaster University

Physics Department

March 2021

Abstract

Longitudinal Beam Dynamics and Longitudinal Matches in Energy Recovery Linacs

Gustavo Pérez Segurana

In the design of particle accelerators, longitudinal beam dynamics plays a critical role in delivering beams with the desired properties to the interaction regions by controlling the energy distribution and current profile. Variable bunch compressors are therefore a fundamental tool to provide flexibility in any accelerator. This variability is implemented in the MAX IV bunch compressors employing variable strength dipoles capable of delivering high-quality beams with a wide range of available longitudinal dispersions.

Energy recovery linacs have the potential to outperform traditional linacs and storage rings by delivering simultaneously high brilliance beams at a high repetition rate. In an ERL, a self-consistent longitudinal match is not only necessary to optimize the beam delivered to the interaction regions but also to enable the energy recovery mechanism. We present a detailed study of self-consistent longitudinal matches for collider and FEL applications. We conclude that choosing common return transport beamlines severely restricts the availability of a self-consistent match, in particular when synchrotron radiation losses are important. Finally, we apply this method to two distinct projects: ER@CEBAF as a high energy ERL FEL driver and PERLE as a high-charge ERL for nuclear physics experiments.

Contents

1 Introduction **1**

1.1 MAX IV 5

1.2 CEBAF - Continuous Electron Beam Accelerator Facility 6

1.3 PERLE – Powerful Energy Recovery Linac Experiment 8

2 Theory **10**

2.1 Beam Dynamics 10

3 Variable bunch compressors in MAX-IV **19**

3.1 Introduction 19

3.2 Existing Fixed R_{56} Arc-Like Compressors 23

3.3 Additional Quadrupole Variable R_{56} Compressor 24

3.4 Additional Dipole Variable R_{56} Compressor 26

3.5 Comparison between the proposed solutions 32

3.6 Particle Tracking Studies 35

3.7 Conclusion 36

4 Longitudinal matches in ERLs **38**

4.1 Introduction 38

4.2 Definitions & Assumptions 39

4.3 Semi-analytic method 42

4.4 Compressive match 49

4.5 Compressive match with SR loss compensation 49

4.5.1 Separate Transport 50

4.5.2 Common Transport 51

4.6 Energy spread minimization 52

4.7 Energy Spread Minimization with SR loss compensation 56

4.7.1 Common Transport 56

4.7.2 Separate Transport 59

4.8 Bunch length control through alternate sign linearization 60

4.9 Strategies to mitigate common transport limitations 61

4.10 Parasitic crossings 64

4.11 Conclusions 68

5 Longitudinal beam dynamics in ER@CEBAF **70**

5.1 ER@CEBAF 70

5.2 Proposed modifications for a compressive match 71

5.2.1 rf phase 72

5.2.2 Injector chicane 75

5.2.3 Arc modifications 76

5.2.4 Longitudinal match 83

5.3 Experimental considerations 84

5.4 Conclusion 88

6 Longitudinal beam dynamics at PERLE **90**

6.1 Longitudinal match 90

6.1.1 On-crest match 91

6.1.2 Energy spread minimization 92

6.1.3 Injected bunch 95

6.2 Conclusion 97

7 Conclusions **99**

A ER@CEBAF arc optics **102**

List of Figures

1.1 From left to right, schematic diagrams of a single pass linac, recirculating linac, energy recovery linac and storage ring. 2

1.2 Electron energy E vs. electron source current I for classes of past, present and possible future ERL facilities. Dashed diagonal lines represent constant power, $P[\mathrm{kW}] = E[\mathrm{MeV}] \cdot I[\mathrm{mA}]$[3]. 3

1.3 Layout of the MAX IV linac. 5

1.4 Top and side views of PERLE. rf cavities in purple, dipoles in blue and quadrupoles in red. Reproduced from [34]. 8

2.1 Phase space distribution with an elliptical boundary highlighting the relationship of the ellipse geometry to the Twiss parameters. Reproduced from [35] 11

2.2 Projected emittance growth as a result of nonzero chromatic amplitude. Colour represents particles with the same energy deviation δ. 15

2.3 Common bunch compressor configurations, dipoles in blue and focusing elements in red. Top left, 4-Dipole "C" chicane; bottom left, 4-Dipole "S" chicane; top right, Double bend achromat (DBA); bottom right, Arc/FODO compressor. 16

2.4 Field lines for charges at different energies. 17

2.5 Diagram of a bunch in a curvilinear trajectory where radiation emitted from particles the back of the bunch reaches the particles in the head of the bunch. 18

3.1 Path length difference with respect to the design trajectory as a function of momentum deviation for uncorrected arc-like and chicane-like compressors showing their respective deviations from linearity. 21

3.2 Longitudinal phase space of chirped bunches for compression in an arc-like system and chicane-like. Ideal "linear" bunch, with curvature from the fundamental rf and effect of negative T_{566} shown. 21

3.3 Longitudinal phase space of chirped bunches with varying bunch length and rf phase before and after compression. 23

3.4 Layout of existing MAX IV Bunch Compressor 1. 24

3.5 Optics and first-, second- and third-order horizontal and longitudinal dispersion functions of existing MAX IV BC1. 25

3.6 Additional quadrupoles layout. Dipoles in black, quadrupoles in red and sextupoles in blue. New elements highlighted by arrows. 26

3.7 Optics, first-, second- and third-order longitudinal dispersion functions of additional quadrupole solution tuned to isochronous condition. 27

3.8 Horizontal momentum acceptance of the original, fixed design with chromatic corrections, variable with extra quadrupoles and variable with extra dipoles solutions. 28

3.9 Phase advance dependence on δ at the end of BC1 for the original lattice, extra quadrupoles and extra dipoles solutions. 28

3.10 Derivative of the phase advance with respect to δ at the end of BC1 for the original lattice, extra quadrupoles and extra dipoles solution. 29

3.11 Additional Dipoles layout. Dipoles in black, quadrupoles in red, sextupoles in blue and octupoles in light blue. New elements highlighted by arrows. 30

3.12 Schematic of new dipole with the original trajectory (solid) and different new trajectories for different R_{56} values. 30

3.13 Optics and first-, second- and third-order dispersion functions of isochronous MAX IV BC1 with additional dipoles. $R_{56} = 0\,\text{cm}$ $T_{566} = -4.0\,\text{cm}$ 33

3.14 Chromatic dependence of the beta and alpha functions at the end of BC1 for the original, fixed lattice, additional quadrupole and additional dipole solutions. 34

3.15 Beam emittance evolution in additional dipole and additional quadrupole configurations. 36

4.1 Simplest racetrack ERL configurations, blue cylinders represent the linacs, and the spiked ball represents the interaction region. Common transport and separate transport. 41

4.2 Linearization with harmonic cavities. 42

4.3 Classification of longitudinal matches for ERLs whose feasibility will be studied in this chapter. 48

4.4 Compressive match. Sequence of longitudinal phase space manipulations maximizing bunch current at interaction point. 50

4.5 Compressive match with SR loss compensation. 51

4.6 Longitudinal phase spaces of accelerating (solid) and decelerating (dashed) bunches in an intermediate arc. The required energy acceptance for common transport corresponds to the height of the black arrow. The required energy acceptance in the corresponding separate transport configuration corresponds to only the height of the red and blue arrows for the accelerating and decelerating arcs respectively. 52

4.7 rf beam load plots for different phase configurations in common transport longitudinal matches that minimize beam energy spread. 54

4.8 Energy spread minimization with common transport. Sequence of longitudinal phase space manipulations with two linearizing arcs with opposite sign of T_{566}. 55

4.9 Energy spread minimizing matches with non-isochronous intermediate arcs. 57

4.10 Arc 1 centroid energy difference between accelerating and decelerating beams for a range of accelerating and decelerating phases. Black dashed contour lines represent peak energy in GeV. 58

4.11 Energy spread minimizing match with SR loss compensation using separate transport. Applicable to e.g. LHeC. 60

4.12 Sequences of compressive common transport longitudinal matches with different choice of linearizing arcs. 62

4.13 Arc path length as a function of relative momentum deviation with only second order longitudinal dispersion non-zero. 63

4.14 Arc path length as a function of relative momentum deviation where we choose reference momentum, first, second and third order longitudinal dispersions allowing control over pathlength and R_{56} of two off-momentum beams. 64

4.15 Equivalent of Fig. 4.5 but bunch decompression does not occur at top energy. 65

4.16 Equivalent of Fig. 4.5 but with utilisation of a parasitic crossing and deceleration on opposite side of rf trough in order to remove linear chirp. . 66

4.17 Change in curvature as an example bunch undergoes a linear compression. 67

4.18 Longitudinal match solutions using parasitic crossings to cancel rf curvature in common transport. 67

4.19 Compressive longitudinal match with energy spread growth at the interaction point. 68

5.1 Schematic of the ER@CEBAF Layout. 71

5.2 Top energy arc phase shift as a function of accelerating phase such that accelerating and decelerating beams have the same energy in arc 1. Dashed lines correspond to solutions where beam chirp is not compensated during deceleration. 74

5.3 rf beam load plot for North and South linacs showing phase choices during acceleration (black), deceleration (red), and resultant/10 (blue) such that beam energies are matched during acceleration and deceleration. Number labels indicate the order of the linac passes. 75

5.4 CEBAF's injector chicane layout with additional sextupoles. Dipoles in black, quadrupoles in red and sextupoles in blue. 77

5.5 Second-order horizontal and longitudinal dispersions in the CEBAF's injector chicane with and without additional sextupoles. 77

5.6 Initial (dashed) and reduced dispersion configuration (solid), first and second-order dispersions and optics (top, middle and bottom respectively) of CEBAF's Arc 1. 78

5.7 Initial (dashed) and reduced dispersion configuration (solid), first and second-order dispersions and optics (top, middle and bottom respectively) of CEBAF's Arc 4. 79

5.8 Initial (dashed) and reduced dispersion configuration (solid), first and second-order dispersions and optics (top, middle and bottom respectively) of CEBAF's Arc 5. 80

5.9 Initial (dashed) and reduced dispersion configuration (solid), first and second-order dispersions and optics (top, middle and bottom respectively) of CEBAF's Arc 9. 81

5.10 Initial (dashed) and reduced dispersion configuration (solid), first and second-order dispersions and optics (top, middle and bottom respectively) of CEBAF's Arc 10. 82

5.11 Tracked bunch longitudinal phase space, prediction of the tracked bunch from semianalytical model (black line) and semianalytical prediction after preliminary second order corrections (red line). 84

5.12 Example use of multiple short bunches to emulate a longer bunch. 85

5.13 Start to end comparison of horizontal dispersion η_x (top) and vertical dispersion η_y (bottom) between original and reduced dispersion configurations. 86

5.14 Mean beam momentum as it traverses the top energy arc. Energy lost corresponds to SR. Overlayed magnet lattice with dipoles as boxes and quadrupoles in red. 86

5.15 Arc 10 horizontal centroid deviation due to dipole common power supply, energy lost to SR and random quadrupole misalignments with amplitude of 200 µm. 87

5.16 Arc 9 horizontal centroid deviation due to dipole common power supply, energy lost to SR and random quadrupole misalignments with amplitude of 200 µm. 88

6.1 Longitudinal phase spaces of (a) assumed initial bunch and (b) bunch at the interaction regions showing the curvature acquired during acceleration. 91

6.2 Longitudinal phase space necessary at the injector to compensate for rf curvature at the interaction regions and final longitudinal phase space after deceleration at the dump in an on-crest longitudinal match. 92

6.3 rf beam load diagram of linacs 1 and 2 with phase choices during acceleration, deceleration, and resultant rf load. 93

6.4 Deviation from integer number of wavelengths of arc path lengths as a function of the deviation of arc 1 to achieve the phase scheme of Fig. 6.3. 93

6.5 Longitudinal phase spaces at the interaction region and dump for different combinations of linearizing T_{566} in arcs 1 and 4, with line indicating a continuous set of solutions available. 94

6.6 rf beam load plots for linacs 1 and 2 for a longitudinal match with a non-isochronous arc 1 showing phase choices during acceleration, deceleration, and 10x resultant. 95

6.7 Sequence of longitudinal phase spaces of a longitudinal match with a slight compression in Arc 1. 96

6.8 Longitudinal phase space of tracked bunch at the exit of the first linac accelerated 15 deg off-crest, with red line representing a third-order polynomial fit and deviations from fit line. 97

A.1 Initial (dashed) and reduced dispersion configuration (solid), first and second-order dispersions and optics (top, middle and bottom respectively) of CEBAF's Arc 2. 103

A.2 Initial (dashed) and reduced dispersion configuration (solid), first and second-order dispersions and optics (top, middle and bottom respectively) of CEBAF's Arc 3. 104

A.3 Initial (dashed) and reduced dispersion configuration (solid), first and second-order dispersions and optics (top, middle and bottom respectively) of CEBAF's Arc 6. 105

A.4 Initial (dashed) and reduced dispersion configuration (solid), first and second-order dispersions and optics (top, middle and bottom respectively) of CEBAF's Arc 7. 106

A.5 Initial (dashed) and reduced dispersion configuration (solid), first and second-order dispersions and optics (top, middle and bottom respectively) of CEBAF's Arc 8. 107

List of Tables

1.1 PERLE Beam Parameters 9

3.1 Magnet parameters for MAX IV BC1 with additional dipoles. We choose as an example the first-order isochronous, second-order linearized solution: $R_{56} = 0\,\text{cm}$ $T_{566} = -4.0\,\text{cm}$ 32

4.1 Numerical optimization of arc path lengths and initial rf phases that minimize the difference in fractional momentum between accelerating and decelerating beams traversing the same arcs of a LHeC-like machine. 59

5.1 ER@CEBAF machine parameter list, adapted from [13]. 70

5.2 ER@CEBAF beam parameter list, adapted from [13]. 71

5.3 Pass-by-pass beam energies for ER@CEBAF. All energies in MeV. ΔE is energy lost to SR in each arc. Adapted from [13]. 73

5.4 Pass-by-pass beam energies for ER@CEBAF. Arc path lengths adjusted to match accelerating and decelerating energies. On crest energy gain set to 700 MeV 76

5.5 Alternative longitudinal match solutions employing different arcs. 83

6.1 First-, second- and third-order longitudinal dispersions of each of the PERLE arcs. Arc 6 is split into spreader, arc and recombiner sections as interaction regions are placed between these. 91

Acknowledgements

I would like to thank my supervisors Ian Bailey and Peter Williams, for their support, initiative and guidance. Through these difficult times none of this work would have been possible without them.

My thanks also go to the rest of the AP group at Daresbury Laboratory, for their willingness to have discussions and being always available. To the collaborators at MAX IV, Jefferson Lab and IJCLab for welcoming our contributions and in particular to Alex Bogacz for his enthusiasm in our project and his support in extending the scope of our work.

I would also like to thank all my colleges at the Cockcroft Institute and Ben, Bianca, Dan, Liam, Pavel, Ruth, Steve, thank you for always being able to put a smile on my face. Special thanks to Hannah, Harry and Joe, thank you keeping me sane and making Liverpool a place to call home.

Last, but not least, I thank all my family for always encouraging me and their unconditional support.

Thank you.

Declaration

This thesis is my own work and it has not been submitted for the award of a higher degree elsewhere. The sections of the thesis that have been published have been clearly identified. Where other sources of information have been used, they have been acknowledged.

Chapter 1

Introduction

Modern particle accelerators are used in many different fields, from high energy particle colliders, to light sources and medical applications. This wide range of applications can only be catered for with a wide range of beam parameters at the interaction points. There is however a general trend towards continuous-wave, high average current, short pulses, low emittances and small energy spreads. All these parameters contribute towards an increased luminosity. Schematics of different archetypes of accelerators are depicted in Fig. 1.1.

A logical approach to increase the luminosity output from an accelerator is to repeatedly recirculate the accelerated beam through the interaction point. This approach is the defining feature of storage rings. However, storage ring facilities are currently near their theoretical performance limit as an equilibrium system. Transversely accelerated electrons emit synchrotron radiation. Therefore, to achieve equilibrium, energy must be resupplied to the circulating electrons with rf cavities. In this equilibrium, the beam emittance is determined by the balance between damping and excitation due to the emission of synchrotron radiation and it is larger than the available from the injector.

In order to circumvent the storage ring limitations, we can use linear accelerators, linacs. The beam quality in a linac is determined by the source. Additionally, since the beam is

not in an equilibrium state, its longitudinal phase space distribution can be manipulated and therefore tailored to a specific application. However, as a single pass machine, there is a heavy reliance on the source to provide a beam of low emittance and high average current. Finally, since many applications require the beams to be accelerated to high energies, the average beam current must be kept low to dump the beam safely and limit the power required to operate them.

Recirculating linacs are accelerators without an equilibrium orbit, but, as in a storage ring, the beam traverses the accelerating cavities multiple times [1]. The usual motivation for beam recirculation in the form of recirculating linacs is economical. Beam recirculation systems are usually cheaper than additional rf linac length, motivating the reutilization of a given rf installation as many times as possible to achieve the highest possible energy.

Energy recovery linacs, ERLs, were first proposed in 1965 [2]. ERLs eliminate the power limitation from linacs by reinjecting the already spent beam into the linac with a phase shift such that the beam is now decelerated and its energy is deposited into the cavities where it can be reused to accelerate the following bunches. As a consequence of the beam deceleration, a low energy beam is dumped. Therefore, an ERL recirculates the beam energy rather than the beam itself and this is what allows for a simultaneous combination of high current and high bunch phase space density.

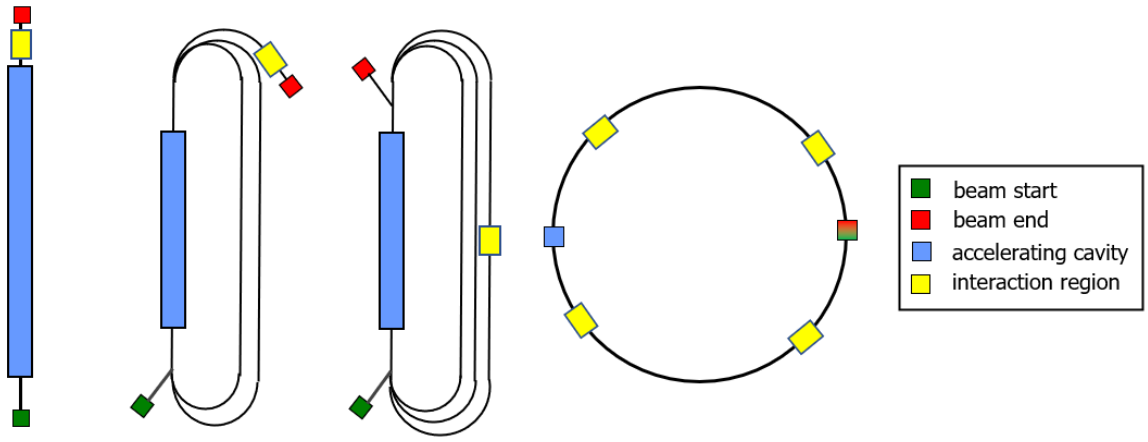

Figure 1.1: From left to right, schematic diagrams of a single pass linac, recirculating linac, energy recovery linac and storage ring.

Figure 1.2 shows an overview of the current state of the art between completed, ongoing and proposed electron facilities as an interaction energy vs. source current plot with diagonal lines as constant beam power lines.

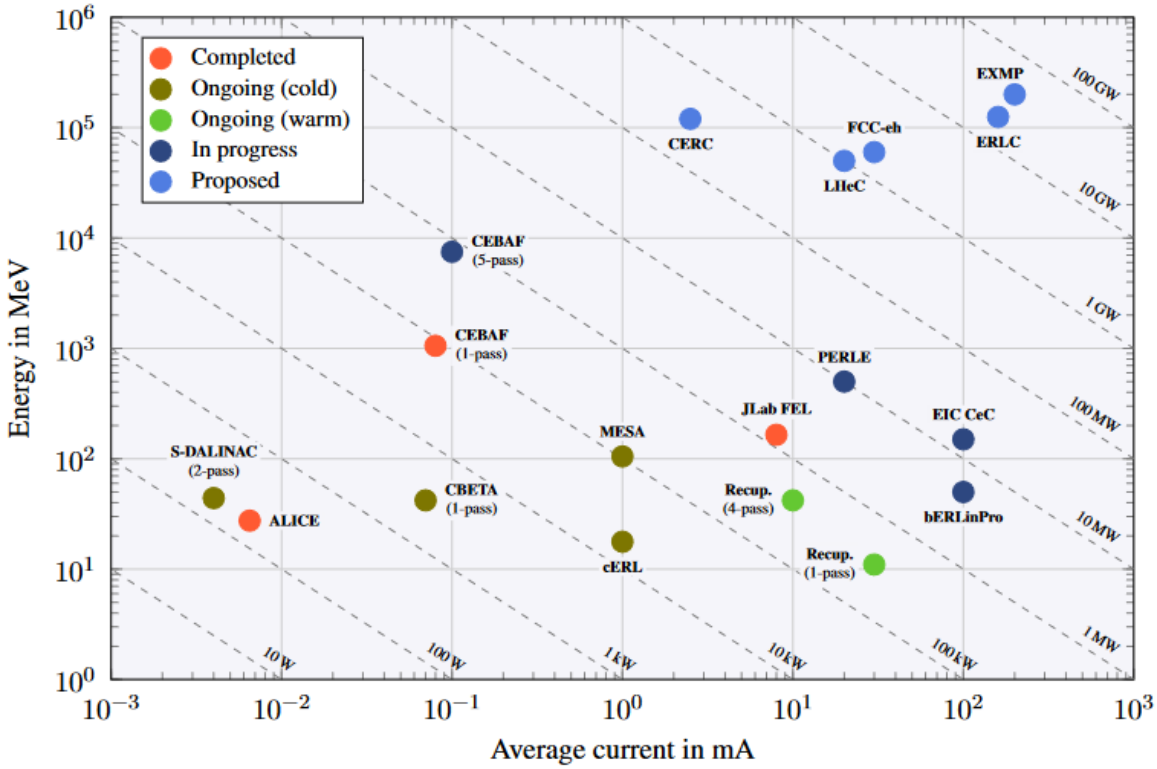

Figure 1.2: Electron energy E vs. electron source current I for classes of past, present and possible future ERL facilities. Dashed diagonal lines represent constant power, $P[\mathrm{kW}] = E[\mathrm{MeV}] \cdot I[\mathrm{mA}]$[3].

The three completed ERL facilities are: ALICE at Daresbury [4], the first European ERL facility; CEBAF (1-pass) [5], with the highest energy reached of 1 GeV; and the JLab FEL [6], with the highest current, 10 mA, of the SRF ERLs, although higher currents have been achieved in the normal-conducting ERL facility at BINP [7].

The ongoing superconducting ERL facilities include the operational S-DALINAC at Darmstadt [8], CBETA at Cornell [9] and the compact ERL (cERL) at KEK in Japan [10, 11] as well as MESA at Mainz [12] which is expected to have beam in the near future.

The facilities that fall in the in-progress classification have the goals of reaching higher energy in multiple turns (CEBAF-5 pass [13]) or high current (bERLinPro [14] and the

coherent electron cooler, CeC at the EIC [15]). PERLE [16] instead is designed to be medium-current, with three-turn operation up to 500 MeV beam energy.

Finally, five concept ERL applications are shown: CERC (Circular Energy Recovery Collider) [17], LHeC(Large Hadron electron Collider) [18], FCC-eh (Future Circular Collider in electron-hadron mode)[18], ERLC (Energy-Recovery Linear Collider) [19] and EXMP (Electrons and X-rays to Muon Pair) [20] which push the energy frontier and rely on the knowledge acquired from the ongoing and planned facilities.

Applications of ERLs span particle and nuclear physics as well as industry. The high intensity and small emittance properties of ERLs enable higher than current sensitivity measurements of fundamental physics employing for example internal gas targets [21]. Properties of unstable nuclear matter can be explored with intense electron beams, which is one of the objectives for PERLE. Amongst the industrial applications, an ERL-based FEL driven by a 40 GeV beam (LHeC parameters) would provide a peak brilliance of the order of the European XFEL, but with orders of magnitude higher average brilliance [22]. An ERL with around 1 GeV electron beam energy would be capable of driving an FEL producing extreme-ultraviolet light, of particular interest for the semiconductor industry which uses photolithography. Finally, inverse Compton scattering (ICS) processes are highly relevant to medical and nuclear physics. A 1 GeV energy ERL with a high average current is capable of driving a high-flux, narrow-band gamma source.

Some of the main complications added to ERLs when compared to linacs are [23]:

- The merger of the injected low energy beam into the ERL loop without emittance growth.
- Separation and dump of the beam after successful energy recovery.
- Multi-pass, multi-turn beam instabilities.
- Construction of a self-consistent longitudinal match from injector to dump.

In this thesis, we first lay out the theoretical framework of beam dynamics with a focus on

longitudinal beam dynamics in chapter 2 that will be used throughout this work as well as outlining the problems of finding a self-consistent longitudinal match in ERLs. In chapter 3 we explore the redesign of the MAX IV bunch compressors with a focus on the longitudinal beam dynamics. This acts as an illustrative example of the range of issues that need to be considered when manipulating the longitudinal phase space of particle bunches in a practical accelerator design. In chapter 4 we present the novel semi-analytical method we have developed to explore and evaluate longitudinal matches in ERLs, which is then applied in chapter 5 to ER@CEBAF and subsequently in chapter 6 to PERLE.

In the following sections we introduce the facilities featured in this thesis.

1.1 MAX IV

MAX IV is primarily a near-diffraction-limited (or fourth generation) storage ring facility utilising full energy injection from an S-band linac [24] into two rings, one at 1.5 GeV and a second at 3 GeV. It was foreseen at the design stage that this linac could also drive spontaneous undulator radiation in a Short Pulse Facility (SPF), and be adapted in the future to drive a soft X-ray FEL. In order to generate a high peak current, longitudinal phase space linearization is necessary for both applications. The implementation of arc-like compressors achieves this without the need for expensive harmonic rf, the disadvantages being the transverse displacement of the beamline sections on either side of each compressor and the fixed R_{56}. The location of the compressors within the linac are shown in Fig. 1.3.

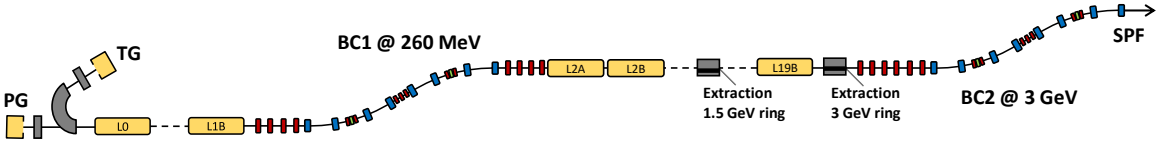

Figure 1.3: Layout of the MAX IV linac. Bunch compressor 1 (BC1) is located at 260 MeV. Extractions to the 1.5 and 3.0 GeV rings are at the exit of acceleration sections 2 & 3 respectively. BC2 is located at 3.0 GeV and feeds a short-pulse facility (SPF) and future soft X-ray FEL.

The MAX IV storage rings and SPF were completed in 2016 and approval has been given for a detailed design of a soft X-ray FEL [25, 26]. Experience at FEL facilities in the interim period has highlighted the importance of variability in the R_{56} of the compressors. The inclusion of this R_{56} variability in the compressors is explored in chapter 3.

1.2 CEBAF - Continuous Electron Beam Accelerator Facility

CEBAF, with construction starting on February 13, 1987 [27], has served the nuclear physics research community since 1995. It was conceived originally as providing a 4 GeV, 200 µA, continuous electron beam, with the purpose of studying the structure for the nuclear many-body system, its quark substructure and the strong and electro-weak interactions.

To achieve these objectives, CEBAF had to provide electron beams of sufficient:

- Energy to provide the kinematic flexibility required to study the transition region;
- Intensity (current) to allow precise measurement of small electromagnetic cross-sections;
- Duty factor to detect hadronic components emitted from the nucleus in coincidence with the scattered electron;
- Beam quality and resolution to allow detailed probing of the nuclear structure.

This combination of high energy, high current, high duty factor and beam quality would make CEBAF the world's most powerful microscope for studying the nucleus.

In the following years, the initial design was upgraded, reaching 6 GeV operation in 2000 and a further design upgrade to 12 GeV starting in 2001 [1], with the shift from 6 GeV

to 12 GeV starting in 2012, and with the first batch of electrons delivered at 12 GeV in 2016 [28].

With all this experience, CEBAF is a clear candidate to explore other applications of SRF technology such as a multipass ERL driven continuous-wave XFEL as an alternative to a dedicated linac design, reducing its cost and achieving high average power.

There is a history of similar proposals and experiments:

- **GERBAL** (2001) – A "Generic Energy Recovering Bisected Asymmetric Linac" as an FEL and SR source [29].
- **CEBAF-ER** (2003) – A successful GeV-scale energy recovery demonstration [5].
- **UK New Light Source** – A design study that considered 2-pass recirculation for a soft XFEL (1 keV) at 1 MHz [30].
- **CEBAF-X** (2014) – A design study to add a soft XFEL to CEBAF with a proposed 3-pass recirculation for hard XFEL [31].

This programme has very high synergy with the UK physics community's interests on UK-XFEL [32], as well as applications of ERLs to high energy physics as in the case of LHeC [18].

ER@CEBAF, the current energy recovery project on CEBAF, is therefore a very compelling project because it would become the first facility to have the energy reach to demonstrate ERL performance in the multi-GeV range. This scaling of energy recovery to multi-GeV energies encounters incoherent synchrotron radiation induced energy loss. It presents an invaluable opportunity for multi-pass beam break-up studies, and enables the experimental exploration of multi-pass, multi-GeV energy recovery.

1.3 PERLE – Powerful Energy Recovery Linac Experiment

PERLE is a proposed ERL facility [16] to test choices for a 50 GeV ERL which could provide electrons to an IP within the LHC called LHeC, or an IP within an FCC hadron ring called FCC-eh [18], and to host dedicated nuclear and particle physics experiments. Its primary objective is to test continuous wave (CW), high current, multipass energy recovery operation. With its target beam power of 10 MW, PERLE presents itself as a bridge between the current 1 MW ERLs and proposed future 100 MW accelerators.

As presently envisaged, PERLE is a common transport ERL arranged in a racetrack configuration with three recirculating arcs on each side stacked vertically as shown in Fig. 1.4. The arcs have a Flexible Momentum Compaction (FMC) lattice design [33] which provides a natural tuning 'knob' for their R_{56}. Injection into the first linac is done at 7 MeV and the target top energy is 500 MeV. Relevant beam parameters are summarized in table 1.1.

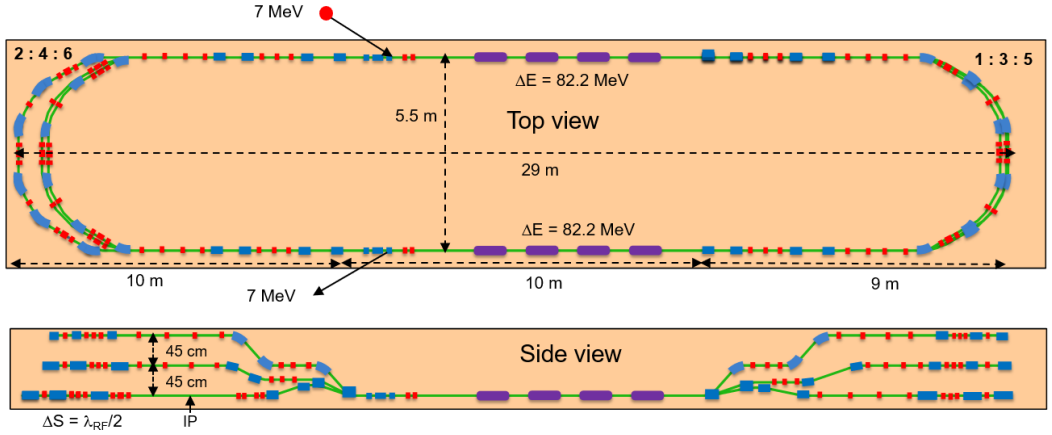

Figure 1.4: Top and side views of PERLE. rf cavities in purple, dipoles in blue and quadrupoles in red. Reproduced from [34].

Table 1.1: PERLE Beam Parameters

Parameter	Value	Units
Injector beam energy	7	MeV
Peak beam energy	500	MeV
Average beam current	20	mA
Bunch charge	500	pC
Bunch length (σ_s)	3	mm
rf frequency	801.5	MHz

Chapter 2

Theory

2.1 Beam Dynamics

When considering the beam as a distribution, the volume in 6-D space it occupies is its emittance, ϵ. The projections of this emittance onto the (x,p_x), (y,p_y) and (z,p_z) planes correspond to the horizontal, vertical and longitudinal emittances respectively. The beam emittance together with the β-function, $\beta(s)$, describe the evolution of the beam envelope along the beamline. The β-function together with $\alpha(s) \equiv -\beta'(s)/2$ and $\gamma \equiv \frac{1+\alpha^2}{\beta}$ are the Twiss functions and $\nu = \int \frac{ds}{\beta(s)}$ is known as the phase advance[1]. A visual representation of the beam emittance and Twiss parameters is shown in Fig.2.1.

Following Liouville's theorem, the six-dimensional (x, p_x, y, p_y, z, p_z) phase space volume that the beam occupies is constant as long as there are no dissipative forces, no Coulomb scattering between particles and no particles are created or lost. Additionally, if the forces in the three orthogonal planes are not coupled, the emittances are also constant in each of the planes. We can define the **rms emittance** as a function of the second moments

[1]When dealing with cyclic accelerators one can also find ψ or μ as symbols for phase advance and $\nu = \frac{1}{2\pi} \oint \frac{ds}{\beta(s)}$ as the tune.

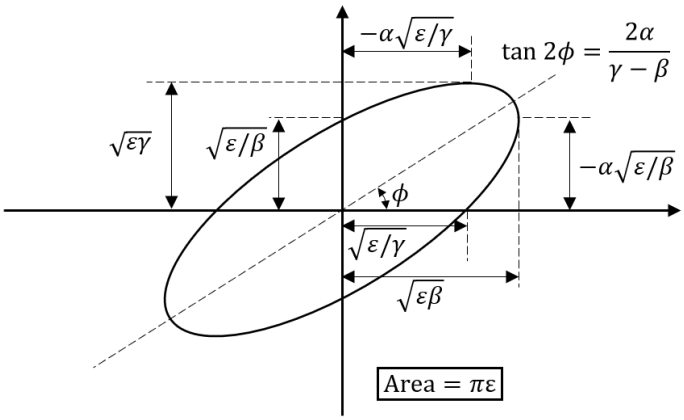

Figure 2.1: Phase space distribution with an elliptical boundary highlighting the relationship of the ellipse geometry to the Twiss parameters. Reproduced from [35]

of the distribution, which for the (x, x') plane is

$$\epsilon_{rms} = \sqrt{\sigma_x^2 \sigma_{x'}^2 - \sigma_{xx'}^2} = \sqrt{(\langle x^2 \rangle \langle x'^2 \rangle - \langle x x' \rangle^2)}\,, \tag{2.1}$$

with $x' = p_x/p$ and equivalently for the vertical and longitudinal planes. For a beam that undergoes acceleration, the **rms normalized emittance** is normally used, which depends on the transverse momentum instead of the divergence. For the horizontal plane,

$$\begin{aligned} \epsilon_{n,rms} &= \frac{1}{m_0 c} \sqrt{\sigma_x^2 \sigma_{p_x}^2 - \sigma_{x p_x}^2} \\ &= \frac{1}{m_0 c} \sqrt{(\langle x^2 \rangle \langle p_x^2 \rangle - \langle x p_x \rangle^2)} \\ &= \sqrt{(\langle x^2 \rangle \langle (\beta\gamma x')^2 \rangle - \langle x \beta\gamma x' \rangle^2)} \end{aligned} \tag{2.2}$$

Normalized emittance is preferred since the divergence of a particle $x' = p_x/p$ reduces during acceleration as p increases. However, this does not affect the normalized emittance. For relativistic particles $(\beta = 1)$,

$$\epsilon_{n,\mathrm{rms}}^2 = \langle \gamma^2 \rangle \left(\sigma_\gamma^2 \sigma_x^2 \sigma_y^2 + \epsilon_{\mathrm{rms}}^2 \right) . \tag{2.3}$$

For conventional accelerators, the first term in the parentheses of Eq.2.3 is negligible resulting in the commonly used relation $\epsilon_{n,\mathrm{rms}} = \langle \gamma \rangle \epsilon_{\mathrm{rms}}$. However, with the large energy spreads common in-plasma accelerated beams this additional approximation may no longer

hold [36, 37].

In addition to the emittance of their beams, accelerators are often characterised in terms of their useful outputs. If we are interested in radiation generation, we talk about brightness and it corresponds to the number of photons emitted per unit of time from a certain area into a certain solid angle and usually within a certain bandwidth. If instead two beams are colliding, the objective is to focus the beams into the smallest possible size at the interaction point to maximize the probability of interaction. In this case we are interested in the beam luminosity $\mathcal{L}$, defined such that the product of luminosity and the cross section of interaction σ, gives the number of events per unit of time.

Having considered the main characteristics of the accelerators, we now turn our attention to introducing useful concepts for developing accelerator designs.

The motion of individual charged particle through magnetic elements can be represented with matrix multiplication. A particle can be represented by a (column) vector $X(s)$, with $X^T(s) = (x(s), x'(s), y(s), y'(s), z(s), \delta(s))$ at a position s along the reference trajectory, where x and y are the horizontal and vertical displacements with respect to the reference trajectory; x' and y' are dx/ds and dy/ds, the angle this trajectory makes in the horizontal and vertical planes; z is the path length difference between the trajectory and the reference trajectory; and $\delta = \Delta p/p$ is the relative momentum deviation from the reference particle. The central trajectory is therefore defined as that with initial conditions $X(0) = 0$.

A particle in a bunch is transformed as,

$$X_i(s) = X_i(0) + \sum_{j=1}^{6} R_{ij} X_j(0) + \sum_{j,k=1}^{6} T_{ijk} X_j(0) X_k(0) + \sum_{j,k,l=1}^{6} U_{ijkl} X_j(0) X_k(0) X_l(0) + \dots , \tag{2.4}$$

where i is the component index of the vectors, $X(0)$ and $X(s)$ are the initial and final coordinates respectively and R_{ij}, T_{ijk} and U_{ijkl}, are the first, second and third-order transfer matrices respectively[2]

[2]In the literature one may find different symbols for third- and higher-order terms, but they can be unequivocally identified by the number of subscripts.

From the matrix elements of equation 2.4 we can identify the dispersion elements as those which transform the particles coordinates as a function of the momentum deviation. In this way, R_{16}, R_{36} and R_{56} are also known as the first-order horizontal, vertical and longitudinal dispersions. Similarly, T_{i66} and U_{i666} correspond to second- and third-order dispersions.

A lattice or a section of a lattice with $R_{i6} = 0$ for $i = 1..4$ is a first-order achromat. This means that a particle's coordinates in the transverse planes do not depend on (to first order) its momentum deviation from the reference particle. Similarly, second-, third- and higher-order achromats correspond to the degree to which the transport map of the transverse coordinates is not dependent on δ. If instead, we refer to the map of the longitudinal position as a function of momentum deviation, the property of a lattice with R_{56}, T_{566}, U_{5666}, ... $= 0$ is called isochronicity.

Terms that do not include a 6 as one of their subscripts are known as **geometric** terms or aberrations. Meanwhile, terms with one or more subscripts equal to 6 are commonly referred to as **chromatic** terms or aberrations, since their effect depends on the momentum deviation δ of the particle [38].

Magnetic fields are usefully expressed by a multipole expansion around the reference trajectory. Eqn. 2.5 shows an expansion of the vertical field as a function of horizontal displacement x where n, β and γ are functions of s and $h = 1/\rho$ with ρ being the radius of the reference trajectory.

$$\begin{aligned} B_y(x,0,s) &= B_y(0,0,s)(1 - nhx + \beta(hx)^2 + \gamma(hx)^3 + \dots) \\ &= B\rho(h - nh^2x + \beta h^3x^2 + \gamma h^4x^3 + \dots) \\ &= B\rho \sum_{n=0}^{\infty} k_n(s)x^n \,, \end{aligned} \tag{2.5}$$

with the multipole strength factors $k_0 = h$, $k_1 = -nh^2$ $k_2 = \beta h^3$, ... and where $B\rho = B/h = p_0/e$ is the magnetic rigidity of a particle of charge e and momentum p_0 along the reference trajectory. In such an expansion the dipole term is that which

is constant. The quadrupole field is proportional to the first derivative of the field with respect to the transverse coordinates, the second derivative is the sextupole term, etc. Consequently, dipoles and sextupoles are classed as even magnets whereas quadrupoles and octupoles are classed as odd magnets.

A particle is not moving through the center o f a quadrupole, it is affected by a force which is focusing in one transverse plane and defocusing in the other. Therefore, in order to confine the beam transverse dimensions, multiple quadrupoles are required. Additionally, if a quadrupole is placed in a dispersive region, it affects the dispersion as well as the optical functions. The focusing effect of a quadrupole depends on the particle momentum. This makes the optic functions momentum dependent that can be compensated by using sextupole magnets. Additionally, in a dispersive region, sextupoles are often used to manipulate higher order dispersions.

When studying the transport and manipulation of bunches with large energy spread it's often useful to study the chromatic amplitude function [39, 40],

$$W \equiv \sqrt{\left(\frac{\partial\alpha}{\partial\delta} - \frac{\alpha}{\beta}\frac{\partial\beta}{\partial\delta}\right)^2 + \left(\frac{1}{\beta}\frac{\partial\beta}{\partial\delta}\right)^2}. \tag{2.6}$$

The chromatic amplitude quantifies the linear chromatic error of the beam as a distribution and therefore the energy dependence of the focusing as it includes the chromatic derivatives of the Twiss parameters $\partial\alpha/\partial\delta$ and $\partial\beta/\partial\delta$. The property $W = 0$ is denominated apochromaticity. Deviations from apochromaticity result in increased projected emittances as shown in a schematic in Fig. 2.2 where 'beam slices' of varying energy have a different distribution in phase space.

In most accelerators, radiofrequency (rf) cavities are used to accelerate the particles in a bunch. Assuming that the particles are ultra-relativistic, so that all particles effectively travel at the same speed, c, such that the value of the longitudinal coordinate is constant (R_{5i}=0), the final energy deviation $\delta(s_1)$ is related to the initial energy deviation $\delta(s_0)$ as

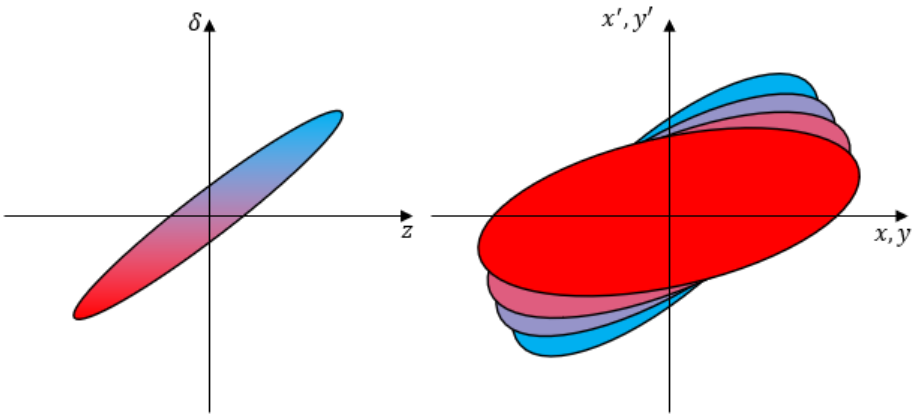

Figure 2.2: Projected emittance growth as a result of nonzero chromatic amplitude. Colour represents particles with the same energy deviation δ.

$$\delta(s_1) = \delta(s_0) + \frac{qV_{\mathrm{rf}}}{E_0} \cos\left(\frac{\omega_{\mathrm{rf}} z(s_0)}{c} + \theta_{\mathrm{rf}}\right) , \tag{2.7}$$

where q is the charge of the particle, V_{rf} is the cavity voltage, ω_{rf} is the rf frequency, θ_{rf} is the rf phase and E_0 is the reference energy [3]. By expanding eq. 2.7 around the longitudinal coordinate z we can extract the terms R_{65}, T_{655}, U_{6555}, ... from eq. 2.4. If θ_{rf} is not 0 the acceleration is off-crest. Off-crest passes through an rf cavity result in a non-zero R_{65} resulting in a linear correlation of the longitudinal position of the particles in the bunch and their momentum deviation, $(\frac{\partial \delta}{\partial s})$; this is a chirped bunch. Moreover, the higher order terms correspond to the impression of the rf curvature onto the longitudinal bunch profile (z, δ).

A bunch compressor manipulates the longitudinal phase space distribution of a bunch, often to increase its peak current by reducing the bunch length. This is particularly relevant in free-electron lasers, which require a high peak current to operate. However, at low energies, a bunch with high peak currents is vulnerable to collective effects that will degrade the beam quality. Therefore it is common to generate long bunches at the source and compress them once the beam is at high energy.

[3] Throughout this report we'll employ the convention where on crest acceleration occurs at zero degrees. The other commonly used alternative convention is that where zero degrees represent the zero crossing with positive slope and in eq. 2.7 the $\cos$ term is substituted by a $\sin$ term.

The magnetic bunch compression process relies on the dispersion that is generated in a dipole magnet. A sequence of dipoles and other focusing elements can be formed such that particles with different energies travel different path lengths. This corresponds to the R_{56}, T_{566}, U_{5666}, ... elements from eq. 2.4. Common bunch compressors are pictured in Fig. 2.3.

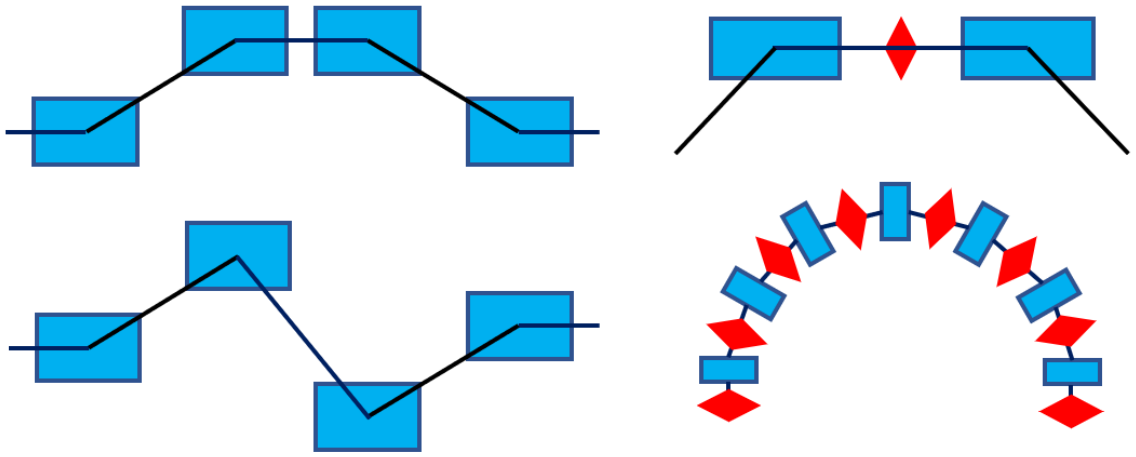

Figure 2.3: Common bunch compressor configurations, dipoles in blue and focusing elements in red. Top left, 4-Dipole "C" chicane; bottom left, 4-Dipole "S" chicane; top right, Double bend achromat (DBA); bottom right, Arc/FODO compressor.

Although called bunch 'compressors', the bunch length is only reduced if the bunch already has an appropriate chirp. If compression is achieved when the head of the bunch enters the system at lower energy than the centroid, and the tail of the bunch has higher energy, we label it "chicane-like" and combine it with pre-acceleration of the bunch on the rising side of the rf waveform. If the opposite is true we label the system "arc-like" and combine it with pre-acceleration of the bunch on the falling side of the rf waveform (or equivalently with the natural chirp produced by the space-charge force). Additionally, focusing elements can be used to tune the longitudinal dispersions of the bunch compressor. Varying the strength of these quadrupoles changes the value of the dispersion as it reaches the following dipole, thereby changing the R_{56} generated via the expression,

$$R_{56} = -\int \frac{R_{16}}{\rho} ds \,, \tag{2.8}$$

where ρ is the bending radius of the reference trajectory, and R_{16} is the linear horizontal

dispersion. It should be noted that if the beam trajectory is bent vertically instead, the vertical dispersion, R_{36}, should be used instead.

The second-order longitudinal dispersion [4] is generated as [41],

$$T_{566} = -\int \left[\frac{R_{26}^2}{2} + \frac{T_{166}}{\rho}\right] ds \tag{2.9}$$

and therefore can be tuned by placing quadrupoles and sextupoles in dispersive sections.

Other effects that play an important role in longitudinal beam dynamics in different circumstances are velocity bunching, longitudinal space-charge (LSC) and coherent synchrotron radiation (CSR). At low beam energies, where ultra-relativistic approximations cannot be applied, different energies can correspond to significant differences in velocity. This can be exploited to do compression in non-dispersive sections. LSC describes the transfer of energy from the tail of the bunch to the front of the bunch. For a perfectly conducting wall, the longitudinal space-charge field is

$$E_s = \frac{e}{4\pi\epsilon_0}\left(1 + 2\ln\frac{b}{a}\right)\frac{1}{\gamma^2}\frac{\partial\lambda}{\partial s}\,, \tag{2.10}$$

where ϵ_0 is the vacuum permittivity, b is the radius of the vacuum pipe, a is the beam radius with longitudinal density modulation $\lambda(s)$. The $1/\gamma^2$ dependence makes this effect decrease strongly at higher energies. A representation of the changes due to the relativistic Lorentz contraction along the direction of motion is shown in Fig 2.4. When a bunch of

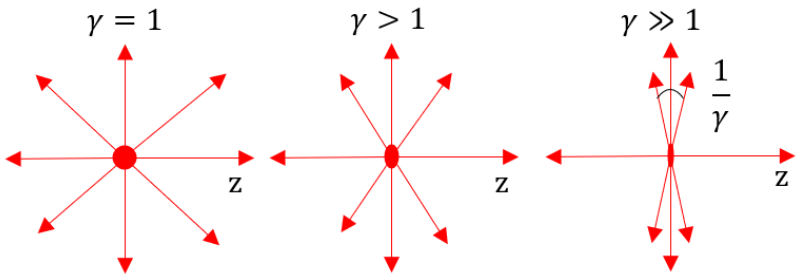

Figure 2.4: Field lines for charges at different energies.

[4] Care should be taken when deriving this expression. Premature truncation of the power series expansions of the coordinates results in an erroneous additional R_{16} term. This cancels exactly on retention of the next highest order terms.

charged particles emits radiation, the energy of the electromagnetic field is taken from its kinetic energy. This CSR wake is generated when the beam is moving in a curvilinear orbit and therefore the emission from the tail of the bunch affects the head of the bunch as shown by the diagram in Fig. 2.5. In the 1-d approximation, the longitudinal electric

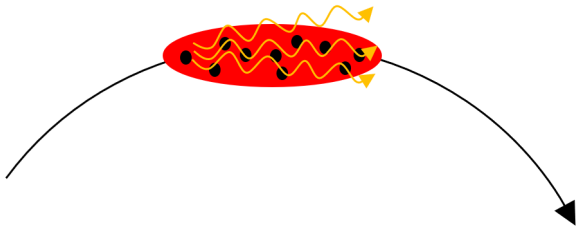

Figure 2.5: Diagram of a bunch in a curvilinear trajectory where radiation emitted from particles the back of the bunch reaches the particles in the head of the bunch.

field of the bunch is given by

$$E_l = \frac{1}{4\pi\epsilon_0}\frac{2eN}{3^{1/3}\rho^{2/3}}\int_z^\infty \frac{1}{(z'-z)^{1/3}}\frac{\partial\lambda(z')}{\partial z'}dz' \tag{2.11}$$

where N is the number of particles in the bunch. The energy loss of a single electron is proportional to N and therefore the total energy radiated by the bunch is proportional to N^2. Additionally, this effect is enhanced by high peak currents as found, for example, in the compressed bunches used to drive FELs.

In this chapter we have introduced basic ideas of beam dynamics. Twiss functions, emittances, brightness and luminosity and how these can be used to benchmark the performance of an accelerator. Then, we introduced the matrix formalism of beam dynamics with the magnetic field multipole expansion and chromatic amplitude. Together with the acceleration in rf cavities these concepts result in an overview of bunch compressors and how their longitudinal dynamics can be tuned. Finally, some effects that also play a role in longitudinal beam dynamics are introduced, including a description of the circumstances where they are most relevant: velocity bunching, LSC and CSR. All these concepts are used in the following chapters to develop a novel variable bunch compressor and a systematic technique for optimising accelerator designs where the longitudinal match, or the sequence of longitudinal phase space manipulation is important.

Chapter 3

Variable bunch compressors in MAX-IV

3.1 Introduction

The work presented in this chapter follows the published journal article [42] as part of this PhD. The author of this thesis carried out the analysis work presented in this chapter except where explicitly identified.

As introduced in chapter 2, magnetic bunch compressors are an increasingly common subsystem within linear electron accelerators for high brightness applications. They are used to manipulate the longitudinal phase space of a bunch for which there is a correlation between momentum deviation and longitudinal position caused by a preceding off-crest radio-frequency (rf) acceleration. For example, they are used to reduce the bunch length, and hence increase the peak current, in electron bunches intended to drive a free-electron laser (FEL). Bunch compressors are necessarily momentum dispersive, as the trajectory deviation with momentum is how longitudinal position changes within the bunch are made. Because of this need to transport and control bunches with large momentum spreads, the chromatic properties of bunch compressors are of paramount importance.

Using the standard matrix notation for beam transfer [43] introduced in Eq.2.4, the longitudinal position at the end of the bunch compressor as a function of momentum deviation can therefore be expressed as

$$z(s) = z(0) + R_{56}\delta + T_{566}\delta^2 + U_{5666}\delta^3 + \mathcal{O}(\delta^4) \tag{3.1}$$

where $z(0)$ is the initial longitudinal position of the particles in the bunch, $z(s)$ is the longitudinal position of the particles in the bunch at a position s along the reference trajectory, and R_{56}, T_{566} and U_{5666} are the first-, second- and third-order longitudinal dispersions and particles at the head of the bunch have $z > 0$. In this description, a chicane-like system has a positive R_{56} and an arc-like system negative R_{56} (for codes that utilise t instead of z as the longitudinal coordinate the opposite is true, hence our preference for the "like" descriptions as they are unambiguous). A consideration of the second-order longitudinal dispersion immediately reveals a disadvantage of the more common chicane-like implementations [44, 45]; both arc- and chicane-like systems have naturally negative T_{566}. To see this one may compare the path length as a function of energy deviation for both systems, shown in Fig. 3.1. At nominal energy, one sees that the linear slopes are of opposite sign, but the curvature is of the same sign. In an arc-like system, this property is welcome as the natural rf curvature (which places both head and tail at more positive z than a linear, falling rf chirp), is partially cancelled by the effect of T_{566}. Whereas in a chicane-like system, the T_{566} exacerbates the curvature of the rising rf chirp, necessitating deliberate cancellation by an additional external system. Typically this takes the form of a higher-harmonic rf linearizing cavity, which requires an expensive, additional rf system as well as facility space. Linearization can also be achieved with strong linac wakefields, as in the FERMI facility [46] where the final linac sections are backward-travelling wave structures. This lessens the correction required from a higher harmonic system, but does not eliminate it as tuning of the linearization is required. The arc-like systems presented here include such tune-ability. We illustrate the contrasting situations in Fig. 3.2. This context is particularly relevant for the MAX IV facility [47]. In addition to the longitudinal properties, when transporting and manipulating large energy

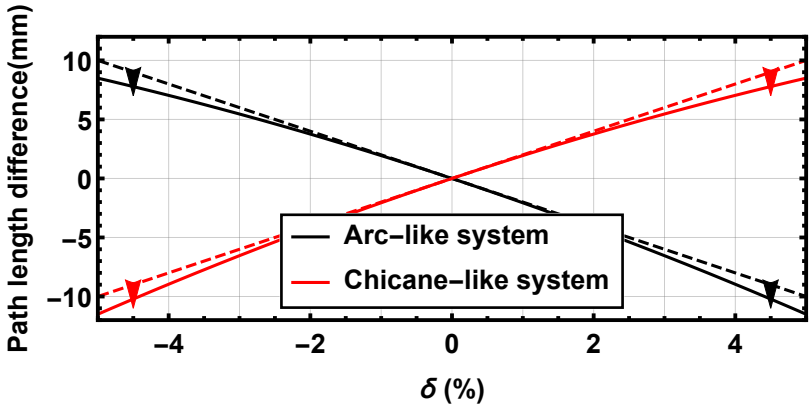

Figure 3.1: Path length difference with respect to the design trajectory as a function of momentum deviation for uncorrected arc-like (black) and chicane-like (red) compressors showing their respective deviations from linearity (dashed). $R_{56} = -0.2\,\text{m}$ $T_{566} = -0.6\,\text{m}$ in the arc-like system and $R_{56} = +0.2\,\text{m}$ $T_{566} = -0.6\,\text{m}$ in the chicane-like system.

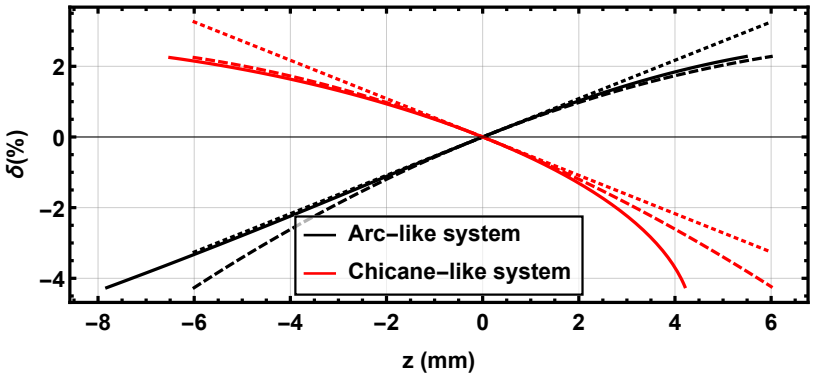

Figure 3.2: Longitudinal phase space of chirped bunches for compression in an arc-like system (black) and chicane-like (red). Ideal "linear" bunch (dotted), with curvature from the fundamental rf (dashed) and effect of negative T_{566} (solid) shown. We see that the curvature is exacerbated in the chicane-like system, and alleviated in the arc-like system.

spread bunches one must be mindful of the transverse chromatic properties. In order to analyse this in the various systems we study the **chromatic amplitude** function [40, 48] as introduced in the previous chapter in eqn. 2.6, which quantifies the linear chromatic error of our beam as a distribution and thus the energy dependence of the focusing. Lack of control over the chromatic derivatives of the Twiss parameters $\partial\alpha/\partial\delta$ and $\partial\beta/\partial\delta$ returns an increased projected and sliced emittance as a consequence of the disparities in dispersion and focusing strengths for different beam slices. It is worth noting that we do not use the single-particle variable **chromaticity**, this is more useful in storage rings where fractional energy deviations of order 10^{-5} are typical. In linacs operated off-crest, we expect energy spreads at the percent level in the low energy sections of the machine, therefore a measure based on energy variation within the particle bunch is far preferable.

The additional degree of freedom in the longitudinal phase space allows either manipulation of the bunch length at a fixed rf phase or manipulation of the rf phase (and therefore energy spread) at constant bunch length. These two cases and their implications on linearization are shown in Fig. 3.3 where the curvature has been cancelled in the compressed bunches and only third- and higher-order terms remain. At a constant rf phase, the T_{566} required for linearization remains the same. If we instead alter the rf phase keeping a constant bunch length the linearizing T_{566} varies as [49]

$$T_{566} = \frac{E_0^2}{2kV_{\mathrm{rf}}^2 \tan^3\theta}\,. \tag{3.2}$$

Motivated by this, we set out in this work two options to "retrofit" variability of R_{56} into the existing layout of MAX IV. We term these the **additional quadrupole** and **additional dipole** solutions, respectively. In doing so we establish the additional dipole solution as having the advantages of apochromaticity and order-by-order control of the momentum compaction, the disadvantage being that part of the trajectory must have a variable horizontal position.

Although the motivation is to introduce flexibility into the MAX IV facility, our observations on these arc-like compressors are generic and have wide potential future applicability

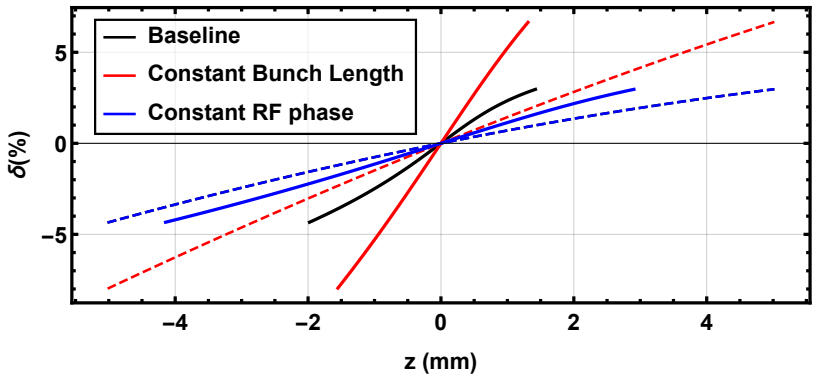

Figure 3.3: Longitudinal phase space of chirped bunches before (dashed) and after (solid) compression. The baseline bunch (black) is accelerated 20° on the falling side of the crest (overlapped by dashed blue line) is compressed with $R_{56} = -0.1\,\text{m}$ and linearized with $T_{566} = -0.70\,\text{m}$. After reducing R_{56} to $-0.05\,\text{m}$, a bunch of equal initial length (red) requires acceleration $\sim 40°$ off-crest with $T_{566} = -0.08\,\text{m}$. If the rf phase is kept constant (blue), the final bunch length increases and the T_{566} required for linearization remains unchanged.

in situations where large energy spread beams must be longitudinally manipulated. In particular, any laser (LWFA) or plasma (PWFA) wakefield generated beam would benefit from the deployment of the following proposed schemes for transport and conditioning. Additionally, the schemes hereby proposed are particularly suited to adoption in the rapidly developing field of electron diffraction facilities [50, 51].

3.2 Existing Fixed R_{56} Arc-Like Compressors

The two bunch compressors at MAX IV each consist of two back-to-back double-bend achromats with three phase advance matching quadrupoles separating them. The centre of each arc hosts a pair of quadrupoles to enforce the first-order achromatic condition and one sextupole for varying the second-order longitudinal momentum compaction away from the naturally over-linearizing value that is apparent in Fig. 3.2. The first compressor (BC1) is shown in Fig. 3.4. It is located $\sim 18\,\text{m}$ from the cathode at beam energy $\sim 275\,\text{MeV}$. The second compressor (BC2) is of an optically-similar design and is situated $\sim 298\,\text{m}$ from the cathode at beam energy $\sim 3000\,\text{MeV}$. In both systems, the beamline central trajectory is offset transversely by $\sim 2\,\text{m}$. For the rest of this chapter, we work with the

first bunch compressor. The design optics and dispersion function for BC1 are shown in Fig. 3.5.

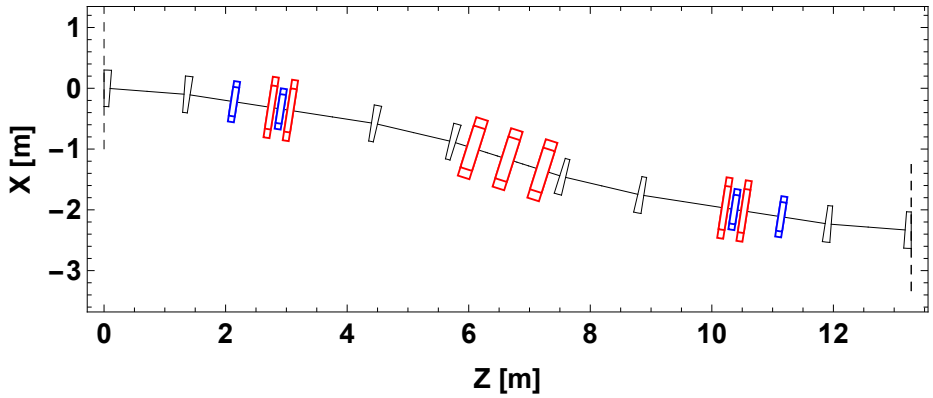

Figure 3.4: Existing MAX IV Bunch Compressor 1. Dipoles in black, quadrupoles in red and sextupoles in blue.

In the initial design shown, the sextupoles are set such that the T_{566} is reduced from nominal. The resulting R_{56} and T_{566} of this lattice are -32 mm and -91 mm respectively. A recent paper described a method of inserting sextupoles to ensure achromaticity of this design to third order [52]. We will comment on the ease of replicating this feature in the variable R_{56} proposals that follow.

3.3 Additional Quadrupole Variable R_{56} Compressor

The most conceptually-simple alteration one can make to the original compressors that enables manipulation of the R_{56} is the insertion of additional quadrupoles between each pair of dipoles as shown in Fig. 3.6. Varying the strength of these quadrupoles changes the value of the dispersion as it reaches the following dipole, thereby changing the R_{56} of each achromat following eqn. 2.8. The quadrupoles at the centre of each achromat are tuned to symmetrize the dispersion at each side. Following this scheme, we can reduce the final R_{56} magnitude continuously and even drive it to positive values. An example tuning is shown in Fig. 3.7 where we choose the isochronous condition. It should be noted that the quadrupole k-value for this tuning is rather large, at $\sim 33\,\mathrm{m}^{-2}$. Such a high

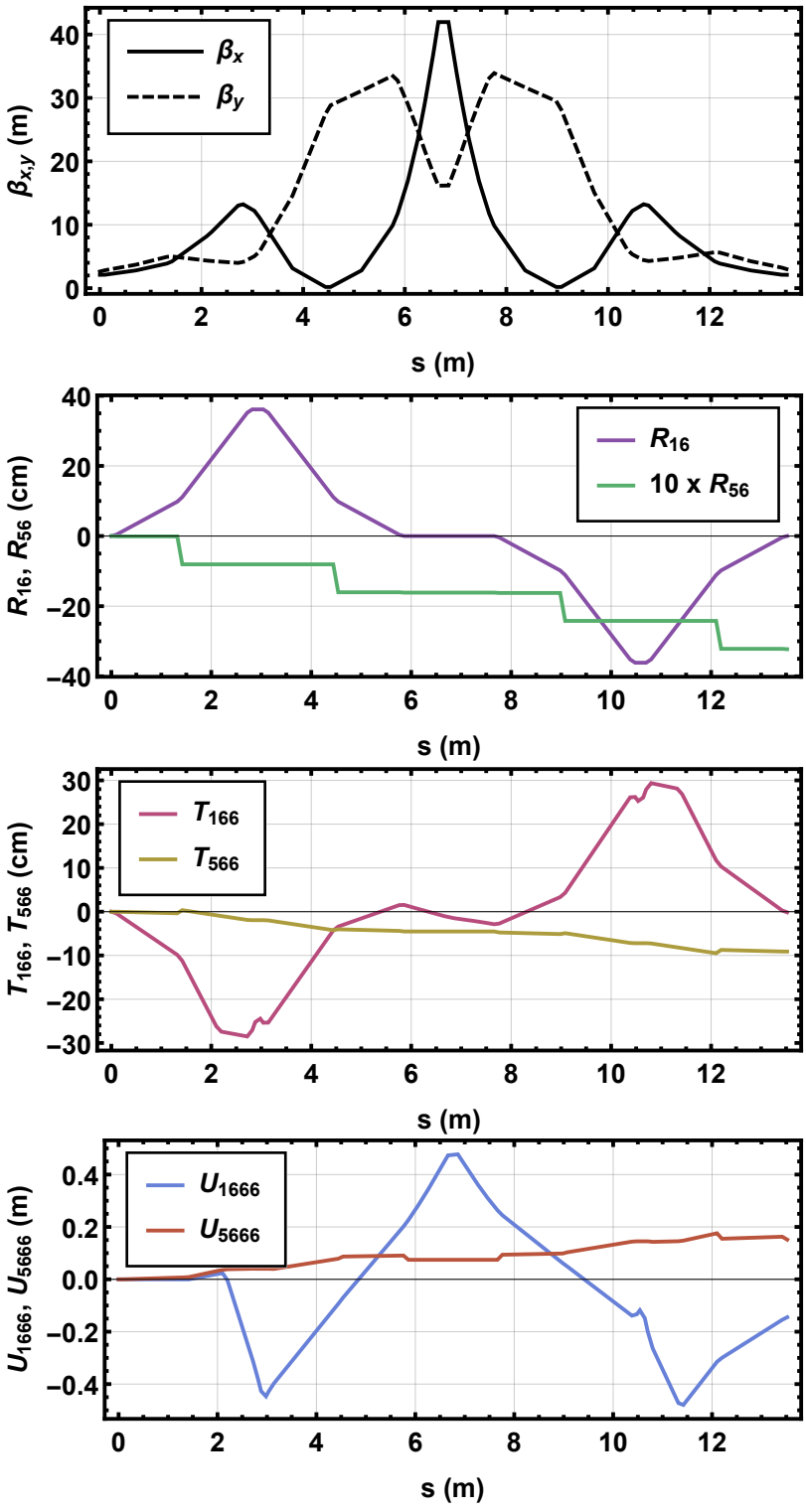

Figure 3.5: Optics and first-, second- and third-order horizontal and longitudinal dispersion functions of existing MAX IV BC1.

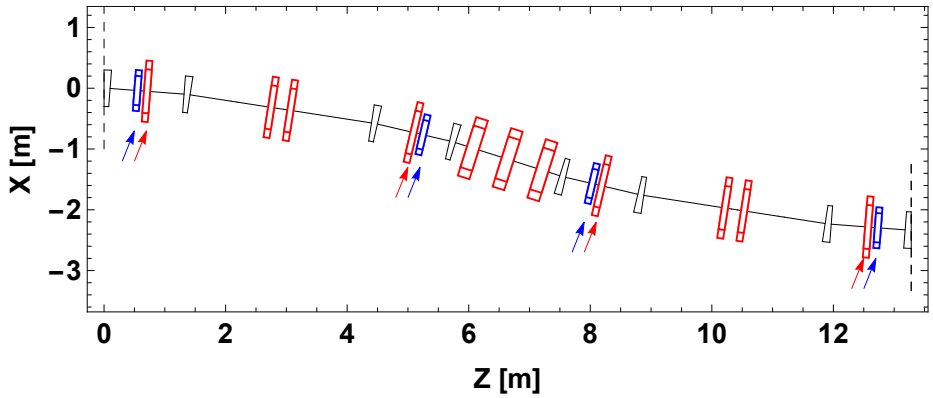

Figure 3.6: Additional quadrupoles layout. Dipoles in black, quadrupoles in red and sextupoles in blue. New elements highlighted by arrows.

k-value would require stronger magnets than the rest of the beamline and strong focusing can introduce chromatic errors.

In order to minimise second-order horizontal dispersion, T_{166}, we also insert additional sextupoles at the location where dispersion is highest for all the range of R_{56} configurations, following [52]. This is naturally reduced in comparison to the initial design as the second-order longitudinal dispersion across the whole bunch compressor is related to the transverse dispersion via eqn. 2.9.

Reasonable momentum acceptance for $\delta \leq 3\%$ is maintained, as shown in Fig. 3.8. However since all quadrupoles used for the dispersion manipulation are focusing, the chromatic performance is harmed. The chromatic behaviour in the vertical axis is also spoiled by the strong focusing as shown by the phase advance response to deviations in momentum (Figs. 3.9 and 3.10).

3.4 Additional Dipole Variable R_{56} Compressor

A standard solution adopted by many electron accelerators driving FELs is the *variable* four-dipole chicane bunch compressor [53]. The technique adopted is a mechanical change in the centroid trajectory, achieved through moving dipoles and beam tubes mounted on

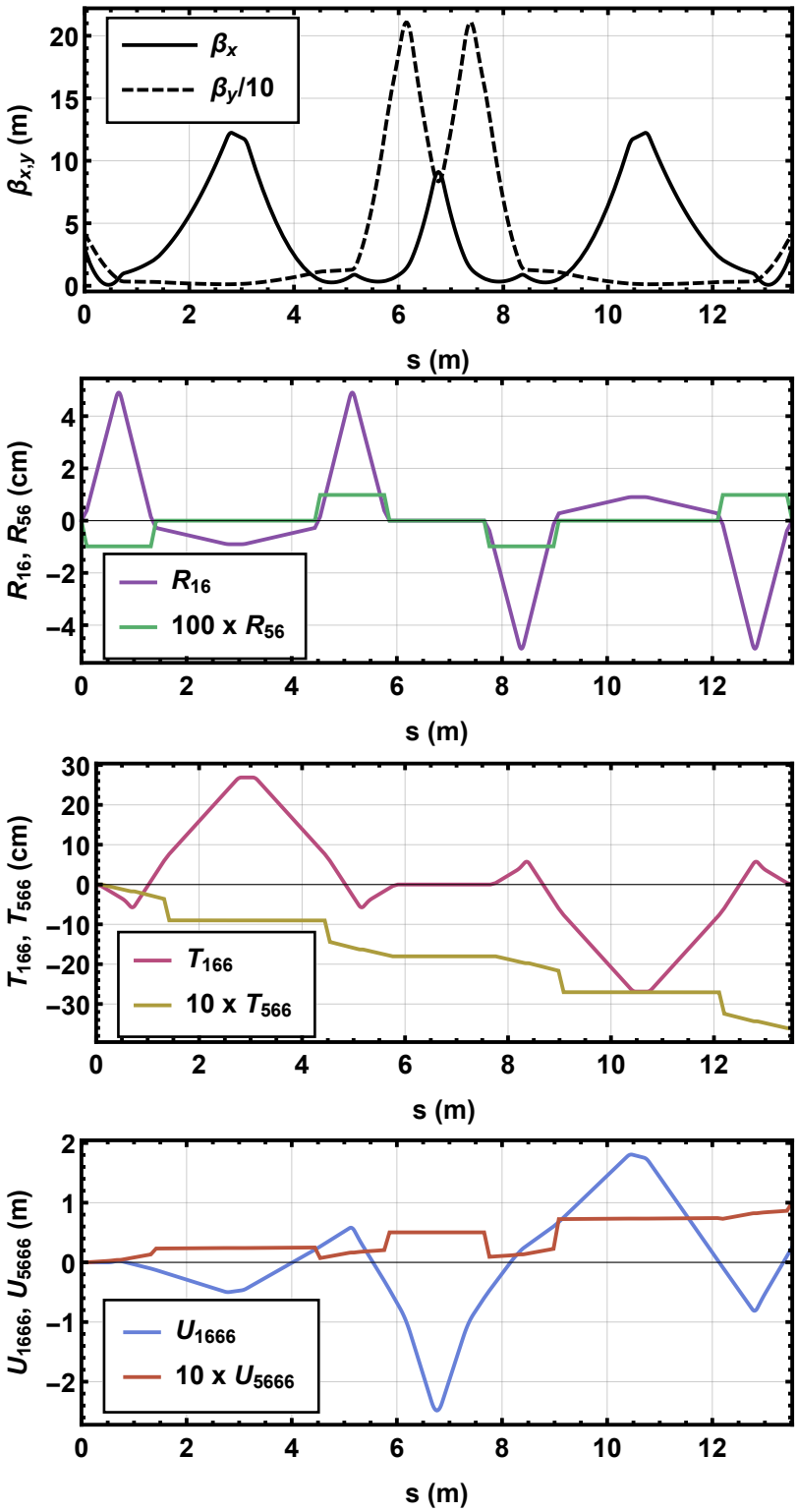

Figure 3.7: Optics, first-, second- and third-order longitudinal dispersion functions of additional quadrupole solution tuned to isochronous condition.

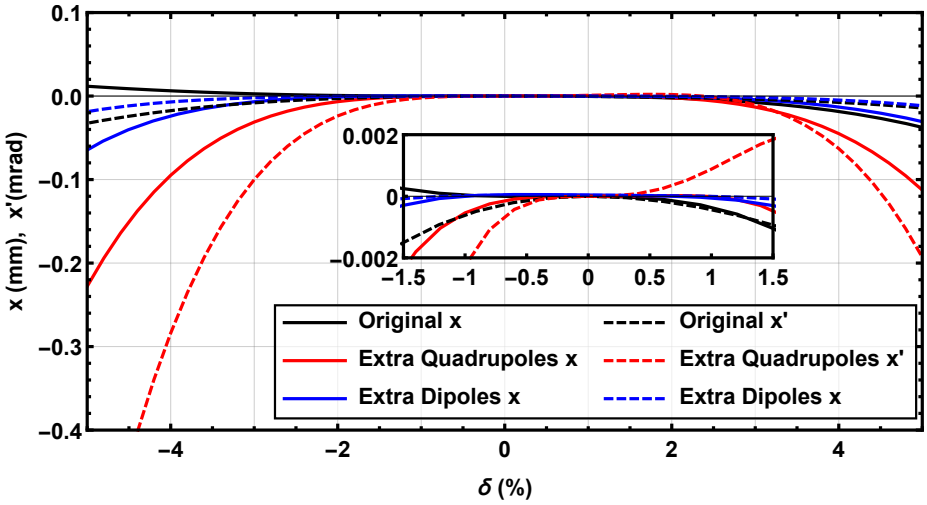

Figure 3.8: Horizontal momentum acceptance of the original, fixed design with chromatic corrections (black), variable with extra quadrupoles (red) and variable with extra dipoles (blue) solutions.

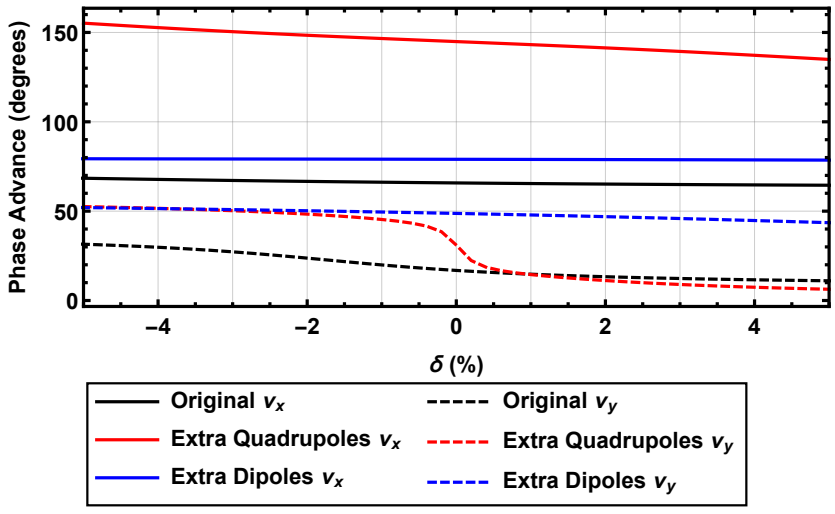

Figure 3.9: Phase advance dependence on δ at the end of BC1 for the Original lattice (black), extra quadrupoles (red) and extra dipoles solutions (blue).

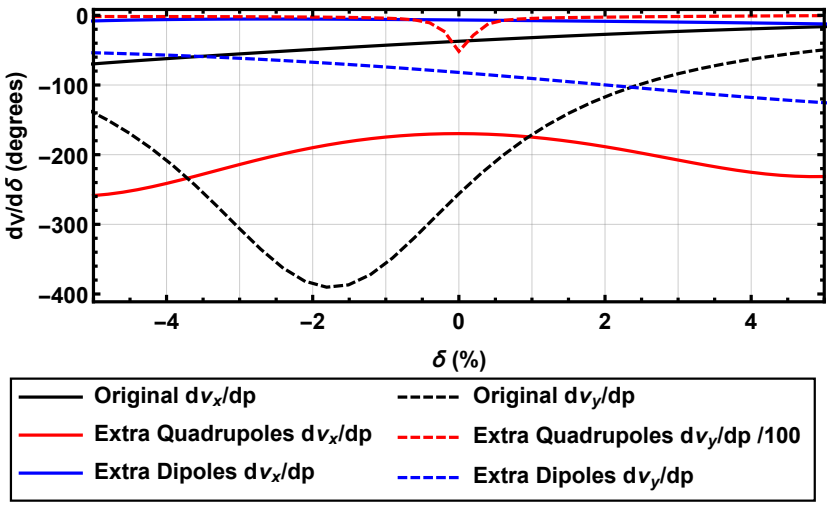

Figure 3.10: Derivative of the phase advance with respect to δ at the end of BC1 for the original lattice (black), extra quadrupoles (red) and extra dipoles solution (blue).

an actuated table. Here we adapt that approach in the context of arc-like compressors, analogously relaxing the concept of a fixed trajectory in order to gain an advantage in terms of chromatic behaviour over the strongly-focusing additional quadrupole solution.

Our technique draws inspiration from the recent deployment of "anti-bend" cells (cells with bending of opposite sign to the rest), in low emittance storage ring lattice designs [54, 55], where the purpose is also the control of dispersion.

We insert an additional dipole in between each pair of existing ones. The resulting layout for MAX IV BC1 is shown in Fig. 3.11. As we are working within a fixed footprint, the total bending angle of each three-dipole subsystem must remain constant. Thus the bend angle of our additional dipole is set by alterations of the strength of the existing two dipoles as shown in Fig. 3.12.

Unlike a four-dipole compressor, the excursion of the trajectory as the R_{56} is varied is small enough that no actuation is needed, merely an expanded beam tube. However, as the trajectory explores a large range of offsets within the new dipole, care must be given in considering the properties of the good field region. Additionally, different trajectories also have different path lengths. The original dipoles are of combined function in order to provide additional vertical focusing, ensuring the two planes are not very different

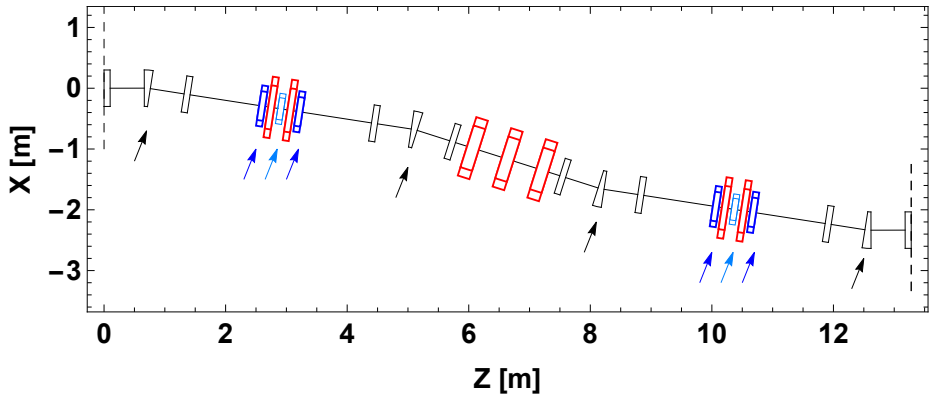

Figure 3.11: Additional Dipoles layout. Dipoles in black, quadrupoles in red, sextupoles in blue and octupoles in light blue. New elements highlighted by arrows.

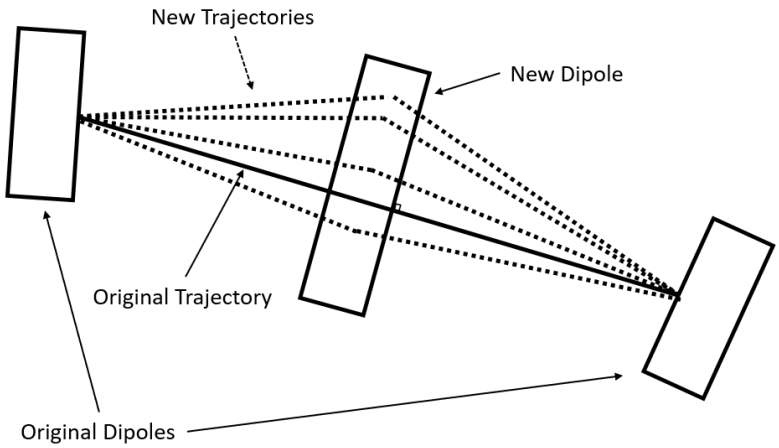

Figure 3.12: Schematic of new dipole with the original trajectory (solid) and different new trajectories (dashed) for different R_{56} values. For very low values of R_{56} the original dipoles become reverse bends.

in terms of phase advance over the system. They share $\phi : k_1 : k_2$ ratios with the initial parameters $\pm 76\,\mathrm{mrad} : -3.0\,\mathrm{m}^{-2} : 3.1\,\mathrm{m}^{-3}$. Since different R_{56} configurations have different trajectories across these new dipoles, designing a magnet with specific quadrupole and sextupole components for each trajectory is challenging. Therefore it was decided to use flat dipoles (no quadrupole or sextupole moments), leaving open the option to implement them with the correct sign further along the design process if it became necessary to relax the optics or sextupole strengths. Additionally, we considered the magnet edge angles, as these have focusing effects in both vertical and horizontal planes. The existing dipoles are rectangular magnets, such that $e_1 + e_2 = \phi$ where e_1 and

e_2 are the entry and exit edge angles and ϕ is the total bending angle. Here we consider 3 different configurations. Firstly, rotate the dipoles for each desired R_{56} configuration, such that entry and exit angles are always equal. Secondly, a simpler option in terms of implementation is to set $e_1 = 0$ and $e_2 = \phi$. Finally, we consider a new design of a magnet with curved edges such that $e_1 = e_2 = 0$ for all ϕ. We want to minimise horizontal focusing as it would counteract our dispersion generation. Both stationary and rotating dipoles configurations give a net-zero horizontal focusing, while the sector magnet provides a positive horizontal focus. Therefore we select the stationary dipole configuration as the difference in vertical focus is minimal ($\propto \phi^3$), and it is mechanically simpler to implement since maintaining the balance of the edge angles would require rotating dipoles. The new magnets are also rectangular and as they are situated in a symmetric point between the original dipoles, their edge angles are $e_1 = e_2 = \phi/2$.

The limits of this strategy lie in the maximum dipole field we can achieve without requiring permanent or superconducting magnets and the design of the new dipoles that must accommodate a wide horizontal acceptance for the different R_{56} configurations. The requirements on the dipole strength can be lessened by using a longer dipole, provided there is space in the beamline. In the original, fixed design, $R_{56} = -32\,\mathrm{mm}$. For $R_{56} = -15\,\mathrm{mm}$ we need a horizontal acceptance of $3.1\,\mathrm{cm}$, for $R_{56} = 0\,\mathrm{mm}$, the acceptance grows to $4.4\,\mathrm{cm}$, and finally for $R_{56} = +5\,\mathrm{mm}$ the deviation of the centroid trajectory at the entry to the extra dipole with respect to the original design is $4.8\,\mathrm{cm}$.

As in the additional quadrupole solution, the quadrupoles in the centre of each achromat are tuned to symmetrize the dispersion at each side.

Sextupoles are used to cancel the elements T_{166} (as shown in Fig. 3.13) and T_{266} at the end of the bunch compressor, thereby improving its chromatic behaviour. With an additional family of sextupoles we can regain control of the T_{566} term, thus our system exhibits independently tune-able R_{56} and T_{566}. Finally, a single pair of octupoles is used to cancel the third-order horizontal dispersion, U_{1666}, using the anti-symmetry in the bending angles over the whole bunch compressor. A configuration with $R_{56} = 0\,\mathrm{cm}$ and T_{566} shifted from

the natural $\sim -9.6\,\text{cm}$ to $-4.0\,\text{cm}$ is shown in Fig. 3.13. The limits on the T_{566} variability depend on the starting T_{566} for the chosen R_{56}, sextupole and octupole strength. We show magnet parameters for the isochronous solution in Tab. 3.1.

Table 3.1: Magnet parameters for MAX IV BC1 with additional dipoles. We choose as an example the first-order isochronous, second-order linearized solution: $R_{56} = 0\,\text{cm}$ $T_{566} = -4.0\,\text{cm}$

	$k_1(\text{m}^{-2})$	$k_2(\text{m}^{-3})$	$k_3(\text{m}^{-4})$
Dipoles 1, 3, 4 & 6	0.0783	-0.08185	0
Dipoles 2 & 5	0	0	0
Dipoles 7, 9, 10, 12	0.0783	-0.08185	0
Dipoles 8 & 11	0	0	0
Quadrupoles 1, 2, 6 & 7	4.88141	0	0
Quadrupoles 3 & 5	-3.1747	0	0
Quadrupole 4	6.30158	0	0
Sextupole 1	0	215.345	0
Sextupole 2	0	-116.801	0
Sextupole 3	0	116.801	0
Sextupole 4	0	-215.345	0
Octupoles 1 & 2	0	0	-2373.73

In order to study the transverse chromatic properties of the bunches, we analyse the chromatic dependences of the Twiss parameters in Fig. 3.14, as these determine the behaviour of the chromatic amplitude function. The additional dipole solution shows a smaller chromatic dependence of the Twiss parameters and thus is expected to result in a smaller longitudinal projected emittance growth than the additional quadrupole solution.

3.5 Comparison between the proposed solutions

Both the additional quadrupole solution and the additional dipole solution provide a lattice with the desired R_{56} while also being able to recover the current properties of the lattice.

The additional quadrupole solution relies on the placement of quadrupoles within the dispersive sections to manipulate the dispersion. This in turn has an unavoidable impact on the optics which need to be kept in check by the quadrupoles in the middle section

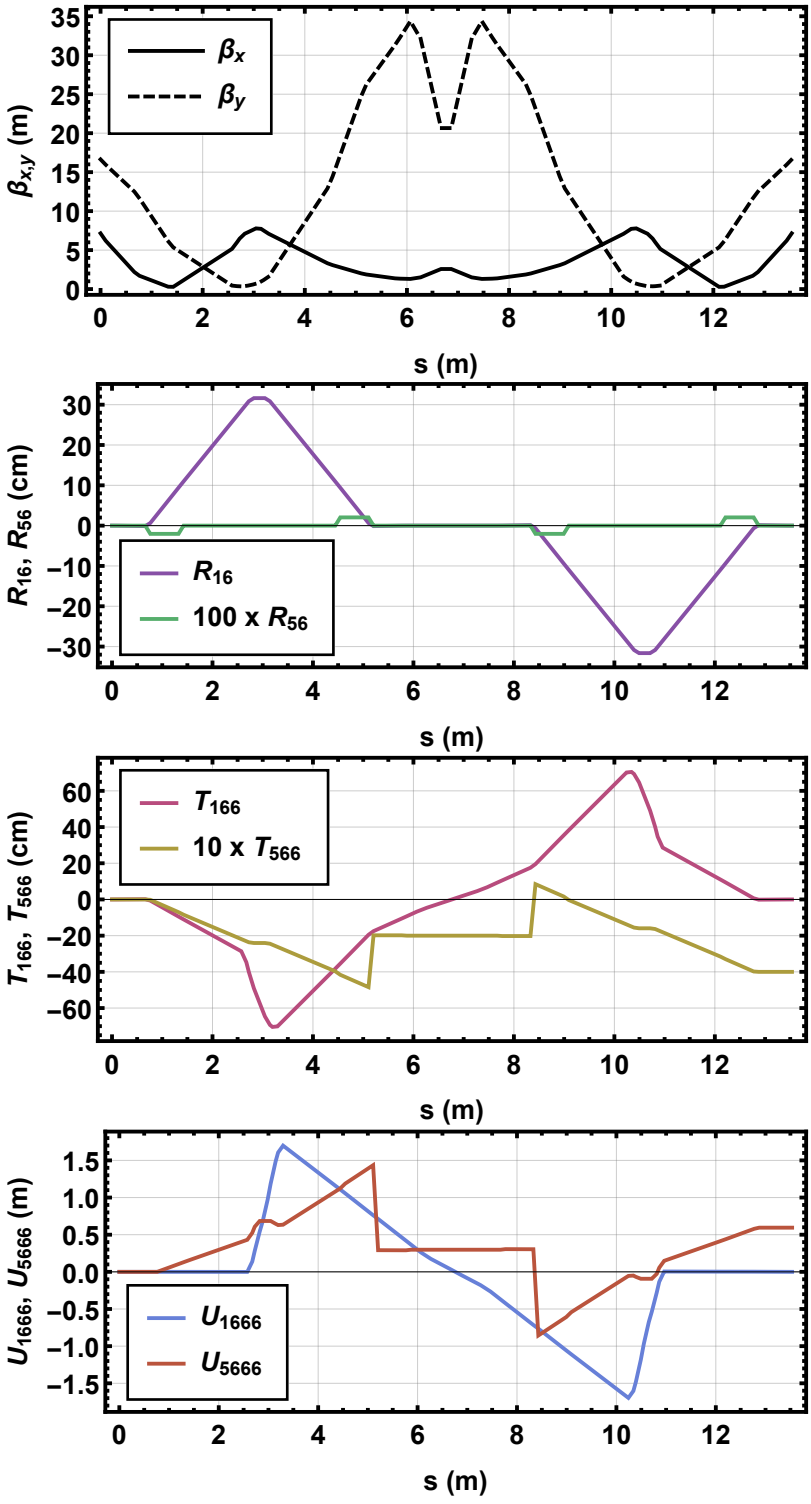

Figure 3.13: Optics and first-, second- and third-order dispersion functions of isochronous MAX IV BC1 with additional dipoles. $R_{56} = 0\,\text{cm}$ $T_{566} = -4.0\,\text{cm}$

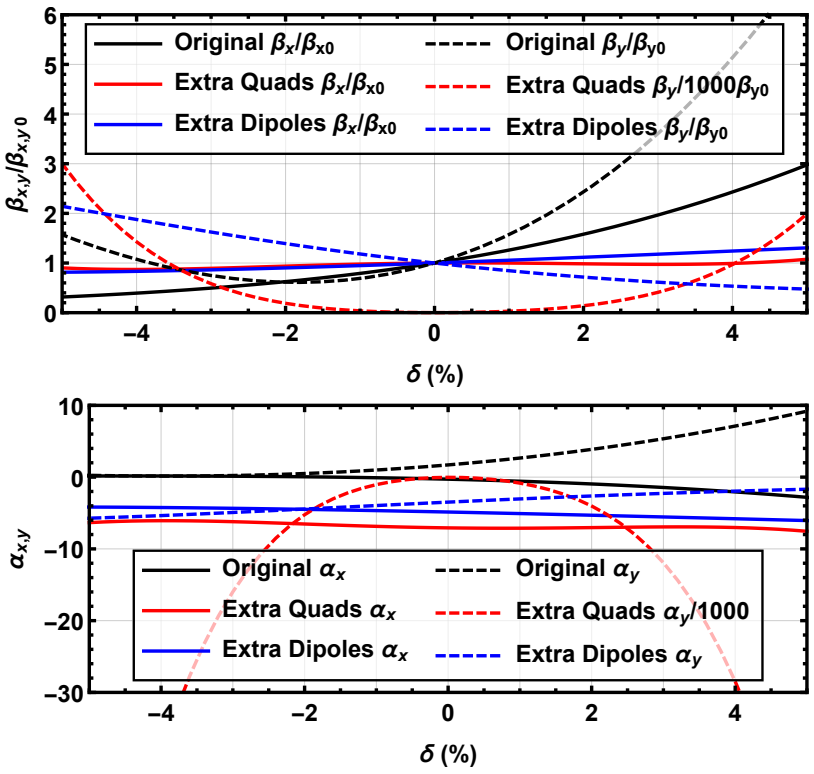

Figure 3.14: Chromatic dependence of the beta (top) and alpha (bottom) functions at the end of BC1 for the original, fixed lattice (black), additional quadrupole (red) and additional dipole (blue) solutions.

where the disperison is zero. This results in very strong focusing requirements which impact negatively the chromatic performance of this solution. The limiting factor on the range of longitudinal dispersions available is the maximum field deliverable by these quadrupoles. Moreover, the maximum value of the dispersion is reduced compared to the initial lattice and therefore the strength of the sextupoles correcting the second order dispersion must increase accordingly.

The additional dipole solution relies on changing the sequence of bending angles that the beam goes through to achieve the desired longitudinal dispersion. In contrast to the additional quadrupole solution, the only additional focusing that this solution provides is the edge focusing of the dipoles. This weaker focusing will be shown to be the determinating factor favouring the additional dipole solution in section 3.6. Without the extra focusing, the sextupoles and octupoles can be placed around the dispersion peaks to maximize their efficacy. Finally, the limiting factor on the range of longitudinal dispersions available for this solution is a combination of the maximum field available at the additional dipole.

3.6 Particle Tracking Studies

In order to further investigate the performance of both candidate lattices, we track a bunch from the linac up to the exit of the bunch compressor. This tracking study was carried out in collaboration with Bill Kyle at MAX IV Laboratory using realistic bunches. We include collective effects, in particular coherent synchrotron radiation (CSR) in this tracking. The effect is however negligible due to the relatively long bunch length. In the additional quadrupoles solution, as predicted by Fig. 3.14, emittance growth of orders of magnitude is present. The greatest emittance growth is located in the section before BC1 and especially in the central triplet of the bunch compressor (Fig. 3.15b). Both of these are related to the optical constraints of the system. In order to drive the dispersion and achieve the R_{56} ranges that we are aiming for, all the focusing needed from the quadrupoles results in a strongly focused system. This causes transverse phase space distortion of the large

relative energy spread beam, resulting in the emittance growth seen. In addition to this, the beam would be further degraded in the downstream matching section. By contrast, the additional dipole solution, without the optical constraints, is shown to better preserve the beam quality across the bunch compressor as show in Fig. 3.15a.

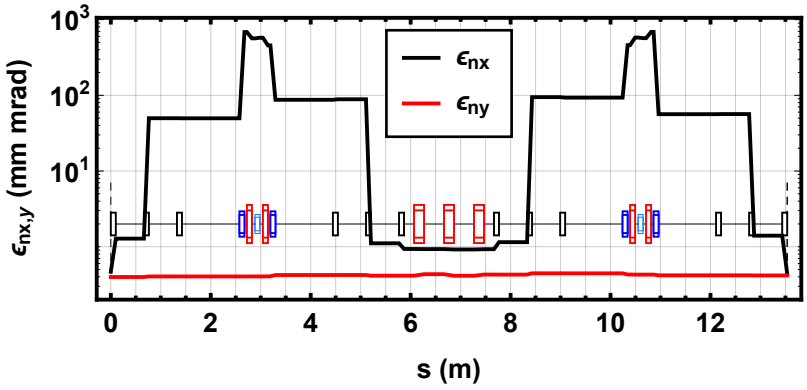

(a) Beam emittance evolution in additional dipole solution.

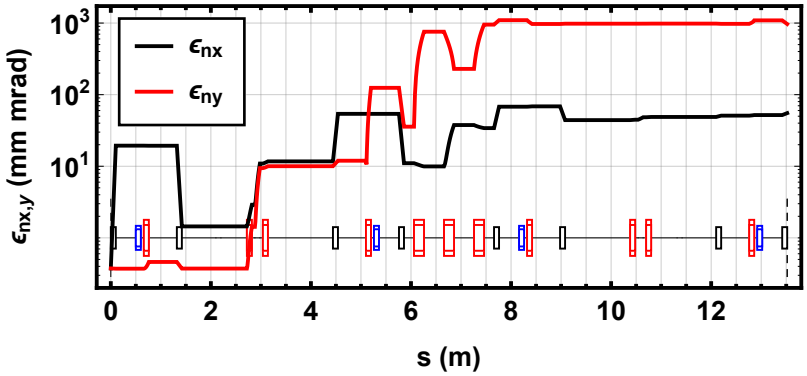

(b) Beam emittance evolution in additional quadrupole solution.

Figure 3.15: Beam emittance evolution in additional dipole and additional quadrupole configurations.

3.7 Conclusion

We have presented two solutions to retrofit variable order-by-order momentum compaction into the MAX IV arc-like bunch compressors. In both cases, we are able to move from the natural R_{56} through the isochronous condition to the opposite sign (thereby mimicking a chicane-like compressor). In the additional quadrupole case, the strong focusing needed

for the dispersion manipulations greatly worsen the beam quality with emittance growths of orders of magnitude. In the additional dipole case, we can do this without chromatic penalty and showing minimal emittance growth using sextupole and octupole magnets. This solution is presently under detailed engineering consideration for adoption in the MAX IV Soft X-ray FEL upgrade project.

Finally, this is a concrete example of a design driven by longitudinal dynamics requirements. This type of design will become necessary to achieve optimal longitudinal matches in Energy Recovery Linacs as shown in the following chapters.

Chapter 4

Longitudinal matches in ERLs

4.1 Introduction

The work presented in this chapter follows the published journal article [56] as part of this PhD.

Depending on the application, the desired characteristics of a bunch's longitudinal phase space at an interaction point can be broadly categorised into two distinct classes. If the bunch peak current is to be significantly increased upon acceleration to drive, for example, a high power FEL [32, 57] we term it a **compressive match**. If instead energy spread minimization is required, for example in a collider, we term it an **energy spread minimising match**. Of course, some situations require a partial compression, in this work we choose to explore the extremes of this continuum in order to highlight their contrasting characteristics.

ERLs can be further classified into those in which energy loss due to synchrotron radiation is an appreciable percentage of the beam energy and those in which synchrotron radiation losses can be neglected. As this scales as the Lorentz factor to the fourth power [58], realistically-sized facilities can be split into those below a few GeV, and those above.

Finally, many different arrangements of the accelerator elements can form an ERL, however one critical characteristic of all possible topologies is whether the beam traverses the same arc[1] accelerating and decelerating, or if the beam only traverses each arc once. The former case we term **common transport**, the latter we term **separate transport**. An example of each of these is shown in Fig. 4.1. The additional degrees of freedom available in a separate transport ERL are control of path lengths and longitudinal dispersions independently during acceleration and deceleration.

In this chapter we explore these categories of possible ERLs and how each category exhibits a different set of possible longitudinal matches.

4.2 Definitions & Assumptions

In setting out our general framework for constructing longitudinal matches for energy recovering systems we make the following approximations:

- The quality factor,Q, of an rf system is effectively infinite. Equivalently the time taken for a bunch to transit the entire system is small compared to $Q \times T$ where T is an rf period.
- The bunch charge is such that the system is below any beam break-up (BBU) threshold where the higher order modes of a superconducting cavity are excited coherently in a recirculating linac or ERL.
- The system is in steady-state, any start-up transients have dissipated.

As such this methodology establishes the single bunch longitudinal dynamics in steady-state. The consequences of relaxing the first two conditions are explored in [59, 60], where we see that the ordering of bunches, or **filling pattern**, affects low-level rf (LLRF) stability and the regenerative BBU threshold.

[1] In practice, what we refer to here as "arc" will actually comprise a spreader-arc-recombiner sequence of transport elements between linac passes or interaction regions

Each pass of the beam through an rf section represents a load. We represent this load in the complex plane as shown later in Fig. 4.4. A beam on the accelerating crest is defined as $\theta = 0$, with the decelerating trough being $\theta = \pi$ following eqn. 2.7. We can use this to illustrate the full system characteristics of a longitudinal match and determine its viability. As a first approximation, a complete energy recovery match exhibits a resultant load (vector sum of each pass) lying on the vertical axis. This corresponds to the energy transferred from the rf system to the beam during acceleration being equal to the energy deposited back from the beam to the rf cavities during deceleration. A resultant that lies exactly at the origin indicates that any off-crest acceleration is matched by corresponding off-trough deceleration[2]. If the ERL consists of multiple rf sections, the resultant rf load of each section must lie on the vertical axis unless there is a mechanism present to transfer load between them, for example [61, 62]. If energy lost to synchrotron radiation (SR) is significant, this energy balance must change. We may either reduce the energy recovery efficiency by the same amount as is lost to SR, or keep full ER but offset the dump and injector energies by the same amount. We explore the consequences of each of these choices.

The rf phase that the beam sees on each pass is determined by the arc path lengths and the synchronicity between the different linac sections. In a separate transport ERL, we can independently tune phases in all accelerating and decelerating passes, whereas in a common transport ERL our initial conditions and accelerating phases determine the corresponding decelerating phases.

The injection energy is chosen to be as low as possible (typically a few MeV), limited by the ability to cope with the phase slippage associated with non-relativistic time of flight [8, 63]. The different phase choices affect the mean energy of the particles in the bunch and chirp. Depending on the system application, the fully accelerated beam may require a chirp or not. Similarly, during deceleration, as the beam's relative energy spread undergoes adiabatic growth, proper setting of phases and longitudinal dispersions are required to keep

[2]Naively one could expect that this condition guarantees that any chirp imparted to the bunch on acceleration is removed on deceleration. However, this is not generally the case, we explore this point later.

the beam within the energy acceptances of the arcs.

Many different configurations are possible for a common transport ERL, in this work we focus on a racetrack configuration similar to ER@CEBAF [13, 64] and PERLE [16], dealing with these two concrete cases in chapters 5 and 6 respectively. This employs two linacs to provide higher density of accelerating sections for the same footprint as compared to a single linac such as S-DALINAC [8]. For ease of comparison, we consider separate transport examples with topologies which match our common transport design during acceleration. However, instead of re-injecting the top energy beam into the injection linac it is re-injected into the opposing linac. In this way, accelerating and decelerating beams of the same energy traverse different arcs. Schematics of these topologies are shown in Fig. 4.1.

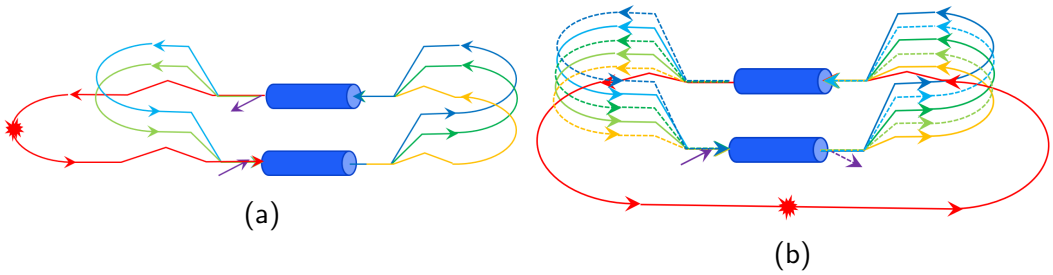

Figure 4.1: Simplest racetrack ERL configurations, blue cylinders represent the linacs, and the spiked ball represents the interaction region. (a) common transport and (b) separate transport, with solid and dashed lines indicating the arcs traversed during acceleration and deceleration respectively.

When considering viable longitudinal matches, we favour isochronous arcs over non-isochronous ones. This is to minimize beam degradation due to collective effects that become magnified by R_{56} excursions and the resulting longitudinal bunch charge distribution modulations [65].

Additionally, we must consider the implications of parasitic compressions, also know as overcompressions, where the bunch head and tail exchange places. One could expect significant degradation to occur at a parasitic compression, and it would be of particular concern during acceleration. However if the minimum bunch length during this compression is relatively large due to the presence of uncompensated rf curvature at that location,

such degradation would not be significant.

Harmonic rf is an established technique to linearize longitudinal phase space [66]. It may also be used to top up the energy of both accelerating and decelerating beams in an ERL, in order to compensate for energy lost to synchrotron radiation. However, linearization requires some deceleration of the bunch during acceleration, and some acceleration during deceleration reducing the maximum acceleration achievable, as can be seen from considering the Fourier series expansion of a "square" function [49] and shown in Fig.4.2. Whereas, a compensation for SR requires always accelerating the bunch. Therefore one cannot simultaneously compensate for SR loss **and** linearize. Finally, the cost implications of an additional SRF system motivates the study of alternatives to correctly manipulate the longitudinal phase space. For these reasons, we do not consider them in this work.

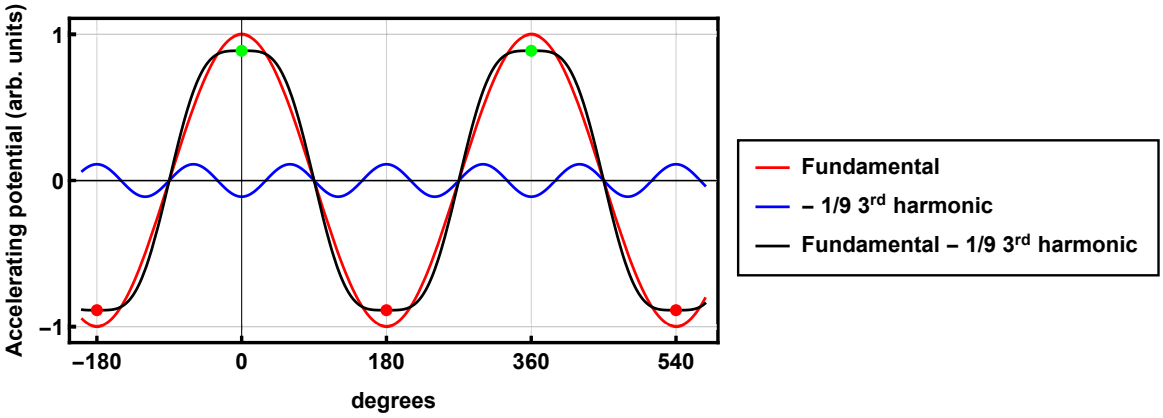

Figure 4.2: Fundamental mode (red), scaled 3rd harmonic (blue) and their sum (black). The combination of both modes shows a linearized potential around crest (green dots) and trough (red dots) but with lower amplitude than the fundamental.

4.3 Semi-analytic method

We employ a semi-analytic method extended from that of Zagorodnov and Dohlus [66], adding ERL operational constraints to find self-consistent longitudinal matches, where such a match results in the desired longitudinal phase space transformations in the beam. An alternative strategy would be to use one-dimensional longitudinal phase space particle

tracking [67]. We consider this to be impractical and opaque due to the large number of discrete stages required in a multipass ERL design, which results in a solution space of a very large dimension. In principle, one could employ genetic algorithms or similar methods to search this space, but in doing this one loses full understanding of minimal, simplest solutions. A semi-analytic method lends itself more readily to conceptual simplicity.

The energy distribution of the initial bunch is approximated as

$$\delta_0(z) = \delta_0' z + \frac{\delta_0''}{2} z^2 + \frac{\delta_0'''}{6} z^3 \,, \tag{4.1}$$

where z is the longitudinal position of the particles in the bunch, δ is the fractional energy deviation with respect to the nominal energy and the 0 subscript indicates this is the initial bunch. Throughout this work, the coordinate z (initial position in the bunch) is used as an independent coordinate and all other functions depend on it. For example, the function $z_i(z)$ refers to the position a particle with initial position z has after the i^{th} stage. For simplicity we omit the dependence on the initial coordinate z in the notation.

Arc elements are defined as drifts such that

$$z_i = z_{i-1} + (R_{56}^{(i)}\delta_i + T_{566}^{(i)}\delta_i^2 + U_{5666}^{(i)}\delta_i^3) \quad i \geq 1 \,, \tag{4.2}$$

where i represents the element index. From this point we'll use a simplified notation $r_{56i} \equiv R_{56}^{(i)}$, $t_{56i} \equiv T_{566}^{(i)}$ and $u_{56i} \equiv U_{5666}^{(i)}$, giving the transformations of the longitudinal coordinate as,

$$z_i = z_{i-1} + (r_{56i}\delta_i + t_{56i}\delta_i^2 + u_{56i}\delta_i^3 + \mathcal{O}(\delta_i^4)) \quad i \geq 1 \,, \tag{4.3}$$

with its first derivative

$$\frac{\partial z_i}{\partial z} = z_i' = z_{i-1}' + (r_{56i}\delta_i' + 2t_{56i}\delta_i\delta_i' + 3u_{56i}\delta_i^2\delta_i' + \mathcal{O}(\delta_i^4)) \quad i \geq 1 \,, \tag{4.4}$$

with its second derivative

$$\frac{\partial^2 z_i}{\partial z^2} = z_i'' = z_{i-1}'' + (r_{56i}\delta_i'' + 2t_{56i}\delta_i''\delta_i + 2t_{56i}\delta_i'^2 + 3u_{56i}\delta_i''\delta_i^2 + 6u_{56i}\delta_i'^2\delta_i + \mathcal{O}(\delta_i^4)) \quad i \geq 1 \tag{4.5}$$

and its third derivative

$$\begin{aligned}\frac{\partial^3 z_i}{\partial z^3} = z_i''' = z_{i-1}''' + (r_{56i}\delta_i''' + 6t_{56i}\delta_i''\delta_i' + 2t_{56i}\delta_i'''\delta_i + 6u_{56i}\delta_i'^3 + \\ 18u_{56i}\delta_i\delta_i'\delta_i'' + 3u_{56i}\delta_i^2\delta_i''' + \mathcal{O}(\delta_i^4)) \quad i \geq 1\,.\end{aligned} \tag{4.6}$$

rf elements are modeled as thin lenses where

$$\delta_i = \frac{(1+\delta_{i-1})E_{i-1} + \Delta E_i}{E_i} - 1 \quad i \geq 1\,, \tag{4.7}$$

and E_i is the beam centroid energy at the i^{th} stage and

$$\Delta E_i = eV_i \cos(kz_{i-1} + \theta_i) \quad i \geq 1\,, \tag{4.8}$$

where e is the electron charge, V_i is the peak accelerating voltage of the i^{th} stage, $k = 2\pi/\lambda_{\text{rf}}$, with λ_{rf} as the cavity wavelength and θ_i the cavity phase as seen by the reference particle at the i^{th} stage. Introducing

$$X_i = eV_i \cos(\theta_i) = \Delta E_i(z=0) \qquad \text{and} \qquad Y_i = eV_i \sin(\theta_i) \tag{4.9}$$

to simplify our notation, we can rewrite the energy difference at the i^{th} stage as

$$\begin{aligned}\Delta E_i &= eV_i \cos(kz_{i-1} + \theta_i) \\ &\approx X - kY z_{i-1} - \frac{1}{2}k^2 X z_{i-1}^2 + \frac{1}{6}k^3 Y z_{i-1}^3 + \mathcal{O}(z_{i-1}^4)\end{aligned} \tag{4.10}$$

and the energy deviation with its derivatives as

$$\begin{aligned}\delta_i &= \frac{(1+\delta_{i-1})E_{i-1} + \Delta E_i}{E_i} - 1 \\ &= \frac{E_{i-1} + \delta_{i-1}E_{i-1} + \Delta E_i}{E_i} - 1 \\ &\approx \frac{E_{i-1} + \delta_{i-1}E_{i-1} - E_i + X - kYz_{i-1} - \frac{1}{2}k^2Xz_{i-1}^2 + \frac{1}{6}k^3Yz_{i-1}^3 + \mathcal{O}(z_{i-1}^4)}{E_i}\end{aligned} \tag{4.11}$$

$$\delta_i' = \frac{\partial \delta_i}{\partial z} \approx \frac{1}{E_i}\left(\delta_{i-1}'E_{i-1} - kYz_{i-1}' - k^2Xz_{i-1}'z_{i-1} + \frac{1}{2}k^3Yz_{i-1}'z_{i-1}^2\right) \tag{4.12}$$

$$\begin{aligned}\delta_i'' = \frac{\partial \delta_i'}{\partial z} \approx \frac{1}{E_i}\Big(&\delta_{i-1}''E_{i-1} - kYz_{i-1}'' - k^2Xz_{i-1}''z_{i-1} - k^2Xz_{i-1}'^2 \\ &+ \frac{1}{2}k^3Yz_{i-1}''z_{i-1}^2 + \frac{1}{2}k^3Yz_{i-1}'^2z_{i-1}\Big)\end{aligned} \tag{4.13}$$

$$\begin{aligned}\delta_i''' = \frac{\partial \delta_i''}{\partial z} \approx \frac{1}{E_i}\Big(&\delta_{i-1}'''E_{i-1} - kYz_{i-1}''' - k^2Xz_{i-1}'''z_{i-1} - 3k^2Xz_{i-1}'z_{i-1}'' \\ &+ \frac{1}{2}k^3Yz_{i-1}'''z_{i-1}^2 + 3k^3Yz_{i-1}z_{i-1}'z_{i-1}'' + 2k^3Yz_{i-1}'^3\Big)\end{aligned} \tag{4.14}$$

where we have taken the Taylor expansion to third order.

If we work under the assumption that our reference particle is at the design energy, $\delta_i(0) = 0$ it follows from Eq.4.2 that $z_i(0) = 0$ and therefore the equations above (4.11, 4.12, 4.13 and 4.14) can be simplified to

$$\delta_i \approx \frac{E_{i-1} + \delta_{i-1}E_{i-1} - E_i + X}{E_i}\,, \tag{4.15}$$

$$\delta_i' \approx \frac{1}{E_i}\left(\delta_{i-1}'E_{i-1} - kYz_{i-1}'\right)\,, \tag{4.16}$$

$$\delta_i'' \approx \frac{1}{E_i}\left(\delta_{i-1}'' E_{i-1} - kY z_{i-1}'' - k^2 X z_{i-1}'^2\right) \tag{4.17}$$

and

$$\delta_i''' \approx \frac{1}{E_i}\left(\delta_{i-1}''' E_{i-1} - kY z_{i-1}''' - 3k^2 X z_{i-1}' z_{i-1}'' + 2k^3 Y z_{i-1}'^3\right) \tag{4.18}$$

respectively.

Finally, the effect of incoherent synchrotron radiation (ISR) is approximated by a single element such that

$$\Delta E_i = -U_0 = -\frac{C_\gamma E_0^4}{\rho_0} \tag{4.19}$$

where, as introduced in [58], U_0 is the energy radiated in one revolution, by an electron bunch with nominal energy E_0, following a trajetory with fixed radius of curvature ρ_0 and

$$C_\gamma = \frac{4\pi}{3}\frac{r_e}{(m_e c^2)^3} = 8.85 \times 10^{-5}\,\mathrm{m\,GeV^{-3}},$$

where m_e is the electron rest mass and r_e is the classical electron radius. Additionally, we use the global compression function

$$C_N = \frac{1}{Z_N} \tag{4.20}$$

and the inverse compression function

$$Z_N \equiv \frac{\partial z_N}{\partial z}\,. \tag{4.21}$$

The global compression function C_N represents the compression which is obtained for the particles in the neighbourhood of position z (position in the bunch after the source). If we want to have a linear compression, then we can enforce the first and second derivatives of the global compression equal to zero ($C_N' = 0$ and $C_N'' = 0$). The first and second

derivatives of the inverse global compression functions are related as

$$C'_N = -(C_N)^2 Z'_N, \qquad C''_N = 2(C_N)^3 (Z'_N)^2 - (C_N)^2 Z''_N \tag{4.22}$$

Our constraints can be then reformulated as conditions on the first and the second derivatives of the inverse global compression: $Z'_N = 0$, $Z''_N = 0$. In the general case we adjust the parameters Z'_N and Z''_N to make the current (particle density) profile symmetric and to avoid current spikes. For example, with the choice $Z'_N = 0$, $Z''_N > 0$ we will have a local maximum of the global compression function at the middle of the bunch and a weaker compression in the head and the tail.

In addition to the global compression function we have the partial compression function which describe the amount of compression after the i^{th} stage,

$$C_i = \frac{1}{Z_i}, \quad Z_i \equiv \frac{\partial z_i}{\partial z} \tag{4.23}$$

and its derivatives

$$Z_i \equiv z'_i, \quad Z'_i = z''_i, \quad Z''_i = z'''_i \,. \tag{4.24}$$

Setting up constraints in terms of the inverse compression functions therefore allows us to control the transformation of the longitudinal charge density. If instead the objective is to control the energy spread by setting the beam chirp, this can be done by also setting constraints in terms of the δ'_i, δ''_i and δ'''_i parameters in order to control the first, second and third order beam chirps since they correspond to

$$\frac{\partial \delta_i}{\partial z_i} = \frac{\delta'_i}{z'_i} = \frac{\delta'_i}{Z_i} \qquad Z_i \neq 0 \tag{4.25}$$

for the first order chirp,

$$\frac{\partial^2 \delta_i}{\partial z_i^2} = \frac{z'_i \delta''_i - \delta' z''_i}{z'^3_i} = \frac{Z_i \delta''_i - \delta'_i Z'_i}{Z_i^3} \qquad Z_i \neq 0 \tag{4.26}$$

for the second order chirp, also refered to as curvature, and

$$\begin{aligned}\frac{\partial^3\delta_i}{\partial z_i^3} =& \frac{z_i'(\delta_i'''z_i' - 3z_i''\delta_i'') + \delta_i'(3z_i''^2 - z_i'''z_i')}{z_i'^5} \\ =& \frac{Z_i(\delta_i'''Z_i - 3Z_i'\delta_i'') + \delta_i'(3Z_i'^2 - Z_i''Z_i)}{Z_i^5} \qquad Z_i \neq 0\end{aligned} \tag{4.27}$$

for the third order chirp. Using these two families of parameters to set up constraints allows us to differentiate between a linearly-compressed bunch and a linearized bunch.

Thence, we generate a system of equations describing the evolution of the longitudinal phase space of an electron bunch in an ERL analogous to eqns. (A1) and (A2) in ref. [66].Below we apply this method to a wide range of cases, organized as shown in Fig. 4.3, and study their limitations as well as presenting sample solutions of each of the longitudinal matches.

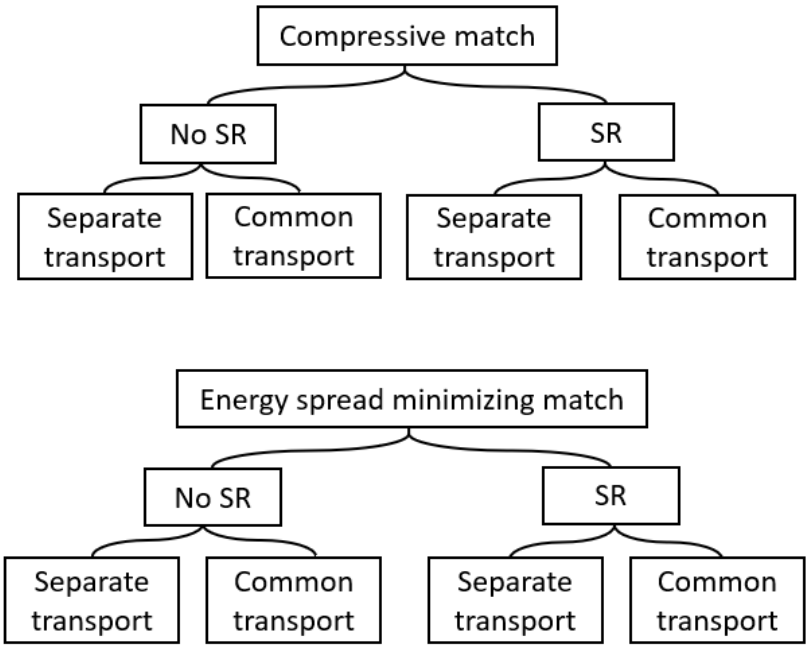

Figure 4.3: Classification of longitudinal matches for ERLs whose feasibility will be studied in this chapter.

4.4 Compressive match

A longitudinal match that increases the beam peak current from the injector to the interaction point must involve off-crest acceleration in at least one linac. By correlating the longitudinal position of the particles in the bunch with their energy, the bunch length and therefore peak current can be modulated by tuning longitudinal dispersion values. A fully compressed beam at the i^{th} stage satisfies the condition $Z_i = 0$.

How far off crest a viable match can be is constrained by the range of R_{56} available in the arcs, the energy acceptance of the arcs, and the overhead rf power available. It is advantageous to choose to accelerate on the falling side of the crest as, by doing so, one utilises the natural T_{566} of an arc to aid linearization [42] with a linearized bunch satisfying the condition

$$\left.\frac{\partial^2 \delta}{\partial z^2}\right|_{z=0} = 0\,.$$

For our first example, we then select the optimal decelerating phase as that which gives zero rf load balance and compensates the beam chirp on deceleration, resulting in minimum projected energy spread at the dump. This match is shown in Fig. 4.4. The beam is accelerated n times at the same rf phase. At the top energy a combination of **arc-like** and **chicane-like** sections with equal and opposite R_{56} values compress and decompress the bunch. As the compression and decompression of the bunch happens at the top energy arc, this match is available in both common and separate transport configurations.

4.5 Compressive match with SR loss compensation

The introduction of SR energy losses implies that the resulting rf load must change. We can choose to reduce the energy recovered by decelerating further off-trough than we accelerate. This change by itself however results in an overcompensation of the beam chirp, in turn, this can be corrected by modifying the decompressive R_{56}. By doing this we can match the accelerating and decelerating energies at a single arc, or at the dump,

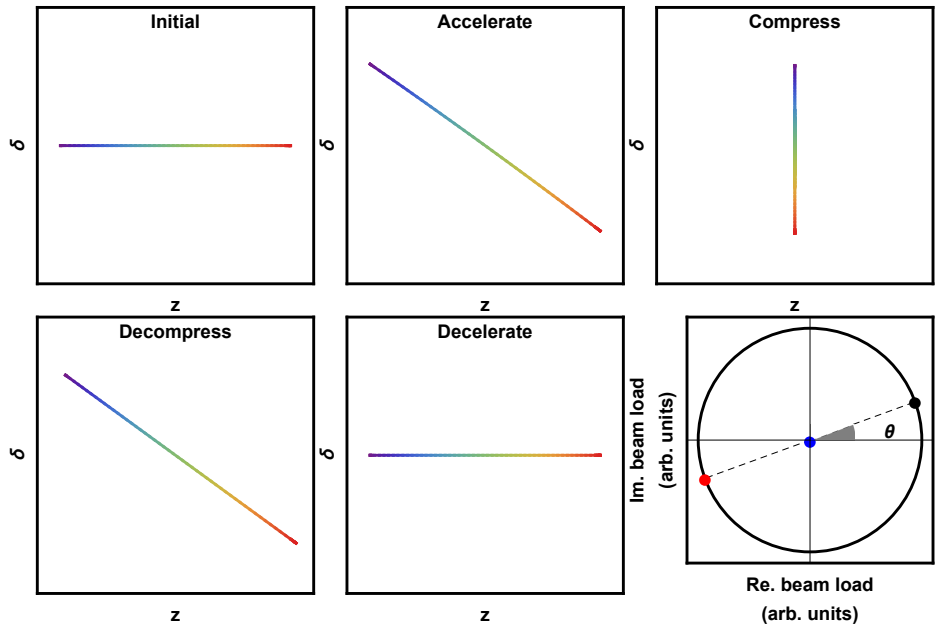

Figure 4.4: Compressive match. Sequence of longitudinal phase space manipulations maximizing bunch current at interaction point. From top left: Initial, accelerated, compressed, decompressed and decelerated charge distributions. Bottom right shows the total rf load in the complex plane with rf phase choices during acceleration (black), deceleration (red), and resulting beam load (blue). To achieve zero chirp after deceleration we must decompress with opposite sign R_{56} to that of the compression.

but not both. We are thus faced with two different scenarios depending on whether our transport is common or separate.

4.5.1 Separate Transport

In separate transport we retain independent control over all steps as there is no need to fit both accelerating and decelerating beams in a single arc energy acceptance. It is also possible to handle larger disruptions at the interaction point, such as increased energy spread due to an FEL [6, 22, 29]. The independent control of longitudinal dispersions enables linearization during acceleration and deceleration as well as bunch length control. This is illustrated in Fig. 4.5

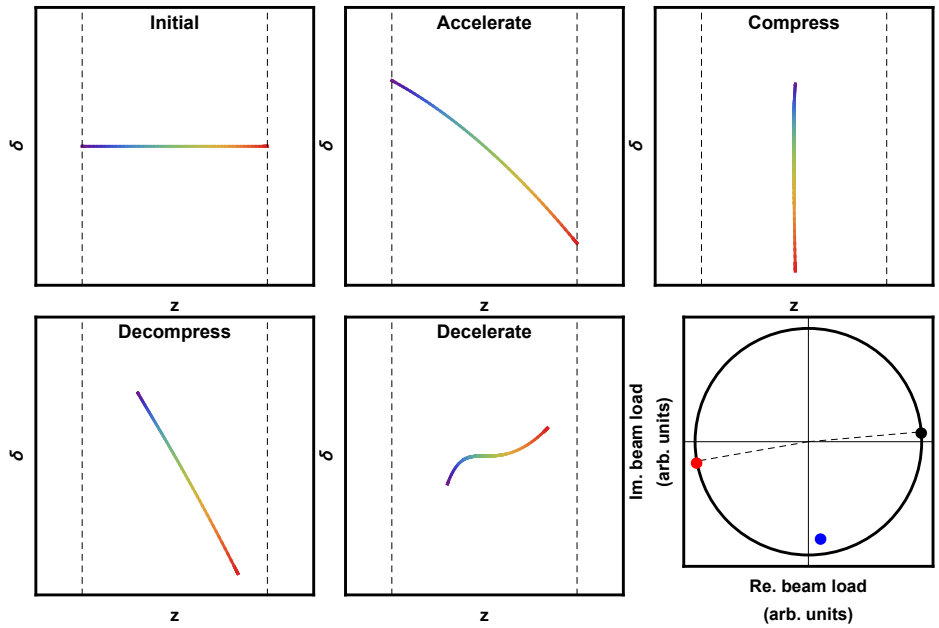

Figure 4.5: Compressive match with SR loss compensation. Image sequence as per Fig. 4.4. Choosing decompressing R_{56} of opposite sign to compressing now results in a shorter bunch length as we must move decelerating phase further off-trough to account for SR energy loss. The complex plane diagram shows the rf phase choices during acceleration (black), deceleration (red), and x 10 resulting beam load (blue) for clarity.

4.5.2 Common Transport

A comparison of the required energy acceptance between compressive longitudinal matches in common and separate transport is shown in Fig. 4.6. As the energy lost to SR increases, the difference between the average energy of accelerating and decelerating beams will also increase. First, limiting how far off-crest the accelerator can be run, and ultimately requiring unfeasibly large energy acceptance. Additionally, the path length symmetry between acceleration and deceleration passes does not match the energy asymmetry. Therefore, if we choose to match the energy compensation we cannot match the chirp compensation. One proposed method that has been suggested to remedy this is to include additional "SR compensating linacs". However as mentioned previously these must operate at a higher even harmonic to add energy to both accelerating and decelerating beams. Linearization, requiring odd harmonics, is not possible in this scenario thereby precluding a self-consistent longitudinal match.

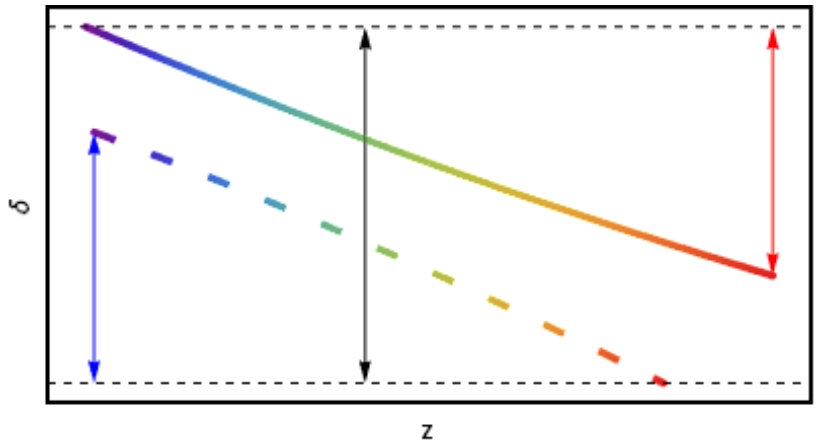

Figure 4.6: Longitudinal phase spaces of accelerating (solid) and decelerating (dashed) bunches in an intermediate arc. The required energy acceptance for common transport corresponds to the height of the black arrow. The required energy acceptance in the corresponding separate transport configuration corresponds to only the height of the red and blue arrows for the accelerating and decelerating arcs respectively.

4.6 Energy spread minimization

A longitudinal match that delivers to the interaction point a bunch with minimal energy spread can be obtained to first order by accelerating on crest. In this case the magnitude of the absolute energy spread will be determined by the rf curvature imprinted onto the bunch during acceleration. This can correspond to several times the slice energy spread depending on the bunch length, energy gain between injected bunch and top energy, and rf frequency.

In order to linearize the longitudinal phase space at the interaction point without using harmonic cavities, the bunch must be accelerated off-crest and the arc T_{566} adequately set. For the final acceleration one must switch to the opposite side of crest in order to cancel the chirp prior to the top energy arc and interaction region, resulting in a flat bunch in longitudinal phase space. There are then three different phase setups possible that satisfy these conditions, illustrated in Fig. 4.7:

(a) The simplest solution runs the first linac ahead of crest and the second linac equally far behind crest, Fig. 4.7a. The bunch is thus chirped into all odd arcs and dechirped

into all even arcs. The T_{566} of the odd arcs can be tuned to minimize the projected energy spread at the interaction point. As the beam energy increases, the beam chirp in higher acceleration passes decreases adiabatically, reducing the effect of our linearizing T_{566} in arcs 3 and above. During deceleration, the bunch undergoes the same chirp-dechirp sequence and the final rf beam load is zero in both linacs.

(b) Arc pathlengths can be set such that the first half of accelerating passes are on the same phase and the second half on the opposite side of crest. This set of phases enables sharing the linearizing effort between all the arcs, with decreasing impact of the second half of the arcs, Fig. 4.7b. During deceleration, the bunch has a chirp of the opposite sign which is compensated towards the dump and the final rf beam load is zero in both linacs.

(c) We may retune the previous solution such that the beam chirp from the first half of acceleration passes is completely compensated by the following pass, and the remaining accelerating passes are made on crest, Fig. 4.7c. This both maximizes the effect of our linearization in the low energy arcs, and minimizes the beam energy spread in the higher energy arcs. This results in an overall reduction of sensitivity to chromatic effects. However there is not a constant energy gain between consecutive arcs and there is an energy imbalance between the two linacs, i.e. one linac recovers more energy than it uses to accelerate the beam, and the other does the opposite. In this instance a twin-axis linac is required with an efficient transfer of rf power between the cavities [62, 68].

All these configurations rely on chirping the beam such that during transport, the natural T_{566} of the arcs has a linearizing effect. However, this significantly lengthens the low energy tail resulting in an overall longer bunch. This then covers more degrees of the rf waveform during deceleration resulting in larger energy spreads at the dump and potentially compromising the energy recovery. Instead, it is possible to set the phases such that the beam chirp has different signs as it travels through at least two of the arcs. By exchanging the role of the low energy tail in the two linearizing arcs we can keep bunch length under

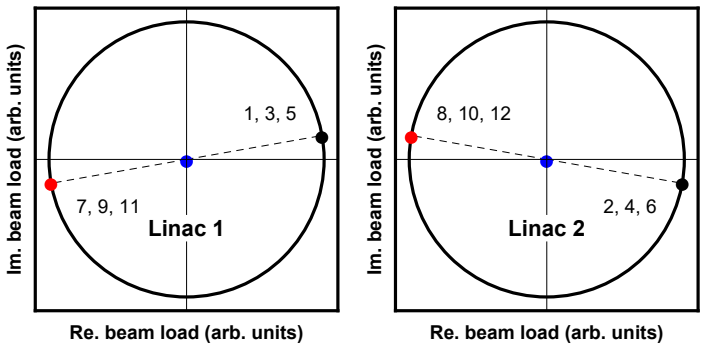

(a)

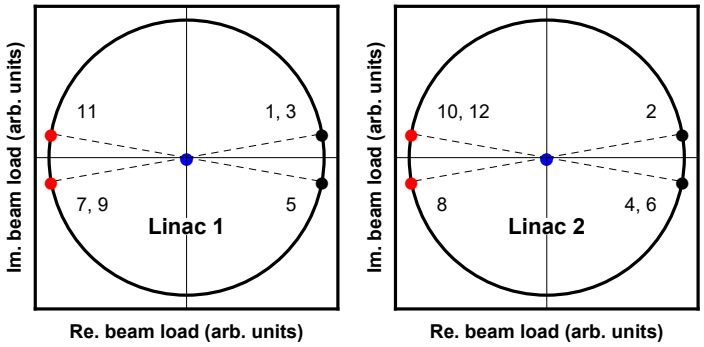

(b)

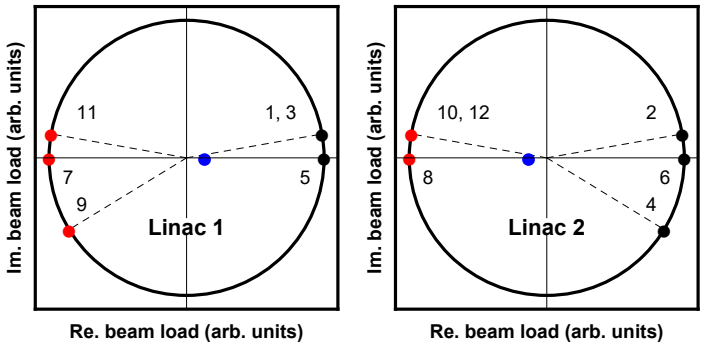

(c)

Figure 4.7: rf beam load plots for different phase configurations in common transport longitudinal matches that minimize beam energy spread. Applicable to e.g. PERLE. rf phase choices during acceleration (black), deceleration (red), and resulting beam load (blue) of each linac independently. Number labels indicate the ordering of the rf passes.

control. This however requires changing the sign of the T_{566} of one of the arcs. An example of a suitable match is shown in Fig. 4.8.

Overall, if all arcs are kept first order isochronous, all viable phase choices that minimize the beam energy spread at the interaction point have rf load vector sums lying on the

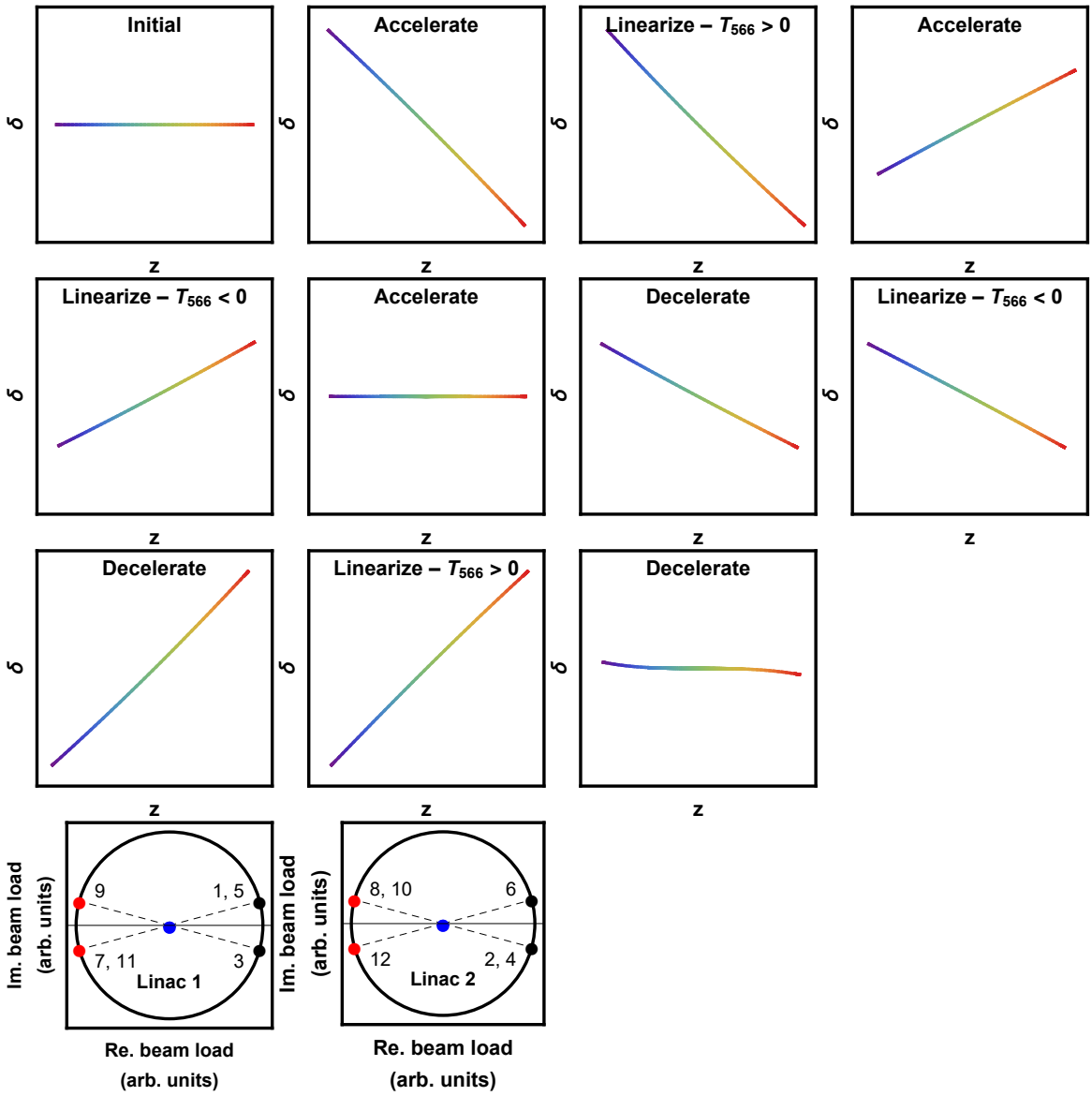

Figure 4.8: Energy spread minimization with common transport. Sequence of longitudinal phase space manipulations with two linearizing arcs with opposite sign of T_{566}. Beam load plots for the two linacs are shown underneath with labels indicating the order of each of the rf passes during acceleration (black), deceleration (red), and resulting beam load (blue) of each linac independently.

horizontal axis. Additionally, the path length shift into the decelerating passes is such that the phases are symmetric about the vertical axis and so the rf load vector sum lies at the origin.

Energy spread minimizing matches are not strictly required to have a zero R_{56}; the beam can have a zero chirp as it reaches the IP without having a purely-real resulting accelerating rf load. This series of longitudinal phase space manipulations are however limited by the requirement of a bunch at the dump to fit within the energy acceptance. Sample viable configurations are shown in Fig. 4.9, with Fig. 4.9a as a common transport example and Fig. 4.9b as a separate transport example. The common transport solution shows a longitudinal phase space at the dump with the characteristic shape of the decelerating rf curvature. This is because the intermediate arc is used to linearize towards the interaction point and therefore is not a free parameter to linearize the bunch towards the dump. On the contrary, the separate transport solution shows only a third-order dependence of δ on s at the dump since accelerating and decelerating arcs can be tuned to linearize the bunch at the IP and at the dump. Finally, comparing the rf loads in both cases, the common transport solution has a non-zero resultant rf load. It can be made zero in the separate transport case thanks to the independent control of the arc path lengths accelerating and decelerating.

4.7 Energy Spread Minimization with SR loss compensation

4.7.1 Common Transport

Proposed facilities above a few GeV cannot neglect SR energy losses. If these losses are small, the phase schemes above can be adapted by changing the path length of the top energy arc. However, this results in an overall chirp in the bunch as it reaches the dump. Therefore, the limits of this strategy are defined by the necessary decelerating phase shift

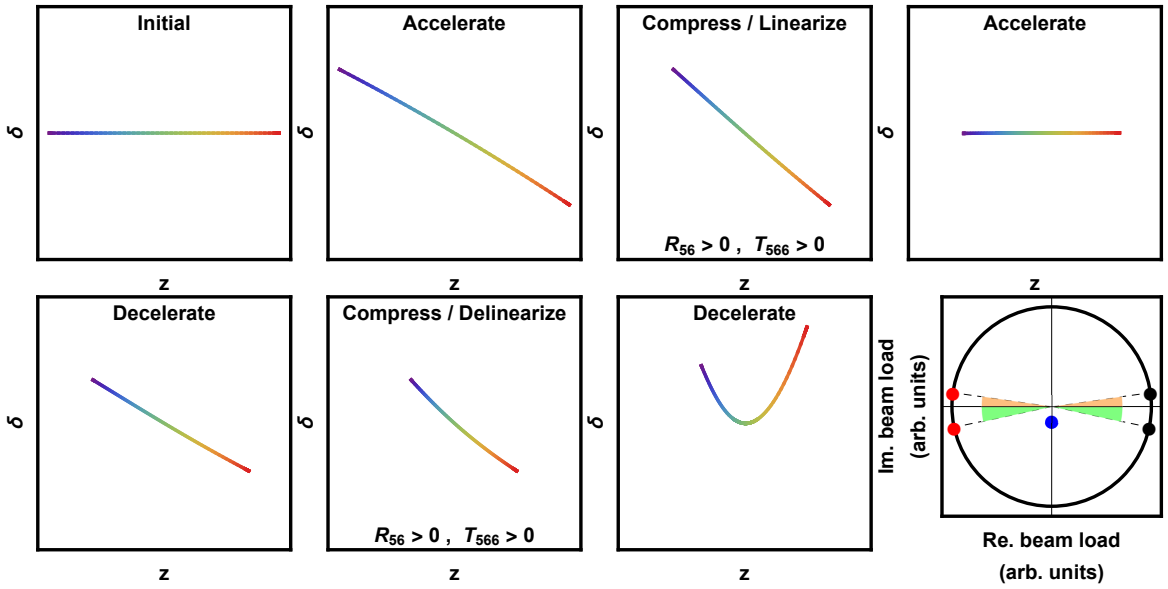

(a)

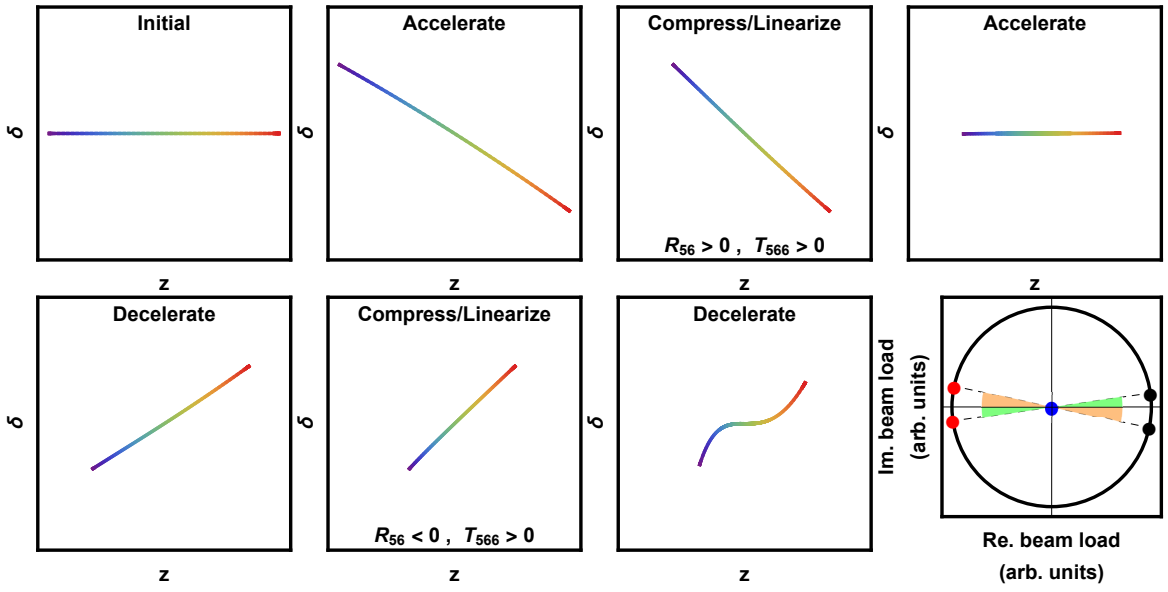

(b)

Figure 4.9: Energy spread minimizing matches with non-isochronous intermediate arcs. rf beam load plot shows rf phase choices during acceleration (black), deceleration (red), and resulting beam load (blue). (a) Common transport, (b) separate transport. Different angle highlights in the rf load plots correspond to accelerating/decelerating at different rf phases with respect to crest/through respectively.

to compensate for the losses, and by the energy acceptance of the arcs and dump.

For non-negligible energy loss, tuning the top energy arc path length can only match the decelerating energy at a single stage. This results in differences in centroid energies at all other stages, requiring very large energy acceptances in these arcs even before taking into account the bunch energy spread. Figure 4.10 shows the energy acceptance necessary in arc 1 of a 3-turn (accelerating and 3-turn decelerating) common transport ERL for a range of peak energies with energy losses corresponding to 180 degree arcs containing dipoles with a geometric radius of 336 m, similar to those proposed for LHeC [18]. For higher energy arcs the requirements diminish as the relative energy spread is adiabatically dampened.

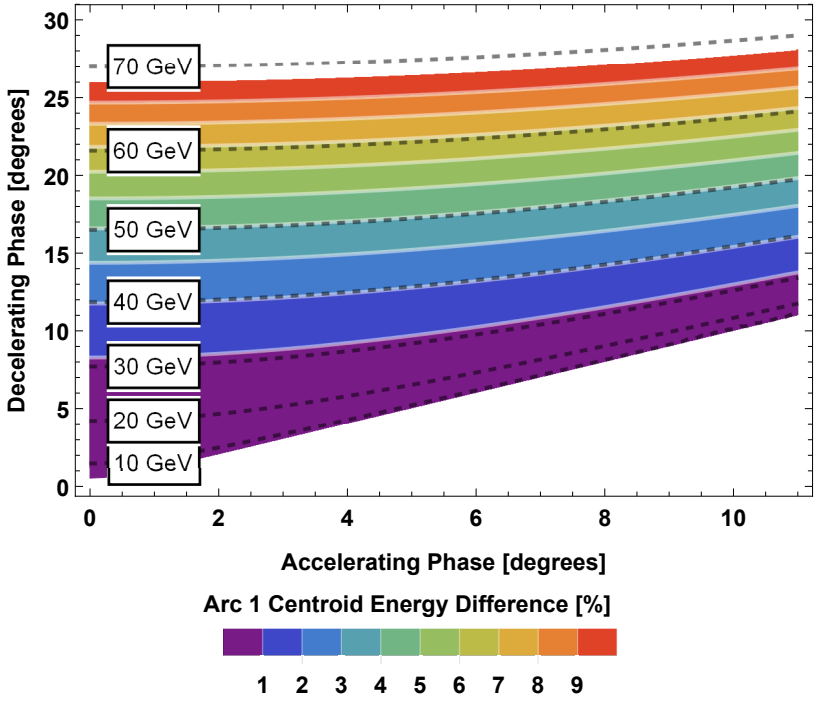

Figure 4.10: Arc 1 centroid energy difference between accelerating and decelerating beams for a range of accelerating and decelerating phases. Black dashed contour lines represent peak energy in GeV.

Alternatively, all arc path lengths may be used to set the rf phases such that the difference between accelerating and decelerating centroid energies is minimized, reducing the energy acceptance required [63]. Example results of such a minimization are shown in Table 4.1. We have shown previously that longitudinal matches that minimize energy spread at the

interaction point are possible even if the resulting accelerating rf load has a non-zero but small imaginary component. The rf phase choices necessary in this case result in very far off crest phases, in turn resulting in chirped beams with very large energy spread, a magnification of the effect shown in Fig. 4.6.

Table 4.1: Results of numerical optimization of arc path lengths and initial rf phases that minimize the difference in fractional momentum between accelerating and decelerating beams traversing the same arcs of a LHeC-like machine. $\theta_{1,1}$ and $\theta_{1,2}$ are the initial phases of the linacs, $\Delta\theta_1$ through $\Delta\theta_6$ are the phase changes between rf passes at each of the arcs and $\delta_{0,\min}$ through $\delta_{5,\min}$ are the fractional energy acceptances necessary to accommodate both the accelerating and decelerating beams from the Injector/Dump to arc 5. $\delta_{6,\min}$ not present as arc 6 is only traversed once.

Parameter	Value	Units
$\theta_{1,1}$	0.0	degree
$\theta_{1,2}$	-13.5103	degree
$\Delta\theta_1$	0.0	degree
$\Delta\theta_2$	-0.755549	degree
$\Delta\theta_3$	44.2088	degree
$\Delta\theta_4$	-13.6424	degree
$\Delta\theta_5$	13.5607	degree
$\Delta\theta_6$	100.057	degree
$\delta_{0,\min}$	0.819755	%
$\delta_{1,\min}$	0.593161	%
$\delta_{2,\min}$	0.768878	%
$\delta_{3,\min}$	0.693516	%
$\delta_{4,\min}$	0.647318	%
$\delta_{5,\min}$	0.822313	%

4.7.2 Separate Transport

A separate transport solution is readily available since accelerating and decelerating beams need not share the same centroid energy. Such a solution is shown in Fig. 4.11. In this example the bunch is accelerated off-crest in a similar fashion as the example of Fig. 4.7b with linearizations in arc 1 and arc 4. Then, the first 4 decelerating passes are further off-crest than their accelerating counterparts to compensate for the energy losses whilst keeping a purely-real resultant beam load in both linacs. The final two decelerating phases are equally as far off-crest as the accelerating passes to control the energy spread in the

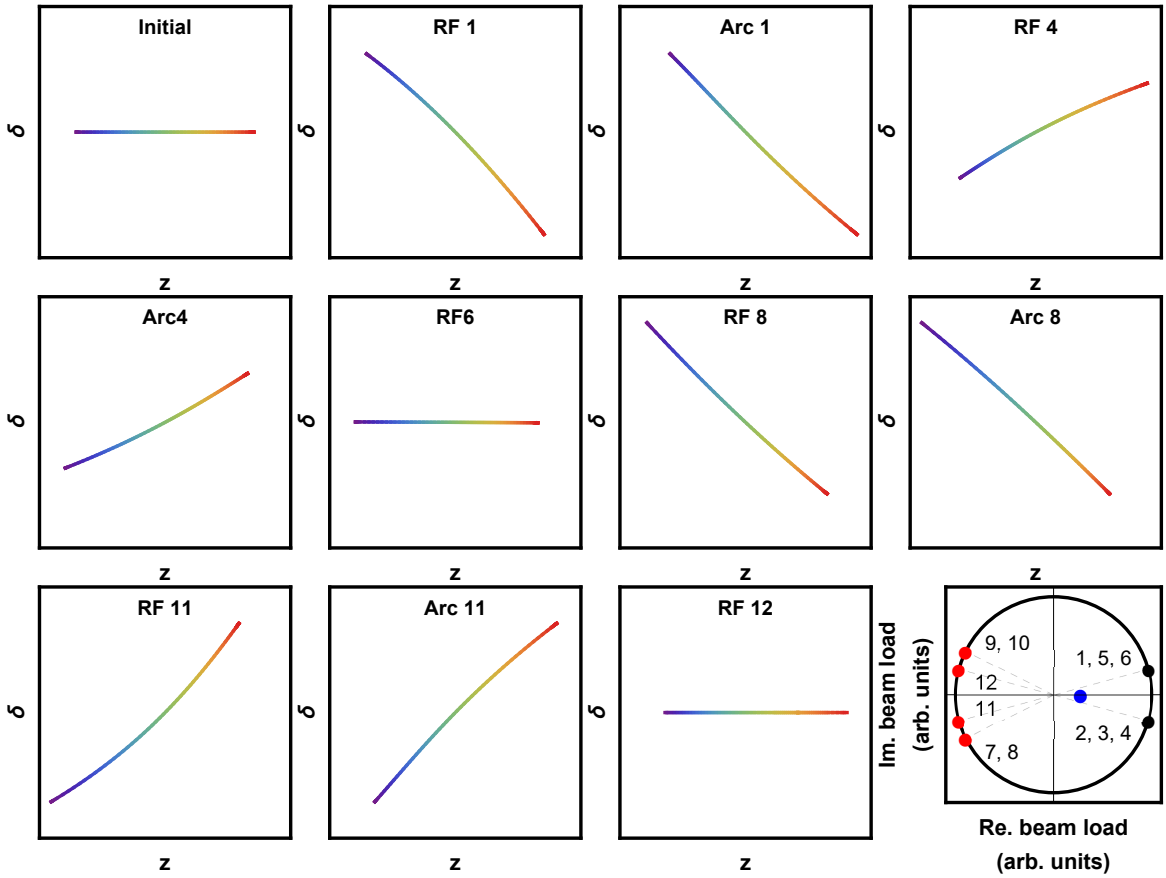

Figure 4.11: Energy spread minimizing match with SR loss compensation using separate transport. Shown longitudinal phase spaces correspond to the example beam at the exit of the element specified. Applicable to e.g. LHeC. rf beam load plot shows phase choices during acceleration (black), deceleration (red), and resultant (blue).

low energy arcs. Linearizations during deceleration occur in arc 8 and arc 10 (energy levels 4 and 1).

4.8 Bunch length control through alternate sign linearization

One method of increasing luminosity is to increase bunch charge by allowing longer bunches from an injector. Pre-compression of such bunches in an injector chicane or equivalent may not be optimal due to emittance degradation through collective effects.

However, linearization of the longitudinal phase space by controlling second order longitudinal dispersions during acceleration results in a compression of the high energy tail and elongation of the low energy tail. Depending on the strength of the linearization required, the resulting bunch elongation may not be tolerable. This bunch elongation can be controlled by splitting the linearization process into several steps and utilising arcs with T_{566} values with opposite signs. This can be achieved by pre-linearizing the bunch in an injection chicane before entering the main ERL loop, or by setting the accelerating rf phases such that in the first accelerating pass the beam chirp is of the opposite sign to that of the fully accelerated beam. This change in rf phase choices will result in an increment in the rf load for non-SR-compensating common transport configurations, and a larger centroid energy mismatch in the intermediate arcs of a SR-compensating common transport accelerator. Alternatively, as shown in Fig. 4.12 careful selection of a single linearizing arc can result in successful matches if the natural, non-zero T_{566} of the rest of the arcs is taken into account. In Fig. 4.12a we demonstrate a successful match by arranging a balance between a natural over-linearizing T_{566} of the arcs and the chosen arc 3 which is anti-linearizing. Conversely, in Fig. 4.12b we show the negative consequences if arc 1 is chosen to control the linearization: As we decelerate through arcs 5 to 2 the low energy tail is elongated and the high energy tail compressed, changing the profile of the curvature imprinted onto the bunch resulting in an energy spread for the fully-decelerated bunch which is much too large.

4.9 Strategies to mitigate common transport limitations

Employing the same arcs during acceleration and deceleration limits the control over path lengths and longitudinal dispersions, whilst sharing the same momentum acceptance. However, as previously shown in chapter 3, a more complex design of the beam transport can mitigate this.

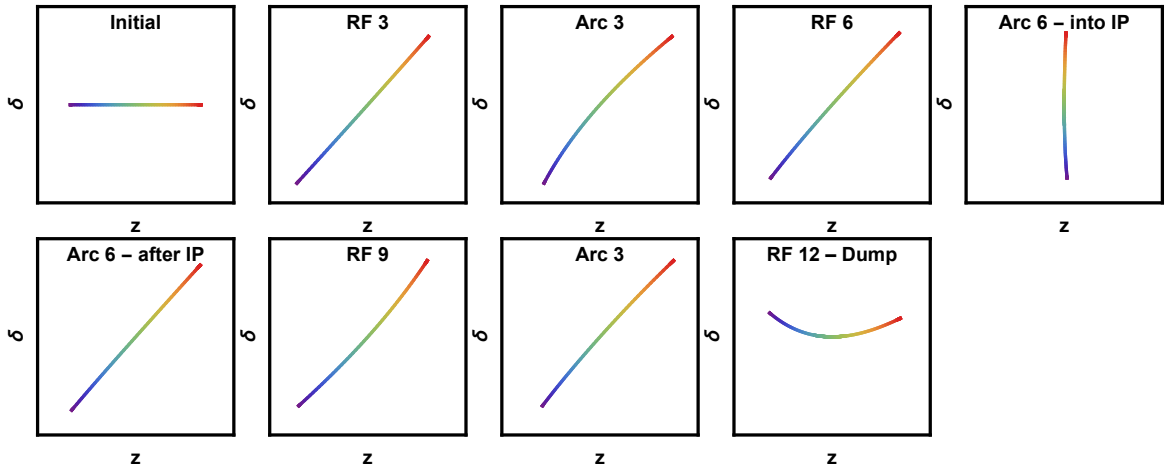

(a)

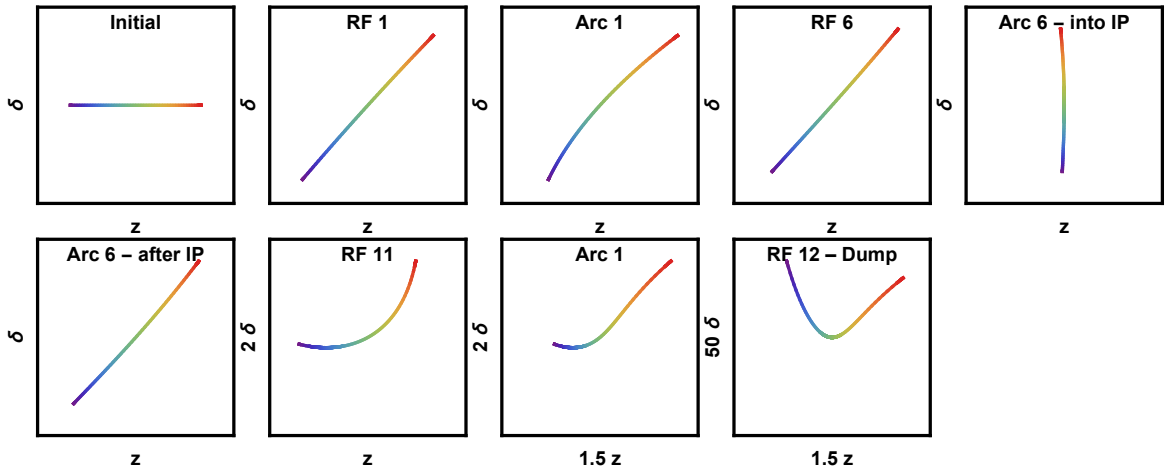

(b)

Figure 4.12: Sequences of compressive common transport longitudinal matches with different choice of linearizing arcs. Longitudinal phase spaces at the exit of the specified elements. The remaining arcs have a non-zero T_{566} of their natural sign. (a) uses arc 3 to linearize, (b) uses arc 1 to linearize. Note the change of scale in the later stages of (b).

In a common transport configuration, if the top energy arc cannot reach the necessary R_{56} values, a large T_{566} in the second-to-top arc may be set to compress accelerating bunches and decompress decelerating bunches as shown in Fig. 4.13. This is thanks to the difference in centroid energies between the accelerating and decelerating beams which correspond to the sum of SR losses and any energy lost at interaction. However, in doing this we must transport a compressed bunch for longer, risking collective effects degrading the bunch prior to interaction. Additionally, in order to effectively transport the beam in this arc, the

arc must have good chromatic behaviour over the whole range of the energy acceptance including zeroing higher-order transverse dispersions and chromatic amplitudes [40, 42].

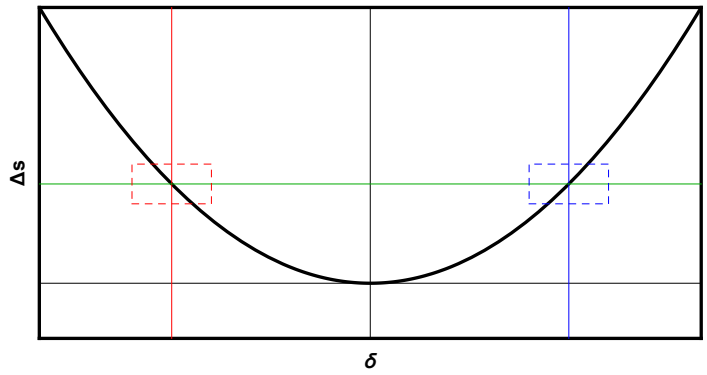

Figure 4.13: Arc path length as a function of relative momentum deviation with only second order longitudinal dispersion non-zero. Red and blue displaced axes highlight the path length dependence on momentum for off-momentum beams with an effective non-zero R_{56}.

The idea of exploiting the different beam energies accelerating and decelerating within the same arc can be extended to independently control the path lengths and linear longitudinal dispersions of both accelerating and decelerating beams with the right choice of on-momentum first, second and third order longitudinal dispersions. This added flexibility to common transport arcs would however require sextupoles and octupoles to adequately set the higher-order longitudinal dispersions while still keeping control over the transverse dispersions and chromatic amplitudes with a wide energy acceptance. Since this method does not provide control over the higher order dispersions as seen by the off-momentum beams, it is potentially useful to implement in arcs where the beam chirp is expected to be zero, and recuperate some path length control between accelerating and decelerating arcs. Figure 4.14 shows an example where the higher energy beam has a path length 5 mm longer than the lower energy beam and their effective R_{56} values are 0 mm and -10 mm respectively. The on-momentum longitudinal dispersions R_{56}, T_{566} and U_{5666} are 1.21 m, -24.2 m and $-35\,156$ m respectively.

We also consider a configuration where the top energy arc can only be used to compress the bunch, but not to decompress it, as shown in Fig. 4.15. In this case, we can set an intermediate arc R_{56} to have the opposite sign. With this scheme, the bunch decompression

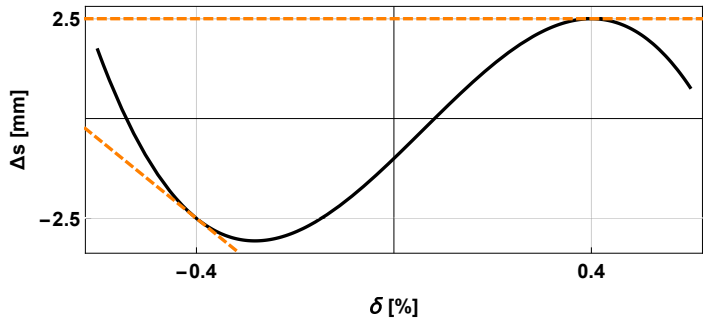

Figure 4.14: Arc path length as a function of relative momentum deviation where we choose reference momentum, first, second and third order longitudinal dispersions. This allows independent control over path length and R_{56} of two off-momentum beams. Example shows for two beams at $\delta = \pm 0.4\%$ the path length difference is 5 mm with effective $R_{56} = 0$ mm and -10 mm respectively, illustrated by the dashed orange lines.

(black and orange dashed lines) is larger during deceleration (green dashed line) thanks to the combination of the energy spread growth in the interaction region and the adiabatic growth of the relative energy spread in the decelerating rf phases between the top and the decompressing arc (red and blue dashed lines). This kind of longitudinal match is what we'll later propose for ER@CEBAF in chapter 5.

4.10 Parasitic crossings

Parasitic crossings, also know as overcompressions, where the bunch head and tail exchange places, provide an additional tool to find longitudinal matches in ERLs as, in effect, they allow the sign of the beam chirp during transport to change between linac passes. Within our model, this corresponds to a negative inverse global compression function, $Z_i < 0$. One could expect significant degradation to occur at a parasitic compression, and this would be of particular concern during acceleration [69, 70]. However if the minimum bunch length during this compression is relatively large due to the presence of uncompensated rf curvature at that location, such degradation would be not significant. One can picture this as the bunch "rolling" through a "banana" shape in the phase space, as opposed to standing totally upright.

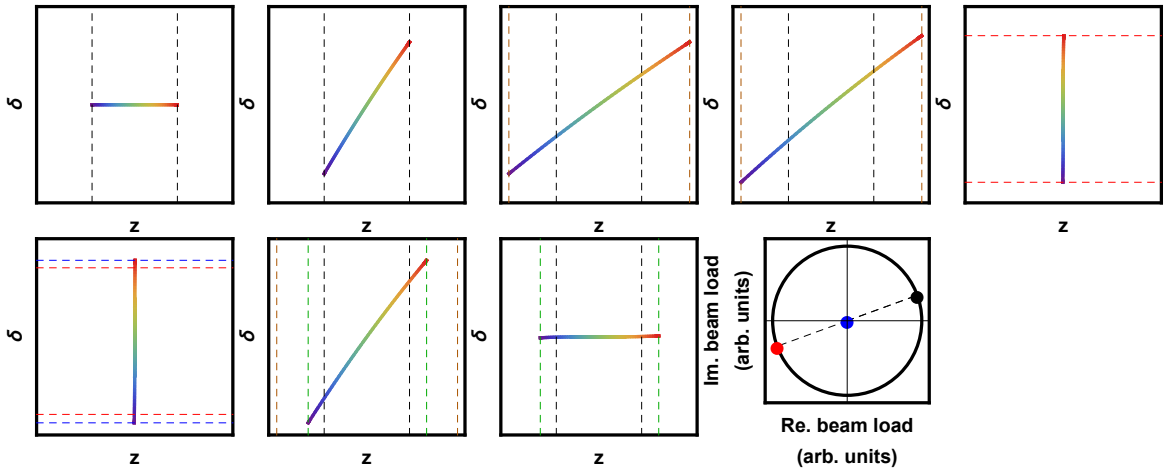

Figure 4.15: Equivalent of Fig. 4.5 but bunch decompression does not occur at top energy. The bunch undergoes decompressions during acceleration and deceleration resulting in a bunch longer at the dump than at the injector. Black dashed lines indicate initial bunch length, orange dashed line indicates maximum bunch length, green dashed line indicates final bunch length, red dashed line indicates bunch energy spread at top energy and blue dashed line indicates adiabatic growth of energy spread of the decelerating fully compressed bunch. rf beam load plot shows phase choices during acceleration (black), deceleration (red), and resultant (blue).

Bunch decompression immediately after the IP in a compressive match can be such that the bunch chirp is of the opposite sign before and after. The bunch undergoes a parasitic crossing and the bunch energy spread can still be compressed during deceleration by changing the side of trough it is decelerated on with the effect of an imaginary resultant beam load. The collective effects during this process will degrade the beam's emittance, however this happens after the interaction region and control of higher order longitudinal dispersion can be used to ensure energy recovery remains satisfied. This sequence of longitudinal manipulations is shown in Fig. 4.16.

First-order transformations like these, via control of R_{56}, can be used to control second-order parameters of our beam and completely or partially cancel the effects of the rf curvature, as shown in Fig. 4.17, such that it is then compensated by the remaining rf passes. In order to continue the chirp compensation, the subsequent passes must be on the opposite side of the waveform.

This mechanism, if implemented in a common transport configuration with shared longi-

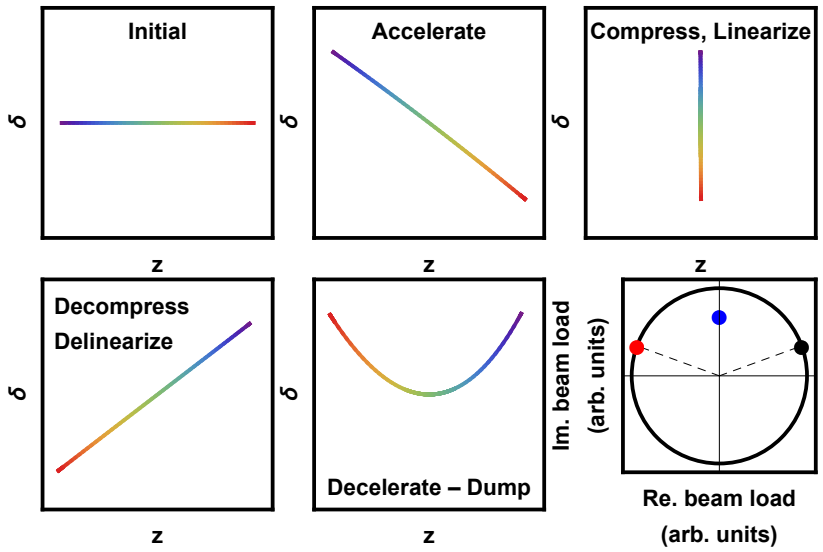

Figure 4.16: Equivalent of Fig. 4.5 but with utilisation of a parasitic crossing and deceleration on opposite side of rf trough in order to remove linear chirp. This results in a large imaginary resultant rf load. We see residual curvature as the natural T_{566} value of the arcs add to the rf curvature for deceleration on falling side of trough. rf beam load plot shows phase choices during acceleration (black), deceleration (red), and resultant (blue).

tudinal dispersions and arc path-lengths requires parasitic crossings during acceleration, deceleration and at top energy, as shown in Fig. 4.18. The parasitic crossing during acceleration would have the same linearizing effect as during deceleration, but it would also increase the beam emittance before the interaction point. This alternative method of linearization is also applicable in energy spread minimizing matches with the exception of crossings happening at the top energy since the beam would have zero chirp at that point.

The separate transport configurations' independent control over each arc's longitudinal dispersions enables the use of these transformations during deceleration without compromising the beam quality before it reaches the interaction region. As the beam quality constraints during deceleration are relaxed, a separate transport system can also compress the bunch during deceleration to cope with the energy spread increases expected from an FEL interaction. This is showcased in Fig. 4.19, showing the beam during acceleration without compressions or parasitic crossings and during deceleration after doubling its energy spread.

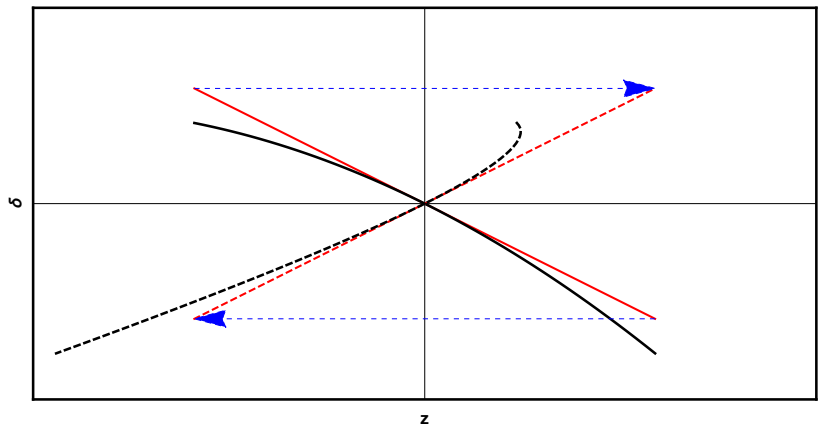

Figure 4.17: Change in curvature as an example bunch (black) undergoes a linear compression (solid to dashed). The same compression acting on a linearized bunch is shown in red.

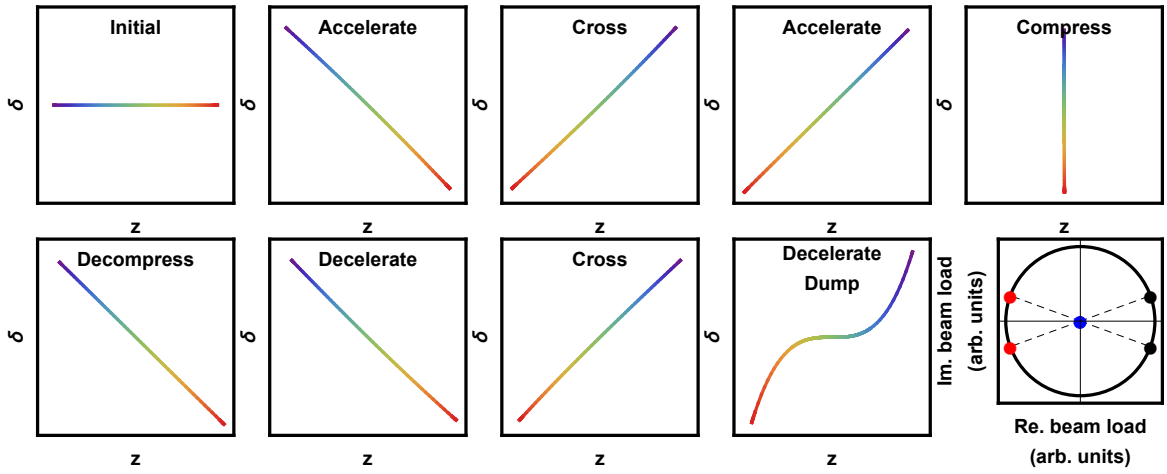

Figure 4.18: Longitudinal match solutions using parasitic crossings to cancel rf curvature in common transport. rf beam load plot (bottom right) shows phase choices during acceleration (black), deceleration (red), and resultant (blue).

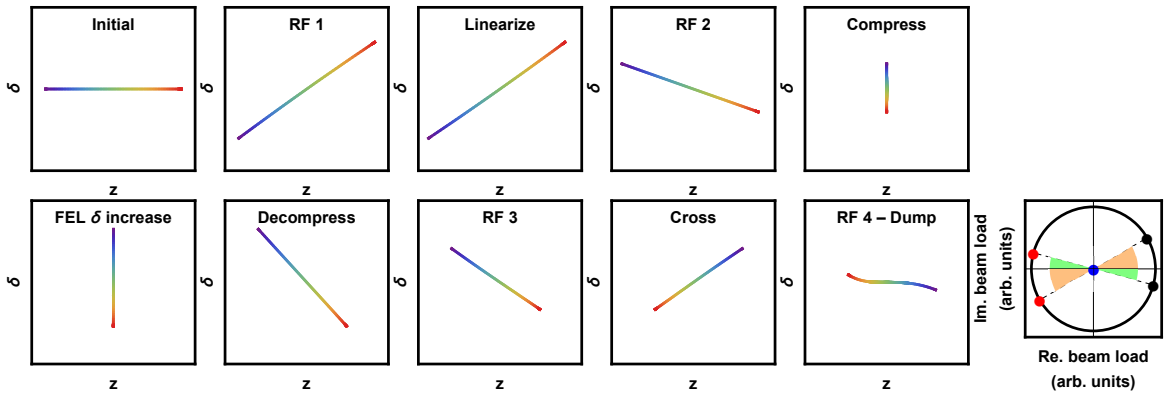

Figure 4.19: Compressive longitudinal match with energy spread growth at the interaction point. Longitudinal phase spaces during acceleration (top) and during deceleration (bottom) with a parasitic crossing. rf beam load plot (bottom right) shows phase choices during acceleration (black), deceleration (red), and resultant (blue). Different angle highlights in the rf load plots correspond to accelerating/decelerating at different rf phases with respect to crest/through respectively.

4.11 Conclusions

In this chapter we have shown our method of finding possible longitudinal matches for a wide range of multi-pass ERL configurations comprising compressive matches and energy spread minimising matches for common transport and separate transport topologies and with and without synchrotron radiation compensation as summarized by Fig.4.3. We conclude that for systems with negligible energy losses, arc path length and longitudinal dispersion configurations exist for both compressive matches and energy spread minimising matches for both common transport and separate transport topologies, although common transport matches will require a more intricate linearizaiton scheme to obtain linearized bunches at both the interaction point and dump.

If synchrotron radiation energy losses must be compensated, we show solutions for compressive matches and energy spread minimising matches for separate transport configurations. Synchrotron radiation compensating compressive matches are also available in common transport configurations. However, synchrotron radiation compensating energy spread minimising matches in a common transport configuration require transport between rf passes with energy acceptances of a few % as shown in Fig. 4.10 or require strong bunch

length modulations including parasitic crossings throughout all of the transport, especially if peak energies are in the range of $\gtrsim 50\,\mathrm{GeV}$ as proposed for LHeC.

Throughout this analysis, no collective effects have been taken into account. The two collective effects that will have the highest impact on the longitudinal phase space will be coherent synchrotron radiation (CSR) and longitudinal space charge (LSC). CSR will lower the energy at the centre of the bunch with respect to the tails. This is opposite to the curvature imprinted by the rf on an accelerating beam and thus will reduce our linearization requirements. However, during deceleration, the changes in the longitudinal phase space from CSR will add to the decelerating rf curvature which, together with the adiabatic growth of the energy spread during deceleration, will result in a significant energy spread at the dump if not accounted for. LSC can be introduced in our considerations by tracking the bunch through the low energy sections [71] and taking the pre-accelerated bunch as the start of our analysis and tracking the last decelerating pass towards the dump.

With these caveats, we have demonstrated a methodology for designing multi-pass ERLs for a wide range of applications. Specific applications of this method are showcased in chapter 5 for ER@CEBAF, enabling it as an FEL driver and in chapter6 for PERLE, as a LHeC demonstrator for nuclear physics experiments.

Chapter 5

Longitudinal beam dynamics in ER@CEBAF

5.1 ER@CEBAF

ER@CEBAF's objective is to perform commissioning and tolerance studies for high energy ER at 1-pass (in similar conditions to the 2003 CEBAF-ER experiment) and at 5-pass regarding 6D bunch phase space preservation [13]. A schematic of the ER@CEBAF layout is shown if Fig. 5.1 and an overview of machine and beam parameters for ER@CEBAF is shown in tables 5.1 and 5.2.

Table 5.1: ER@CEBAF machine parameter list, adapted from [13].

Parameter	Value/Range	Units	Description
f_{rf}	1497.0	MHz	Standard CEBAF rf frequency
λ_{rf}	20	cm	Standard CEBAF rf wavelength
E_{linac}	700	MeV	Energy gain per linac pass, baseline
N_{passes}	1, 5	—	Number of machine passes before energy recovery
$\phi_{\mathrm{FODO,NL}}$	60	degrees	Phase advance per cell, north linac
$\phi_{\mathrm{FODO,SL}}$	60	degrees	Phase advance per cell, south linac
ϕ_{tol}	0.25	degrees	Required path length control tolerance

Within the wider context of our work are the practical applications of ERLs in free-electron

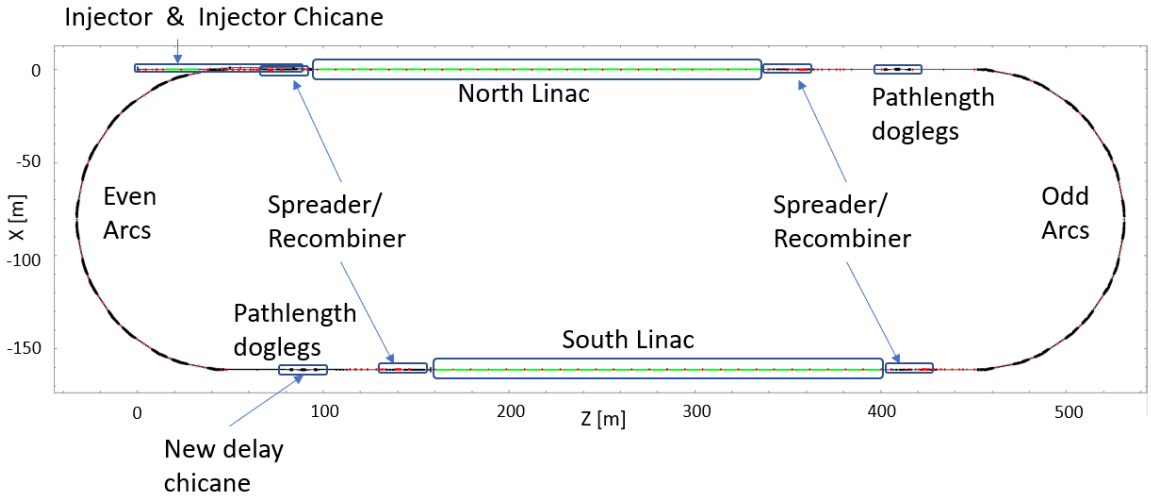

Figure 5.1: Schematic of the ER@CEBAF Layout.

Table 5.2: ER@CEBAF beam parameter list, adapted from [13].

Parameter	Value/Range	Units	Description
$f_{\mathrm{beam,CW}}$	249.5	MHz	Standard CEBAF CW bunch repetition frequency
$I_{\mathrm{beam,maxCW}}$	100	μA	Maximum CW beam current
$q_{\mathrm{bunch,maxCW}}$	0.2	pC	Bunch charge (at 100 µA CW)
$\sigma_{\mathrm{bunch,L}}$	90-150	μm	Bunch length (high energy)
$\epsilon_{\mathrm{x,y,rms,inj}}$	10^{-8}	m-rad	Transverse RMS geometric emittance at injector
dp/p_{inj}	$< 10^{-4}$	—	Momentum/energy spread at injector

lasers, inverse Compton scattering sources and internal gas-target interactions, as all these benefit from the high average power and high luminosity available in an ERL. Therefore we set off to modify ER@CEBAF to demonstrate XFEL-like compressive match and prove it can be done.

5.2 Proposed modifications for a compressive match

As introduced in section 4.2, a common transport ERL like ER@CEBAF presents a series of local and global constraints that must be satisfied to allow for ER operation.

- The target beam energies must be achieved at the interaction region and at the beam dump.

- At least at these two points, the longitudinal phase space of the bunches must satisfy the requirements for the desired experiment and safe beam dump respectively.
- It must be able to withstand and transport disruptions from the interaction region with very low losses.
- At every point in the system, the beam energy spread must fit within the energy acceptance. This is particularly pertinent in common transport configurations, where both accelerating and decelerating beams of the same energy level must fit within the same energy acceptance of the common transport.

In order to satisfy these constraints we depend on a series of high-level tuning parameters at CEBAF:

- The beam centroid energy can be controlled by our choice of rf voltage and phase.
- The constraints on beam energy spread can be relaxed by increasing the momentum acceptance of the arcs and by introducing adequate chirp compensation during deceleration.
- The desired high peak current at the interaction region can be obtained by setting the top energy arc R_{56} value and adopting an adequate linearization scheme.
- The desired low peak current during transport can be controlled by changing the bunch length before the beam enters the main ERL loop, tuning the injector chicane, and by controlling the intermediate arc R_{56} values.

5.2.1 rf phase

The operation of an ERL is based on the control of path lengths between successive passes through the rf cavities as introduced in section 4.2. At the defined top energy transport, a path length change corresponding to a π phase shift into the next rf cavity results in deceleration and thus energy recovery from the spent beam. With a top energy of 7 GeV

we must take into consideration in our energy balance the energy lost to synchrotron radiation, about 14 MeV. A detailed view of the energy values at each of the passes is shown in table 5.3.

Table 5.3: Pass-by-pass beam energies for ER@CEBAF. All energies in MeV. ΔE is energy lost to SR in each arc. Adapted from [13].

Arc (accelerating)	E_{entrance}	E_{exit}	ΔE	$E_{\text{loss,cumulative}}$
1	779.00	779.00	0.00	0.00
2	1479.00	1478.98	0.02	0.02
3	2178.98	2178.88	0.10	0.12
4	2878.88	2878.73	0.15	0.27
5	3578.73	3578.37	0.36	0.63
6	4278.37	4277.89	0.49	1.11
7	4977.89	4977.00	0.89	2.00
8	5677.00	5675.49	1.51	3.51
9	6375.49	6373.10	2.40	5.90
10	7073.10	7070.37	2.72	8.63
Arc (decelerating)	E_{entrance}	E_{exit}	ΔE	$E_{\text{loss,cumulative}}$
9	6371.83	6369.44	2.39	11.02
8	5670.90	5669.40	1.50	12.52
7	4970.85	4969.97	0.89	13.40
6	4271.42	4270.94	0.48	13.88
5	3572.39	3572.04	0.35	14.24
4	2873.50	2873.35	0.15	14.39
3	2174.80	2174.71	0.10	14.48
2	1476.16	1476.14	0.02	14.50
1	777.60	777.59	0.01	14.51
Dump	79.04	—	0.00	14.51

Without other sources of energy for the beam, like harmonic cavities, to top up the beam energy pass-by-pass, if the beam makes a π phase shift into decelerating mode the energy mismatch between accelerating and decelerating beams while traversing the same arc may exceed the energy acceptance of our transport system. Alternatively, we can change the decelerating rf phase by deviating from the π phase shift and so reduce our energy recovery efficiency to guarantee adequate energy correspondence between accelerating and decelerating beams traversing the same arcs as shown in Fig. 5.2. In order to maintain the energy gain per linac pass, the on crest energy gain must be scaled as we go off-crest

following

$$\Delta E_{\mathrm{peak}} = \frac{700\,\mathrm{MeV}}{\cos(\theta_{\mathrm{rf}})} \tag{5.1}$$

which for a far off-crest pass of 20° corresponds to a peak energy gain of 744.924 MeV, which is within the target range for ER@CEBAF of 700 to 750 MeV.

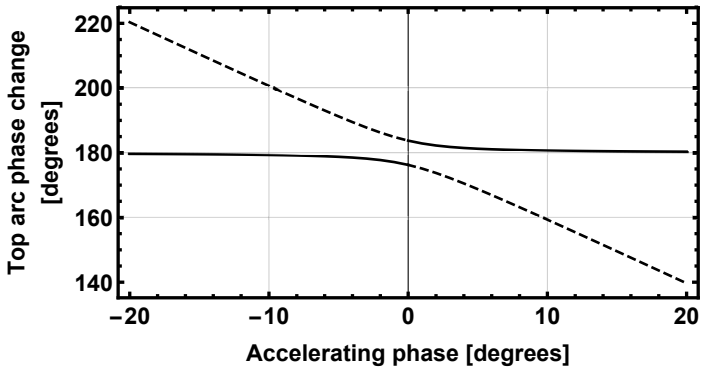

Figure 5.2: Top energy arc phase shift as a function of accelerating phase such that accelerating and decelerating beams have the same energy in arc 1. Dashed lines correspond to solutions where beam chirp is not compensated during deceleration.

In principle, arc path lengths could be set up such that on a pass by pass basis, the difference between the energy gained accelerating and the energy recovered decelerating corresponded to the energy lost to SR. This however would significantly change the energy ratios between the arcs requiring a redesign of the spreader-recombiner systems as well as imprinting pass by pass a chirp into the beam that can only be compensated for with parasitic compressions where the bunch goes through a minimum bunch length while electrons at the head and tail exchange their positions. An example of the rf load diagrams for such a solution is shown in Fig, 5.3 with the corresponding calculations for the beam energy shown in table 5.4.

Several issues make this solution impractical in the specific context of ER@CEBAF. The 9th and 10th accelerating passes are 80.1° and 74.0° off-crest respectively, this, in turn, results in a very small energy gain in the final accelerating pass with a peak energy of 5.43 GeV for an on-crest linac gain set to 700 MeV. Additionally, this solution has a resultant rf load with a very large imaginary component that would hamper rf stability. Finally, the path length flexibility required to obtain this set of rf phases is outside of the

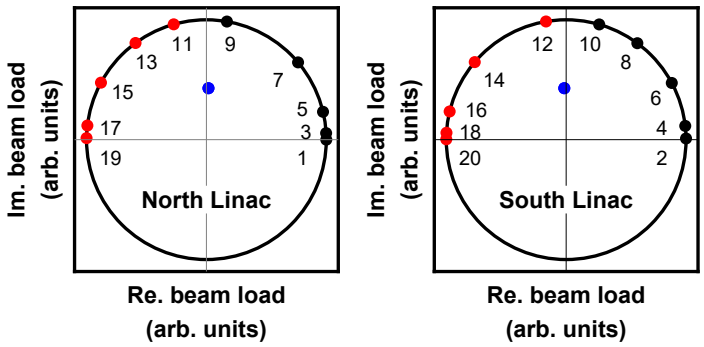

Figure 5.3: rf beam load plot for North and South linacs showing phase choices during acceleration (black), deceleration (red), and resultant/10 (blue) such that beam energies are matched during acceleration and deceleration. Number labels indicate the order of the linac passes.

capabilities of the path length chicanes currently installed in CEBAF. Therefore we don't pursue this phase configuration any further or its complementary solution where phases have the opposite sign.

5.2.2 Injector chicane

In a common transport ERL, the beam traverses the same arcs accelerating and decelerating. Therefore, to facilitate longitudinal manipulations, we preferably employ sections before injecting into the ERL loop and the top energy arc, as the beam only goes through them once. We propose the addition of two pairs of sextupoles into the injection chicane, with a schematic shown in Fig. 5.4 to gain control over the second-order horizontal dispersion T_{166} and second-order longitudinal dispersion T_{566}. The range of T_{566} values available is shown in Fig. 5.5. This control over the second-order longitudinal dispersion in the injector chicane will allow us to pre-linearize our bunch without having to only rely on the arcs.

Table 5.4: Pass-by-pass beam energies for ER@CEBAF. Arc path lengths adjusted to match accelerating and decelerating energies. On crest energy gain set to 700 MeV

Stage	Energy Accelerating (MeV)	Energy Decelerating (MeV)
Injector/Dump	79	79
Arc 1 entrance	779	779
Arc 1 exit	778.997	778.997
Arc 2 entrance	1478.96	1478.96
Arc 2 exit	1478.94	1478.94
Arc 3 entrance	2177.90	2177.90
Arc 3 exit	2177.80	2177.80
Arc 4 entrance	2873.19	2873.19
Arc 4 exit	2873.04	2873.04
Arc 5 entrance	3553.90	3553.90
Arc 5 exit	3553.56	3553.56
Arc 6 entrance	4170.34	4170.34
Arc 6 exit	4169.68	4169.68
Arc 7 entrance	4704.82	4704.82
Arc 7 exit	4704.12	4704.12
Arc 8 entrance	5119.79	5119.79
Arc 8 exit	5118.80	5118.80
Arc 9 entrance	5238.50	5238.50
Arc 9 exit	5237.41	5237.41
Arc 10 entrance	5430.39	—
Arc 10 exit	5429.45	—

5.2.3 Arc modifications

A longitudinal match like the one required to drive an FEL where the bunch is to be compressed and decompressed requires accelerating off-crest. This increases the energy spread which together with residual energy mismatches in the arcs between accelerating and decelerating beams requires an increase of the arcs' energy acceptances, limited by the peak dispersion values.

In order to increase the energy acceptance of the arcs, the polarities of arc quadrupoles in charge of dispersion control are flipped [72], trading high dispersion peaks for larger vertical Twiss functions. This results in an overall reduction of peak dispersion values in the arcs of a factor of 2 with the exception of Arc 1 where, in order to maintain a zero longitudinal dispersion, dispersion peaks are only reduced by a factor of 1.6 as shown in

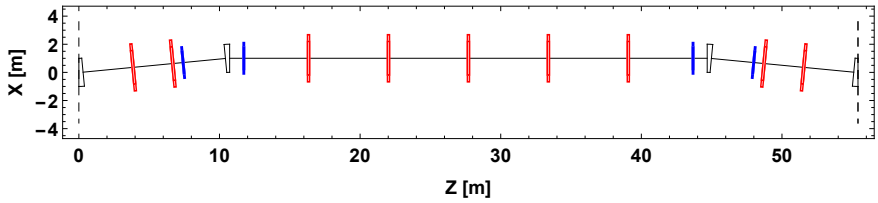

Figure 5.4: CEBAF's injector chicane layout with additional sextupoles. Dipoles in black, quadrupoles in red and sextupoles in blue.

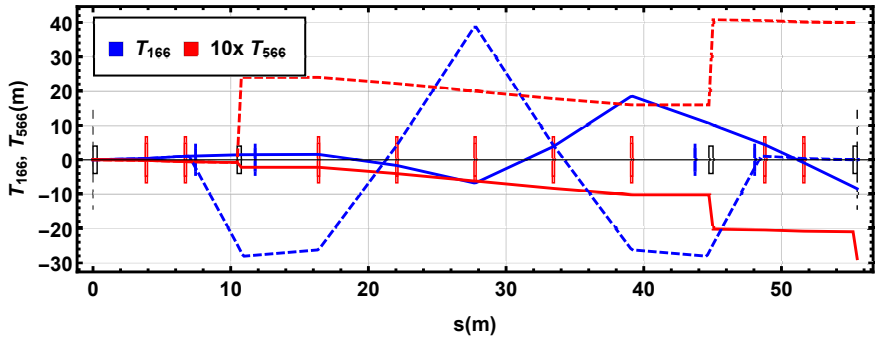

Figure 5.5: Second-order horizontal (blue) and longitudinal (red) dispersions in the CEBAF's injector chicane with (dashed) and without (solid) additional sextupoles.

Fig. 5.6. It must also be noted that this approach is only effective while the peak horizontal dispersion in the arc is larger than the peak vertical dispersion in the spreader/recombiner system, at that point the largest of both dispersions will be the limiting factor in the energy acceptance. In all the arcs, the change in quadrupole settings to reduce the dispersion peaks results in an optics configuration within the arc with larger peaks of particularly the β_y function. Additionally, the optics in the matching sections also need to be adapted accordingly. The reduced dispersion scheme results in a reduction of the natural T_{566} of all arcs. The initial and final Twiss functions correspond to the optics into and out of the linacs which remain the same in all cases except for arcs 9 and 10. These two top-energy arcs have also been set to be non-isochronous as determined later for our longitudinal match. The small irregularities in the periodicity of the optics within the arcs observable for arcs 4, 5, and 9 correspond to the inclusion in our simulation of the small measured magnetic quadrupole component of the arc dipoles. Similar plots for the rest of the arcs are shown in Figures A.1 through figure A.5 respectively.

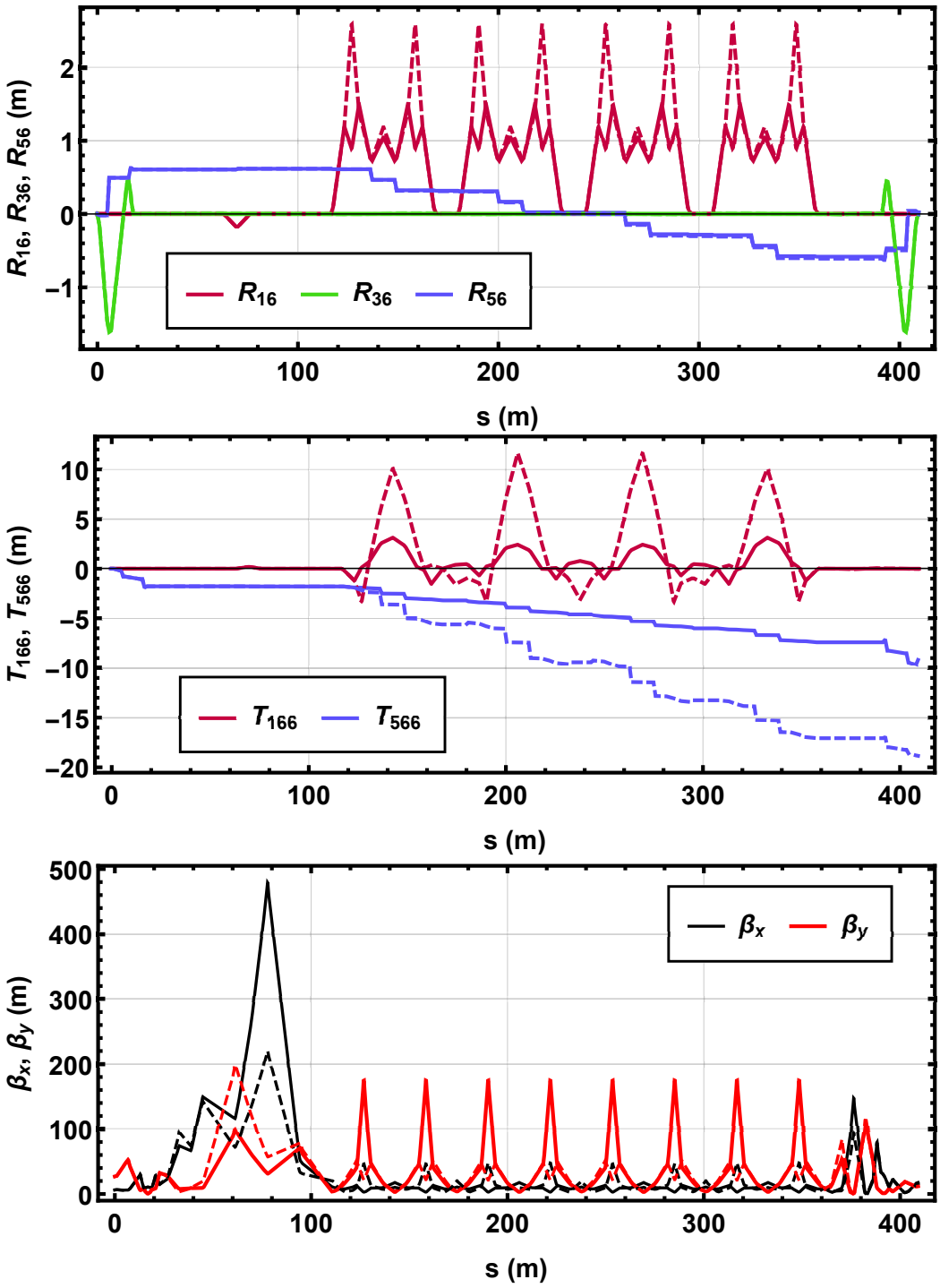

Figure 5.6: Initial (dashed) and reduced dispersion configuration (solid), first and second-order dispersions and optics (top, middle and bottom respectively) of CEBAF's Arc 1.

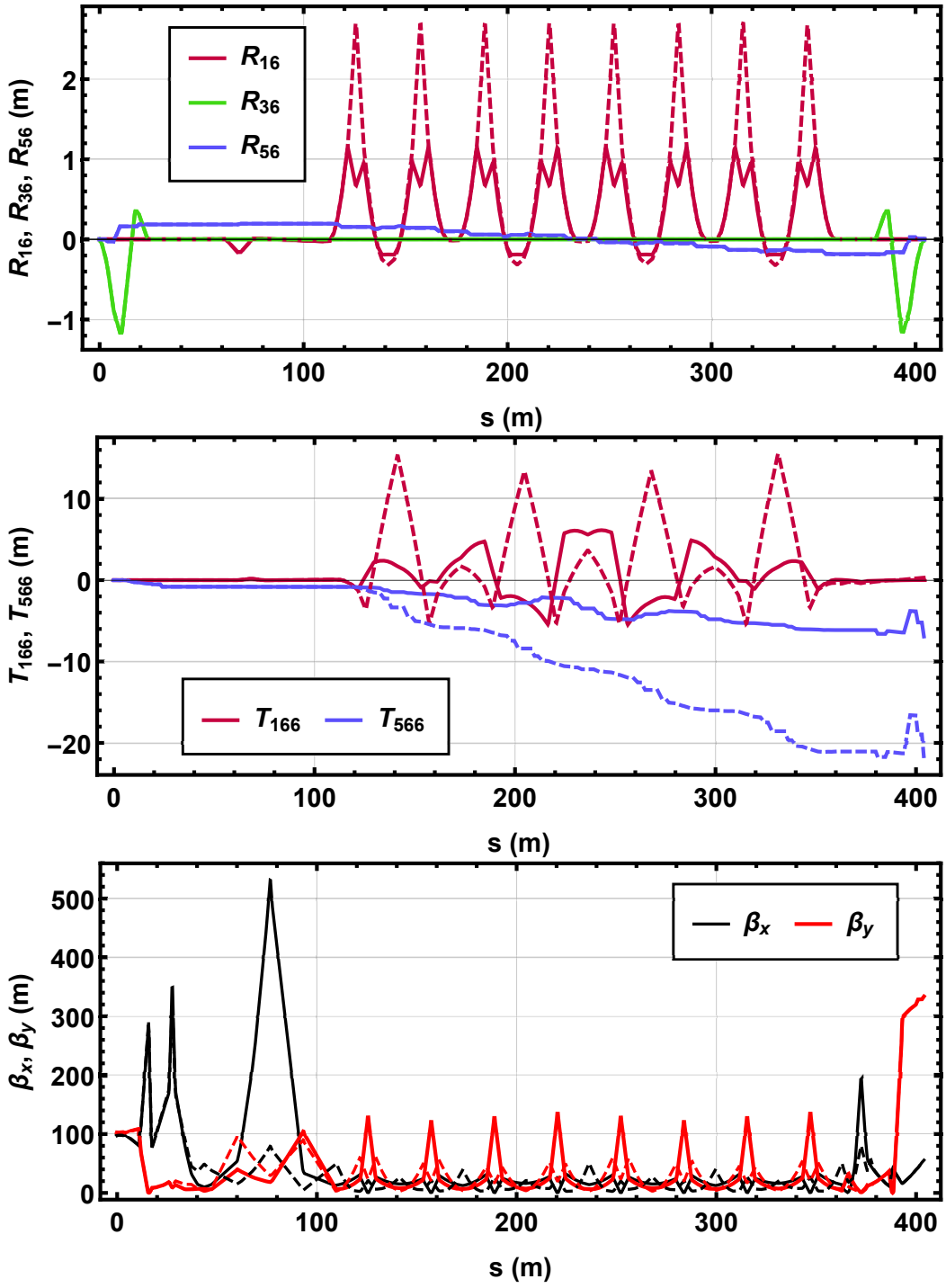

Figure 5.7: Initial (dashed) and reduced dispersion configuration (solid), first and second-order dispersions and optics (top, middle and bottom respectively) of CEBAF's Arc 4.

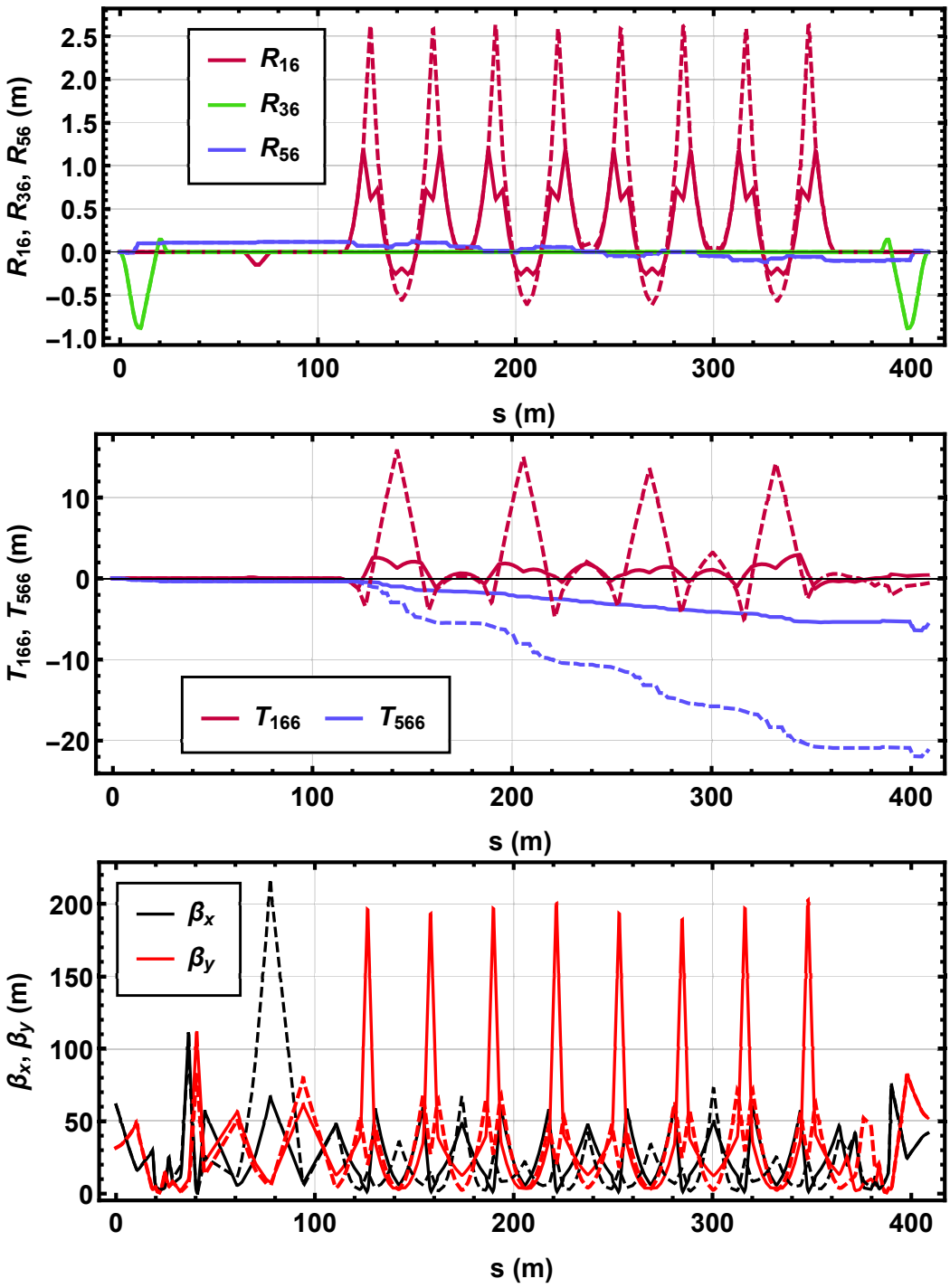

Figure 5.8: Initial (dashed) and reduced dispersion configuration (solid), first and second-order dispersions and optics (top, middle and bottom respectively) of CEBAF's Arc 5.

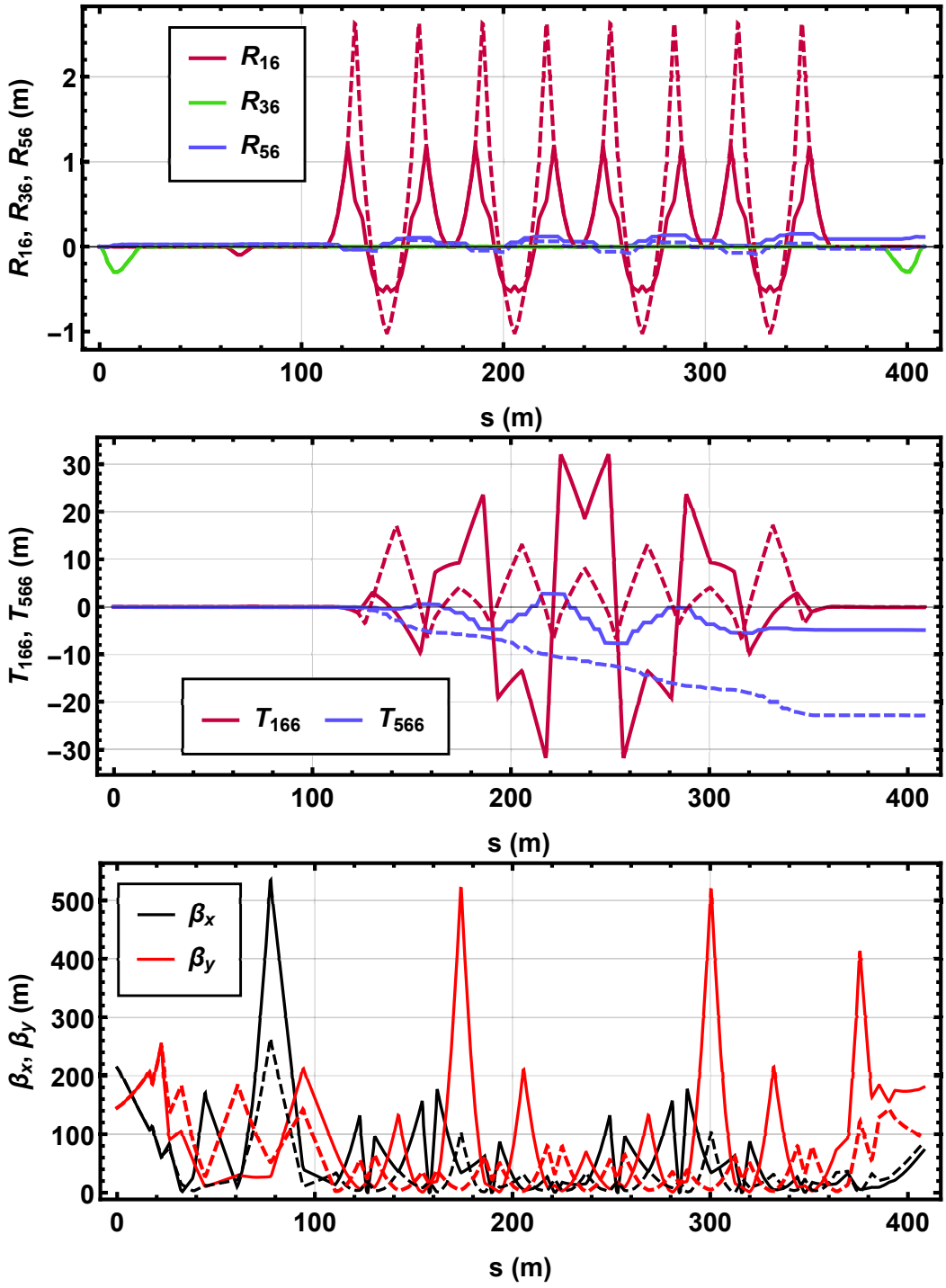

Figure 5.9: Initial (dashed) and reduced dispersion configuration (solid), first and second-order dispersions and optics (top, middle and bottom respectively) of CEBAF's Arc 9.

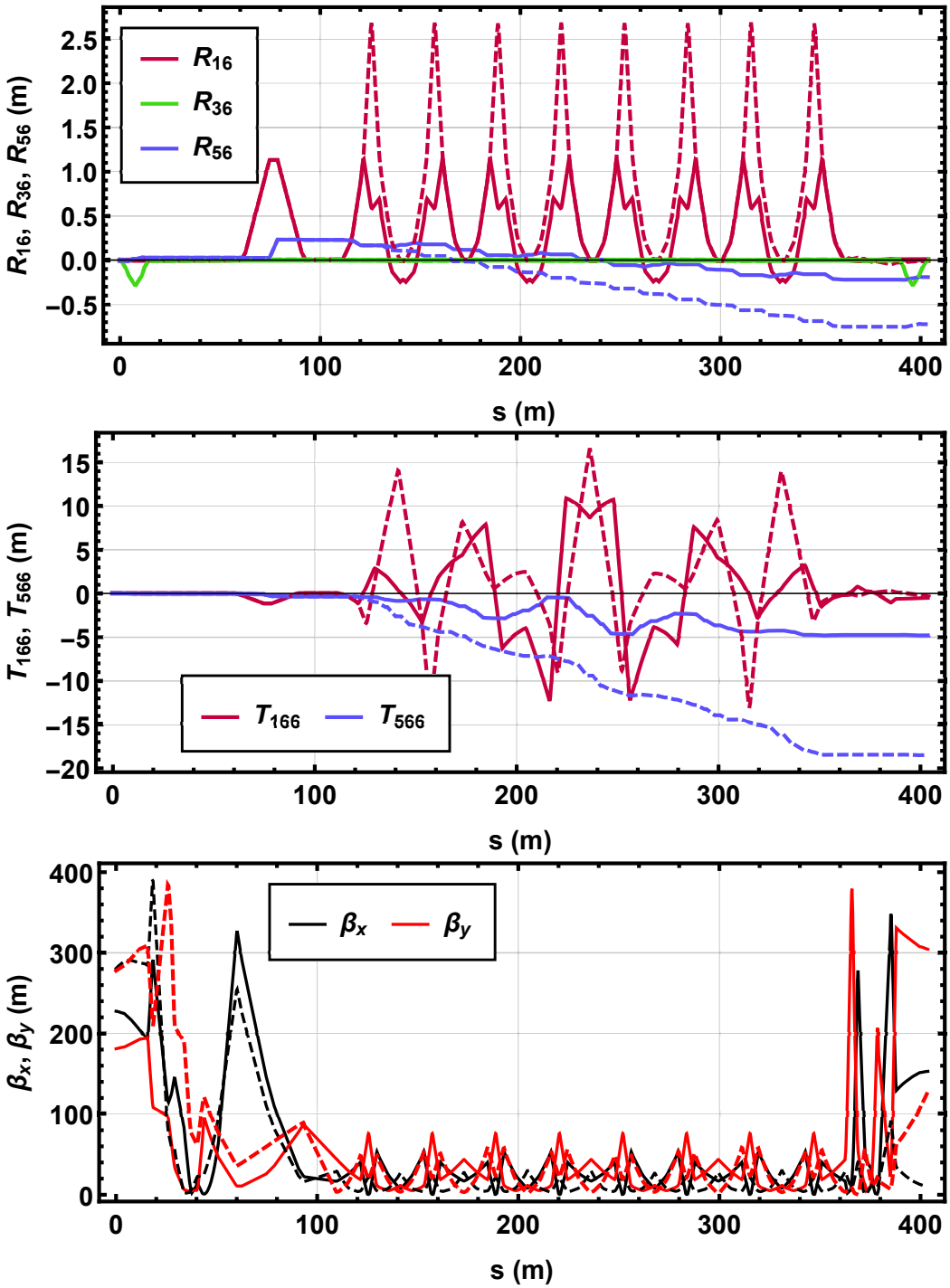

Figure 5.10: Initial (dashed) and reduced dispersion configuration (solid), first and second-order dispersions and optics (top, middle and bottom respectively) of CEBAF's Arc 10.

5.2.4 Longitudinal match

The X-FEL longitudinal match that we want to replicate revolves around a bunch compression at top energy to achieve the maximum current possible to drive our fictitious X-FEL at the exit of Arc 10. In order to preserve beam quality during transport from the injector to the interaction point, the bunch length must be kept long to minimize the impact of collective effects. During deceleration, the bunch undergoes an anti-damping process. Therefore, the bunch must be decompressed and chirp compensated to remain within the arcs' apertures. Following the semi-analytic method portrayed in chapter 4 we formulate a series of possible longitudinal matches of the same kind as Fig.4.15.

Table 5.5: Alternative longitudinal match solutions employing different arcs.

Top arc R_{56} (m)	Decompressing arc R_{56} (m)	Accelerating rf phase ($0^\circ = \text{on crest}$)
-0.30	0.23 (arc 5)	8°
-0.38	0.22 (arc 8)	8°
-0.42	0.22 (arc 9)	8°
-0.29	0.17 (arc 9)	12°
-0.19	0.11 (arc 9)	18°

In the matches where the decompressing arc is a lower energy arc, the fully compressed decelerating beam has its energy spread grow adiabatically over a greater number of rf passes. However, after decompression, the beam has a fewer number of passes in which to compensate its chirp to stay within the arc energy acceptance. Therefore, solely changing which is the decompressing arc has a minimal effect on the R_{56} requirements of this arc to complete the point-to-parallel match. Because of this reason, we favour matches where the decompressing arc follows immediately after the compression, and choose arc 9 to do so. Finally changing the chosen accelerating rf phase reduces the R_{56} requirements of both compressing and decompressing arcs while limiting the initial bunch length that can be transported while maintaining the beam within the energy acceptance of the machine.

From the series of matches outlined in table 5.5 we proceed to evaluate the final option. This results in a compressed longitudinal phase space after arc 10 as shown in Fig. 5.11.

The prediction from the 1-d model, without energy spread, matches the longitudinal phase space obtained via tracking with Elegant. Further optimization of the peak current can be done by tuning the T_{566} of arc 10.

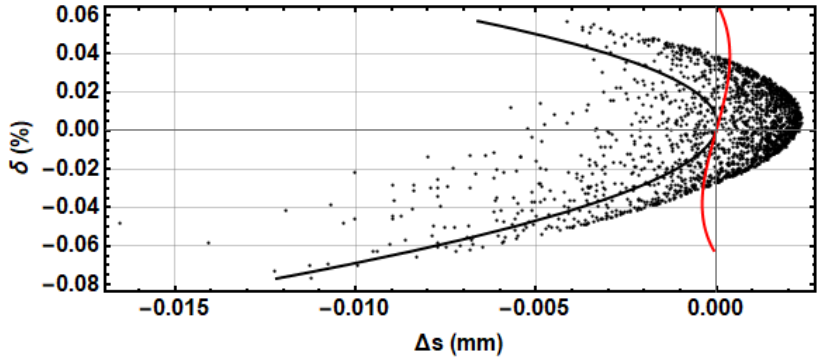

Figure 5.11: Tracked bunch longitudinal phase space, prediction of the tracked bunch from semianalytical model (black line) and semianalytical prediction after preliminary second order corrections (red line).

5.3 Experimental considerations

The standard bunch charge available at CEBAF of 0.2 pC is not high enough to emulate that of a dedicated FEL source like for example the European XFEL ranging from 20 pC to 1 nC [73]. A higher bunch charge in general means a longer bunch from the cathode. This longer bunch can be emulated by setting a phase shifter between the master oscillator and the rf cavities; the timing between the signals driving the injector and the rf cavities becomes desynchronized. Now bunches will see different phases because the rf is ahead/behind-time. If we instead consider that the rf is always "on time" and the bunch is the one that was too early or too late we can explore how a longer bunch would behave by looking at the smaller bunches that effectively populate all the regions of the fictional long bunch. A visual representation of this phase space painting is shown in Fig. 5.12. It must be noted however, this approximation of the behaviour of a longer bunch cannot take into account the effects driven by a higher bunch charge density. For example, at low energy, longitudinal space charge will be important, and, at high energy, CSR will be

important.

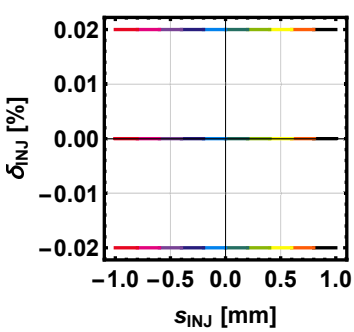

(a) Initial longitudinal phase space.

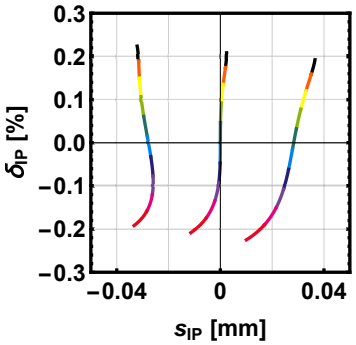

(b) Compressed longitudinal phase space at IP.

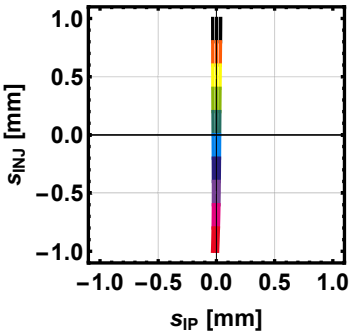

(c) R_{55} mapping.

Figure 5.12: Example use of multiple short bunches to emulate a longer bunch.

Dispersion leaks from one arc to the next arc get adiabatically damped during acceleration, but they can re-emerge during deceleration if not adequately cancelled. An example of this dispersion behaviour is shown in Fig. 5.13. In the horizontal plane, the new configuration shows less dispersion leaking from arc to arc. In the vertical plane though, the dispersion leaks similarly in both cases during deceleration.

Arc dipoles share a common power supply. If the beam energy is high enough, energy lost to synchrotron radiation will induce an orbit error due to the energy difference in the downstream dipoles within the same arc. This energy loss in arc 10 is shown in Fig. 5.14. A series of kickers can be used for orbit corrections. Moreover, a series of synchrotron radiation compensating coils are present in the dipoles to further tune the dipole power. In order to study the results of this effect, we also include the expected next-to-leading-order source of centroid deviation, random quadrupole misalignments, with an amplitude of 200 µm. The results of this study are shown in Fig. 5.15 for arc 10, and in Fig. 5.16. For arc 10, without compensating coils and without correction from the kickers results in centroid deviations of several mm, and the correction from the kickers cannot fully compensate for this effect. With the synchrotron radiation coils, the peak orbit deviations are smaller than in the previous case, and with the additional correction from the kickers, the peak deviations are around 0.05 mm as shown in Fig. 5.15. On the other hand for arc 9, there is minimal difference between the results of the simulations with and without

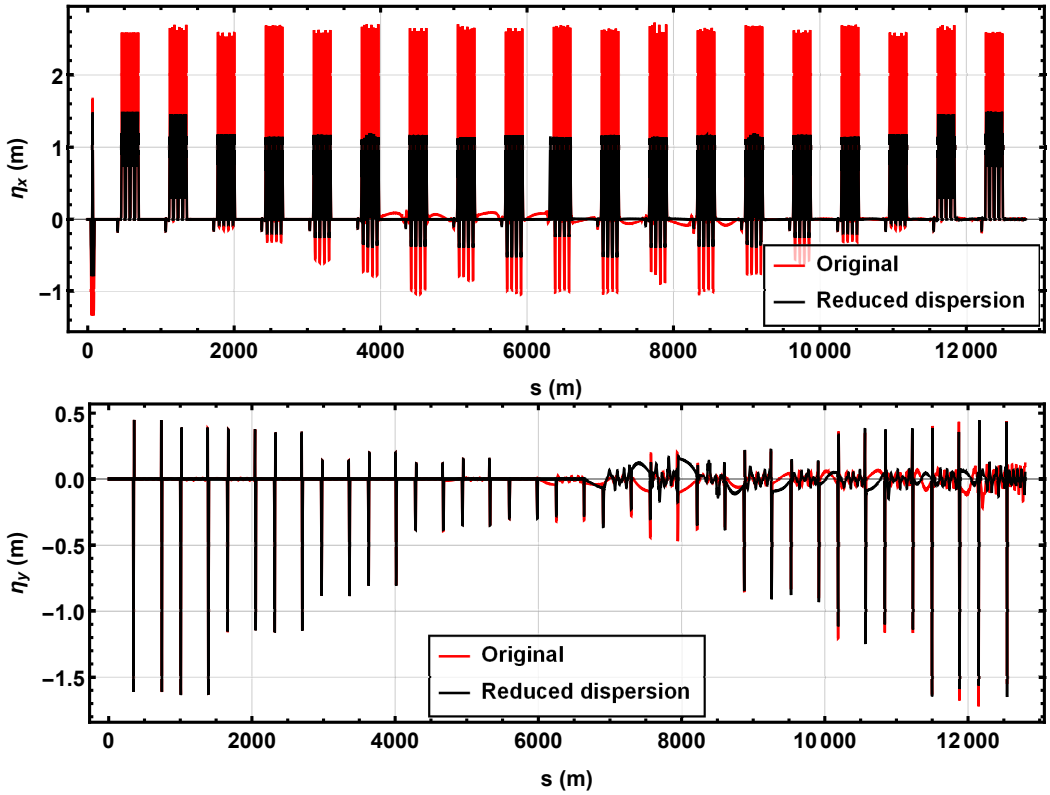

Figure 5.13: Start to end comparison of horizontal dispersion η_x (top) and vertical dispersion η_y (bottom) between original and reduced dispersion configurations.

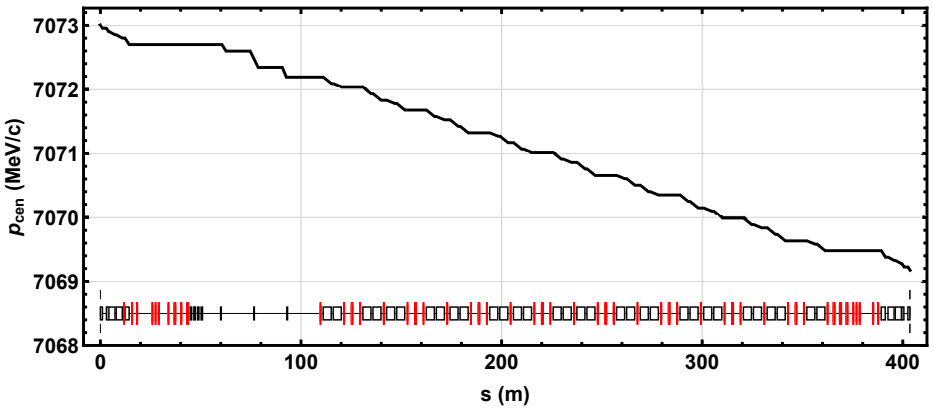

Figure 5.14: Mean beam momentum as it traverses the top energy arc. Energy lost corresponds to SR. Overlayed magnet lattice with dipoles as boxes and quadrupoles in red.

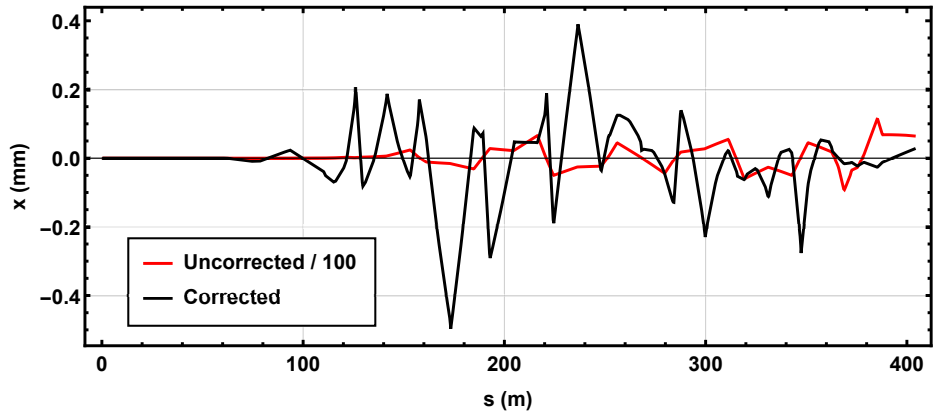

(a) Without compensating coils.

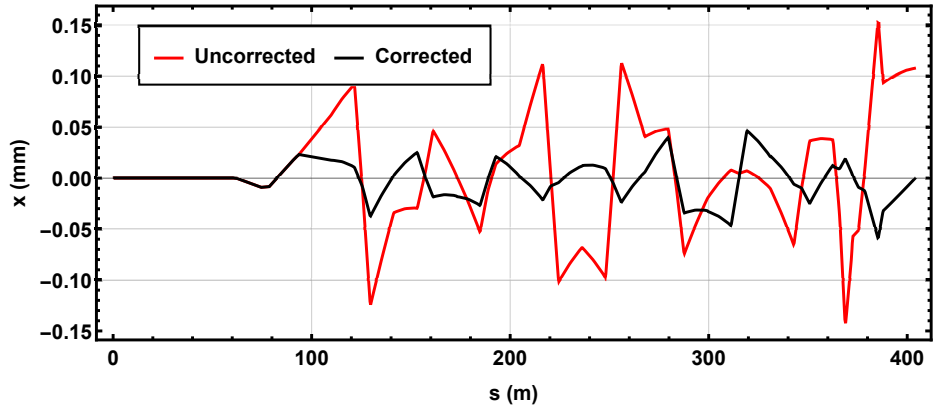

(b) With compensating coils.

Figure 5.15: Arc 10 horizontal centroid deviation due to dipole common power supply, energy lost to SR and random quadrupole misalignments with amplitude of 200 µm.

the synchrotron radiation compensating coils in the cases where the kickers are used as shown in Fig. 5.16. Therefore we can conclude that the induced centroid deviations due to energy lost within the arc are dominated by plausible quadrupole offsets in arcs 9 and below.

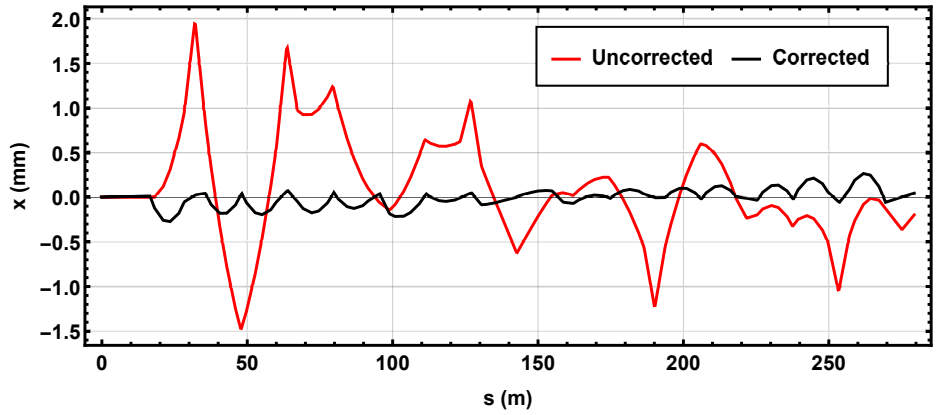

(a) Without compensating coils.

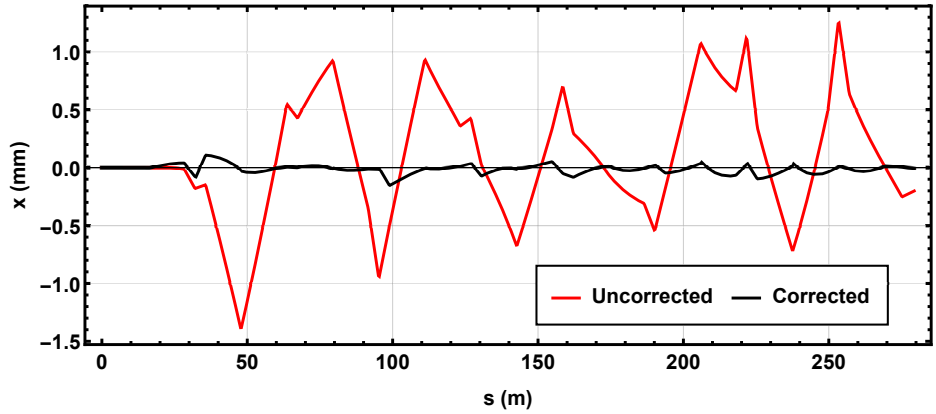

(b) With compensating coils.

Figure 5.16: Arc 9 horizontal centroid deviation due to dipole common power supply, energy lost to SR and random quadrupole misalignments with amplitude of 200 µm.

5.4 Conclusion

We have shown the operational constraints for an ERL to be a suitable machine to drive an XFEL, as well as the series of modifications we propose to the CEBAF lattice that would provide the right longitudinal match. To first order, this requires a modification of the arcs

to increase their momentum acceptance, adequate choice of rf phase and arc path length to be able to manage energy lost to ISR, and finally, modifications to arcs 9 and 10 to compress and decompress the electron bunch. In order to further improve our longitudinal match, second-order corrections to eliminate the curvature from the compressed bunch while not compromising our capabilities to transport the bunch in the decelerating passes would be required. We have also considered some of the experimental considerations that must be taken into account such as the emulation of a longer bunch, dispersion leakage between arcs and synchrotron radiation induced orbit deviations.

Chapter 6

Longitudinal beam dynamics at PERLE

6.1 Longitudinal match

The ability of PERLE [16] to explore its planned experimental programme can be enhanced by optimizing the lattice to produce a longitudinal phase space at the interaction point such that the bunch energy spread is minimized. This corresponds to the case from section 4.6 of energy spread minimization in a common transport topology without significant SR energy losses.

Following the limitations of the PERLE design as a common transport ERL, the available parameters when constructing a longitudinal match are: each of the arcs' longitudinal dispersions, their pathlengths, and the initial phases of both linac sections. The initial longitudinal dispersions of each of the arcs are shown in table 6.1.

Table 6.1: First-, second- and third-order longitudinal dispersions of each of the PERLE arcs. Arc 6 is split into spreader, arc and recombiner sections as interaction regions are placed between these.

	R_{56} (m)	T_{566} (m)	U_{5666} (m)
Arc 1	0.0	-5.3	35.3
Arc 2	0.0	-5.3	35.3
Arc 3	0.0	-4.5	51.9
Arc 4	0.0	-4.6	-20.3
Arc 5	0.0	-4.3	14.5
Arc 6 spreader	0.05	-0.07	0.05
Arc 6	-0.1	-4.0	12.6
Arc 6 recombiner	0.05	-0.07	0.05

6.1.1 On-crest match

To first order, the desired longitudinal match can be obtained by keeping all arcs isochronous with path lengths being an integer multiple of rf wavelengths, and initial rf phases on-crest. Setting the injected bunch to have a flat longitudinal phase space, this configuration results in a longitudinal phase space at the interaction regions as shown in Fig. 6.1 where the final energy spread is dominated by the effect of the rf curvature imprinted on the bunch.

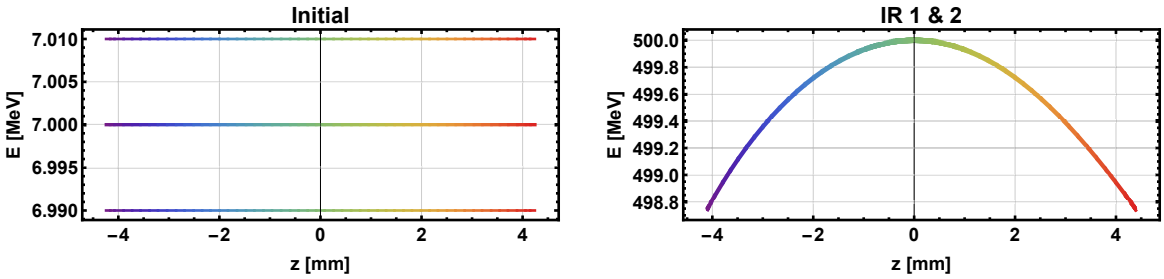

(a) (b)

Figure 6.1: Longitudinal phase spaces of (a) assumed initial bunch and (b) bunch at the interaction regions showing the curvature acquired during acceleration.

For this configuration to result in a minimized energy spread at the interaction region, the necessary longitudinal phase space of the injected bunch, as shown in Fig. 6.2, is the opposite of the previously shown interaction region longitudinal phase space. Additionally,

as the bunch reaches the dump, this energy spread is replicated with the added distortion from the arc longitudinal dispersions.

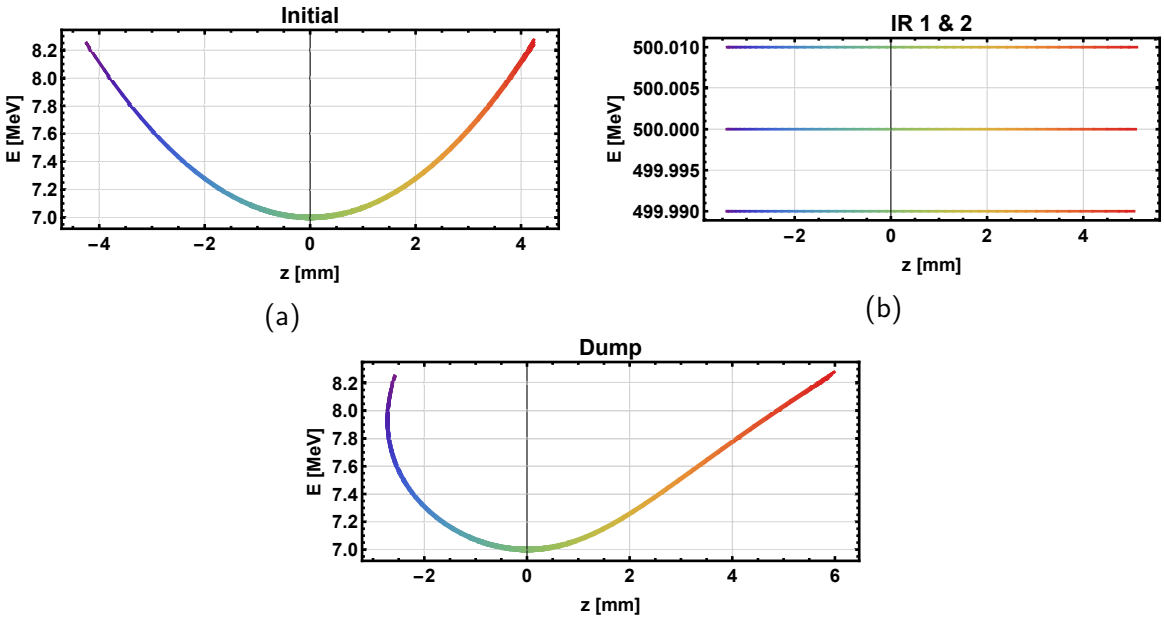

(a) (b) (c)

Figure 6.2: Longitudinal phase space necessary at the injector (a) to compensate for rf curvature at the interaction regions (b), and final longitudinal phase space after deceleration at the dump in an on-crest longitudinal match.

Although this works in principle, it requires an extremely challenging longitudinal phase space to obtain out of the injector, and therefore we must consider off-crest longitudinal matches to minimize the bunch energy spread at the interaction regions.

6.1.2 Energy spread minimization

For linacs 1 and 2 the first accelerating rf phases are $\theta_{1,1}$ and $\theta_{2,1}$ respectively and the arc 1 through 6 phase shifts corresponding to the path length deviations from an integer number of rf wavelengths are denoted as $\Delta\theta_i$ with i indicating the corresponding arc. Successive rf phases correspond to the previous phase plus the offset obtained by the following two arcs. In this way, for example, $\theta_{1,2} = \theta_{1,1} + \Delta\theta_1 + \Delta\theta_2$ and $\theta_{2,2} = \theta_{2,1} + \Delta\theta_2 + \Delta\theta_3$.

Following the solutions from section 4.6, we choose a rf phase configuration shown in

Fig. 6.3 which can be obtained by setting arc path lengths as shown in Fig. 6.4.

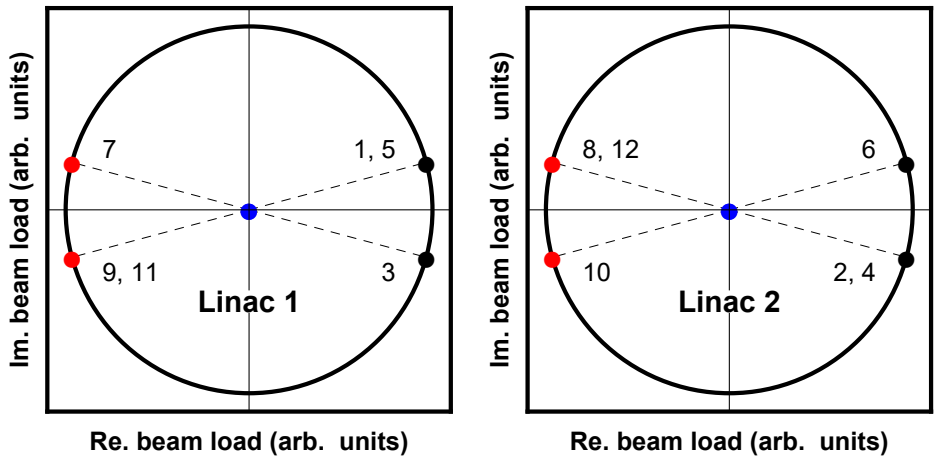

Figure 6.3: rf beam load diagram of linacs 1 and 2 with phase choices during acceleration (black), deceleration (red), and resultant rf load (blue).

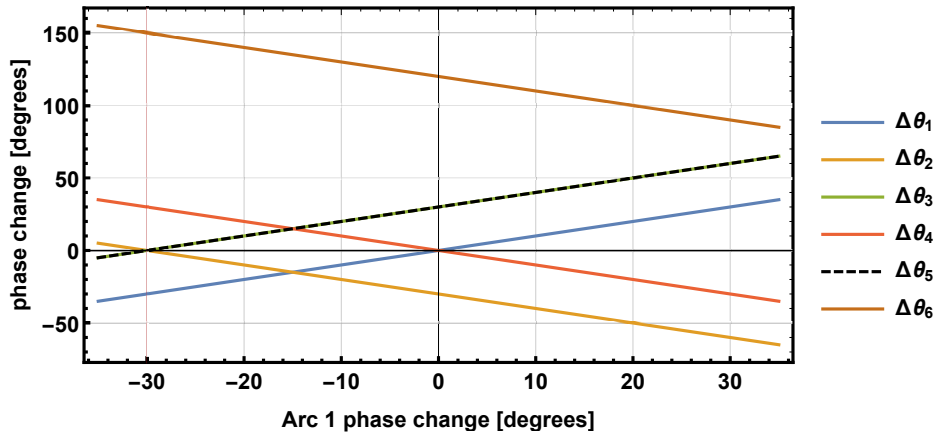

Figure 6.4: Deviation from integer number of wavelengths of arc path lengths as a function of the deviation of arc 1 to achieve the phase scheme of Fig. 6.3.

With this set of phases, during acceleration, the beam traversing through arc 1 has a chirp of opposite sign to when it reaches arc 4. During deceleration, these signs change. In this manner, the lengthening and shortening of the bunch tails as the bunch is linearized will compensate resulting in a bunch with a controlled bunch length.

Due to the symmetry of the system, a set of T_{566} values for the arcs that linearizes the bunch at the top energy also returns the bunch to its initial curvature as it reaches the dump. Therefore, the objective of linearizing the bunch towards the IR tuning two arcs is an underconstrained problem. A study of of the possible configurations is shown in Fig. 6.5,

where by setting one of the arcs T_{566} values and solving for the other, the longitudinal phase spaces at the IR and dump are compared for the effectiveness of the bunch length control scheme. Additionally, the change between the initial and final T_{566} value of the arcs must also be taken into account as greater changes will require stronger corrections with the corresponding stronger sextupole fields.

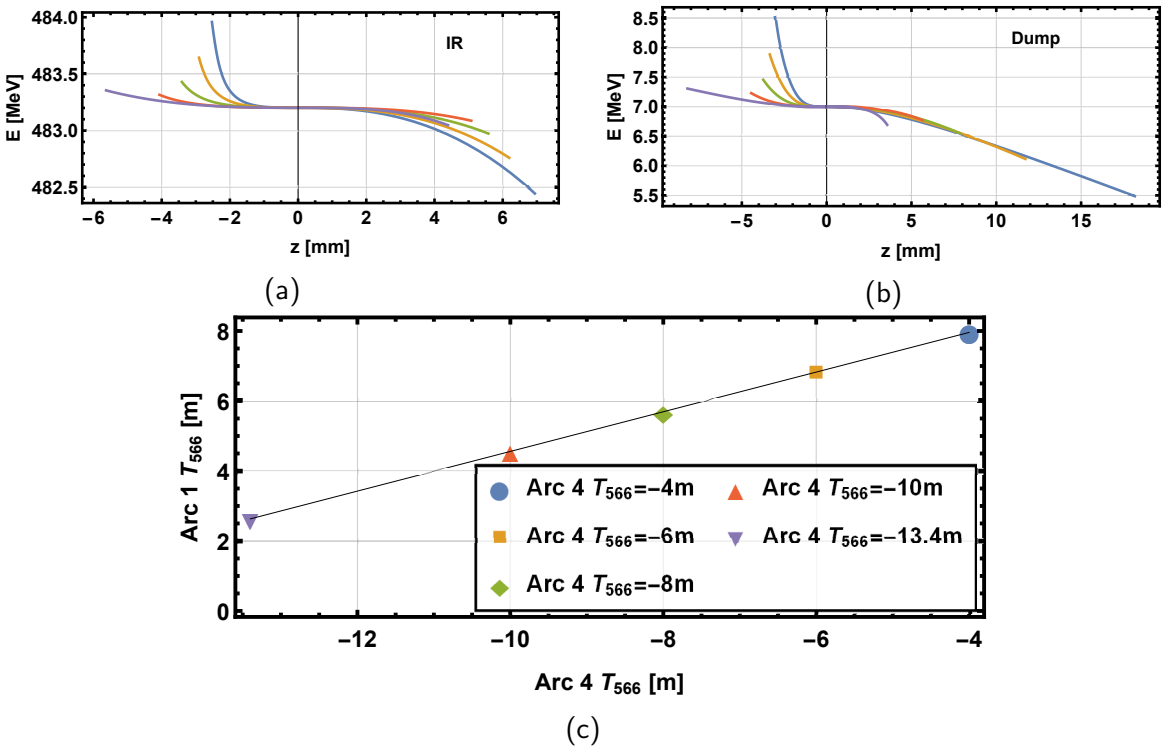

Figure 6.5: Longitudinal phase spaces at (a) the interaction region and (b) dump for (c) different combinations of linearizing T_{566} in arcs 1 and 4, with line indicating a continuous set of solutions available.

Alternatively, a modest compression of the bunch in the first arc by deviating from the isochronous condition would reduce the degrees of rf that the bunch sees for the rest of the accelerating passes and hence reduce the curvature to be corrected tuning the arc T_{566} values. To compensate for the change in the bunch chirp during the compression, the rf phases must shift accordingly. This can be treated as a perturbation from our previous solution for small compressions where the magnitude of the off-crest angle of the first accelerating pass is decreased. The corresponding change in path lengths also affects the phase of the last decelerating pass going equally closer to on-trough as the first pass. This strategy is limited by the range of R_{56} values available. An example set of phases is

shown in Fig. 6.6. Again, the symmetry of the system is such that during deceleration, the compressed bunch reaches arc 1 with the opposite sign of chirp and is decompressed such that during the last deceleration towards the dump the beam chirp is cancelled as shown in Fig. 6.7. The only modified arc parameters are for arc 1: $R_{56} = 0.05\,\mathrm{m}$, $T_{566} = 6.49\,\mathrm{m}$ and for arc 4: $T_{566} = -10\,\mathrm{m}$.

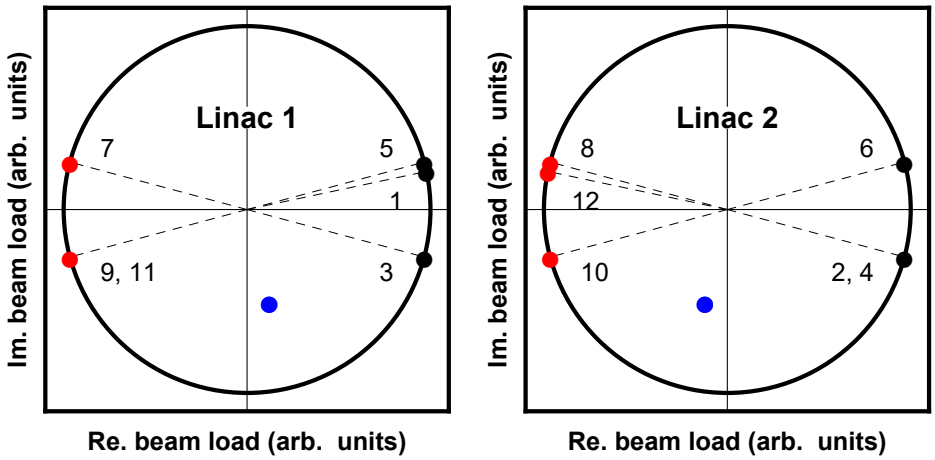

Figure 6.6: rf beam load plots for linacs 1 and 2 for a longitudinal match with a non-isochronous arc 1 showing phase choices during acceleration (black), deceleration (red), and 10x resultant (blue).

The remaining energy spread in the IR corresponds to the third-order curvature that is present in the model, but has not been corrected.

6.1.3 Injected bunch

A more realistic example bunch is depicted in Fig. 6.8 provided by Ben Hounsell [74] which corresponds to a tracked bunch from the cathode to the exit of the first linac. In this way, the relativistic effects and longitudinal space charge relevant at low energies are still taken into account. We can fit this longitudinal phase space to extract the necessary parameters to include in our model.

The third order polinomial that results as a best fit to this longitudinal phase space to

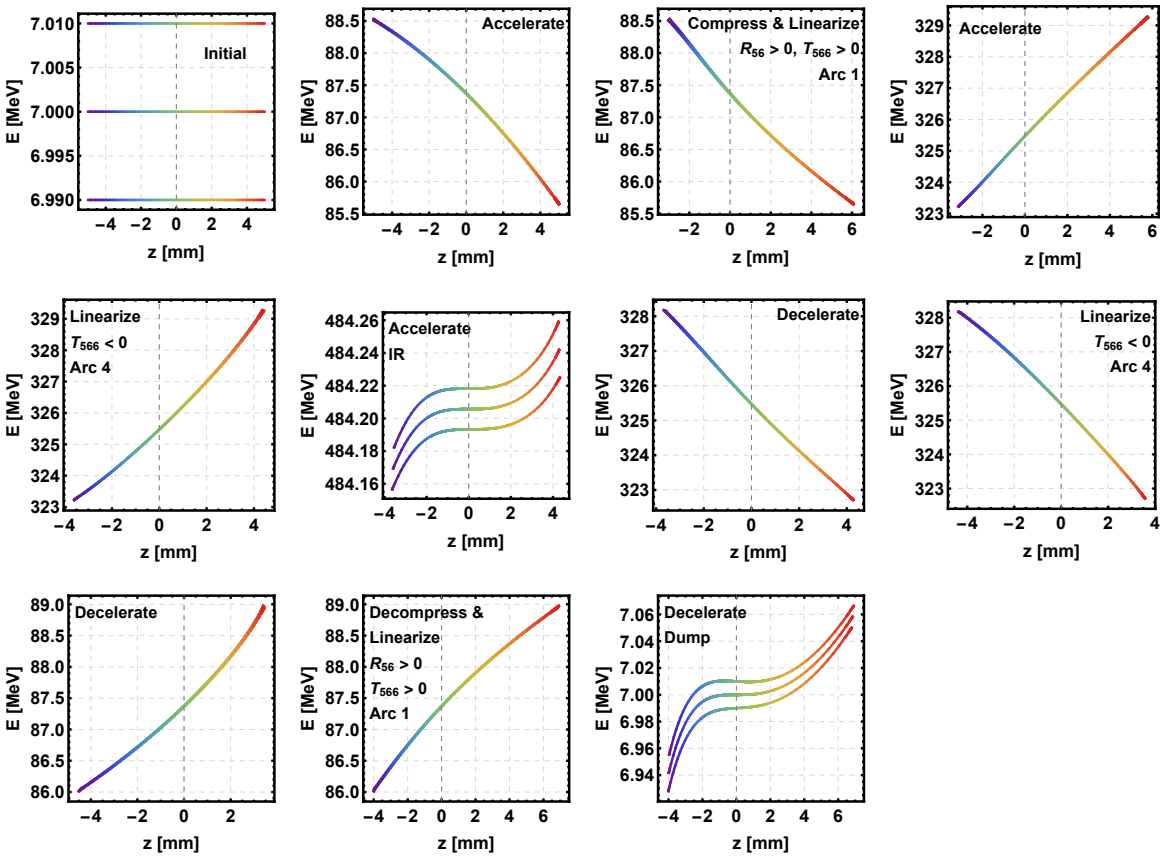

Figure 6.7: Sequence of longitudinal phase spaces of a longitudinal match with a slight compression in Arc 1.

enable comparison with our semi-analytic method is

$$E(z) = 86.4781 - 352.444z - 10239.3z^2 + 24032.0z^3\,, \tag{6.1}$$

whereas our initial estimate from our semi-analytic method following the match of Fig. 6.5 is

$$E(z) = 86.3669 - 357.271z - 11200.1z^2 + 16805.8z^3\,. \tag{6.2}$$

This tracked bunch presents higher-order nonlinearities that are not captured by our method. If third-, fourth- or higher-order corrections were considered for the lattice, the model can easily be expanded to the required order. However, collective effects which are not included in our model will have effects of comparable magnitude to these higher-order nonlinearities. Therefore, at that stage of optimization, a combined study with tracking

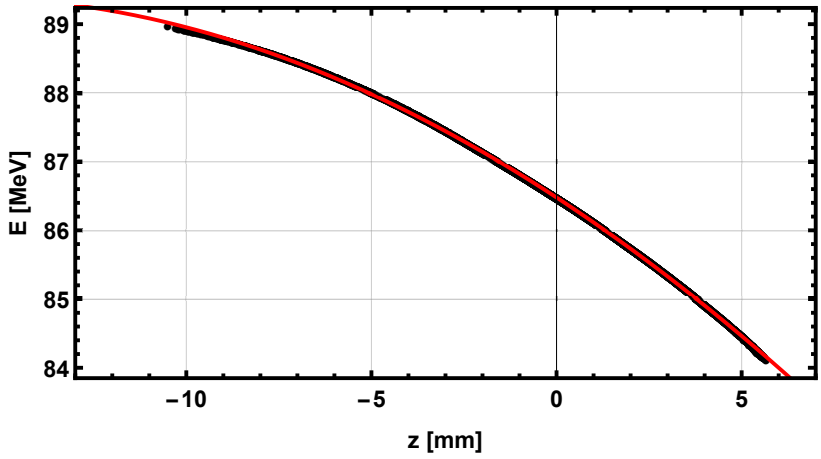

(a)

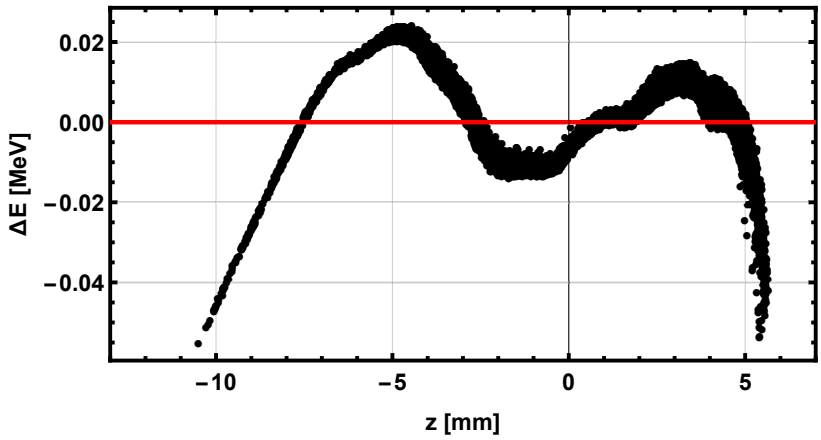

(b)

Figure 6.8: Longitudinal phase space of tracked bunch at (a) the exit of the first linac accelerated 15 deg off-crest, with red line representing a third-order polynomial fit and (b) deviations from fit line.

capabilities is necessary.

6.2 Conclusion

In this chapter, we have explored the design of PERLE as a specific example of an energy spread minimizing longitudinal match in a common transport ERL without synchrotron radiation. The starting longitudinal match in section 6.1.1 shows the limitations of an on-crest match for such a purpose highlighting the relationship between injected bunch charge and bunch length at the injector.

On the other hand, we explore in section 6.1.2 the options available when considering off-crest matches, greatly improving the achieved energy spread at the interaction regions by building on the knowledge from chapter 4. Three main points are drawn from this section: 1) The availability of suitable linac phase configurations relies on the flexibility of the arcs to provide the necessary path length adjustments. 2) Once an off-crest match is achieved, a balance in the linearizing efforts of the selected arcs by tuning of their longitudinal dispersions has strong repercussions on the viability of the matches by keeping the bunch tails under control. 3) A sample match including a modest bunch compression in arc 1 is showcased bringing further improvements with regards to energy spread at the interaction regions with the drawback of a small but non-zero rf beam load at the linacs. Further studies of this trade-off would present a final clear choice for the preferred longitudinal match for PERLE and other ERL projects of similar characteristics.

Chapter 7

Conclusions

In this thesis, we considered the longitudinal beam dynamics in electron accelerators with a particular interest in energy recovery linacs and their longitudinal matches. The initial study of the MAX-IV bunch compressors sets up the framework of designing a lattice to achieve the required longitudinal dispersions. Additionally, the proposed method of using variable trajectories for different settings has the side effect of also changing the path length of the system making this type of variable bunch compressor significant for ERLs.

From the design of an individual transfer line with tailored longitudinal properties, we shift towards a more general view by considering the longitudinal match of an accelerator injector to dump. This method builds on the previous work of Zagorodnov and Dohlus to derive a model of multi-turn ERLs with rf curvature compensation to achieve either fully-compressed bunches at the interaction region or minimized energy spread. These are useful for future FEL or collider applications respectively. In addition to the difference in the required longitudinal phase spaces for the desired application, we consider other sub-classifications: the comparison of separate and common beam transport, and facilities with or without synchrotron radiation considerations, depending on their energies. This wide study aims to facilitate the initial conceptual design of any future ERL by providing a top-level comparison of the capabilities of the different design choices and finally match the project scope to a reduced set of candidates moving forward in the design process. Within

the individual examples, the presented discussion on how to optimize the longitudinal matches provides essential insight into the planning of any ERL without the need for a lattice, therefore also expediting the initial design process.

In summary, all separate transport configurations were found to provide enhanced flexibility as a result of the increased number of degrees of freedom available. In all cases, these separate transport designs were capable of generating a satisfactory longitudinal match able to satisfy constraints at the interaction region, dump and during transport simultaneously. In the case of common transport configurations, longitudinal matches that do not require compensation of SR energy losses are not negatively affected by the reduction of degrees of freedom in our design, albeit that they are less flexible in general. In essence, this is due to the symmetry in the lattice being able to correspond to the symmetry in the longitudinal match. However, if significant disruption of the beam is expected for example by driving an FEL, or the energy lost to SR becomes significant, the parity between lattice symmetry and longitudinal match asymmetry breaks, and special care must be taken to keep the beam within acceptable parameters reducing the expected performance up to the point where the miss-match is so great that additional countermeasures are required. Such measures could involve either inclusion of additional rf infrastructure or transition to separate transport to cope with the energy losses and energy spread increases. This method of finding longitudinal matches is showcased in specific significant projects with contemporary relevance: ER@CEBAF and PERLE.

The proposed longitudinal match at ER@CEBAF would be the necessary one to drive an FEL. Such a match requires a re-tune of the CEBAF arcs to increase their momentum acceptance to allow off-crest acceleration of the beam, as well as a change of the longitudinal dispersion in selected arcs away from their current isochronous design parameters. Additional experimental considerations are taken into account such as the SR energy loss within individual arcs and the resulting orbit deviations and dispersion leaking between arcs.

The construction of the longitudinal match for PERLE is constrained by the high bunch

charge necessary to match the LHeC parameters. As a result, the injected bunch length is high compared to our previous example and special care must be taken to keep the bunch tails under control. An on-crest match is penalized by the energy spread introduced in the long bunch by the rf curvature and, without going off-crest. Correcting this effect would require an expensive linearizing harmonic rf system. The alternative off-crest match relies on the change of arc path lengths to enable the right choice of phases during acceleration and deceleration. The bunch linearization presents another optimization opportunity between the strength of the correction required and the control of the bunch tails. Finally, we present a longitudinal match with a modest compression in the first arc to ease the linearization efforts required as well as a way to use our method with input bunch parameters from tracking simulations at low energy.

The techniques presented in this thesis can become the basis of fundamental tools for the design of future ERLs.

Appendix A

ER@CEBAF arc optics

Bellow are shown the initial and reduced dispersion configurations of the ER@CEBAF arcs that have been omitted from the body of the thesis.

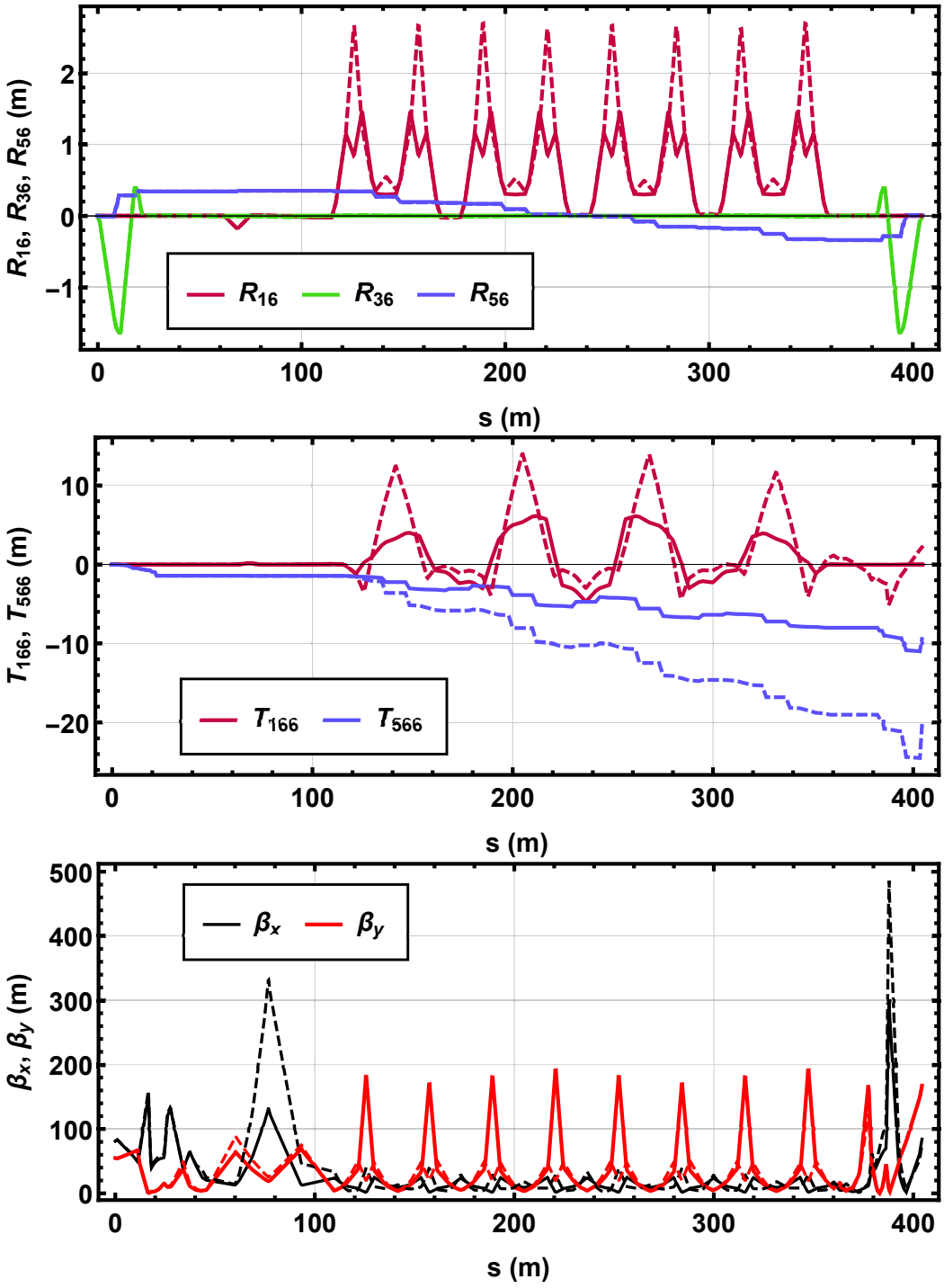

Figure A.1: Initial (dashed) and reduced dispersion configuration (solid), first and second-order dispersions and optics (top, middle and bottom respectively) of CEBAF's Arc 2.

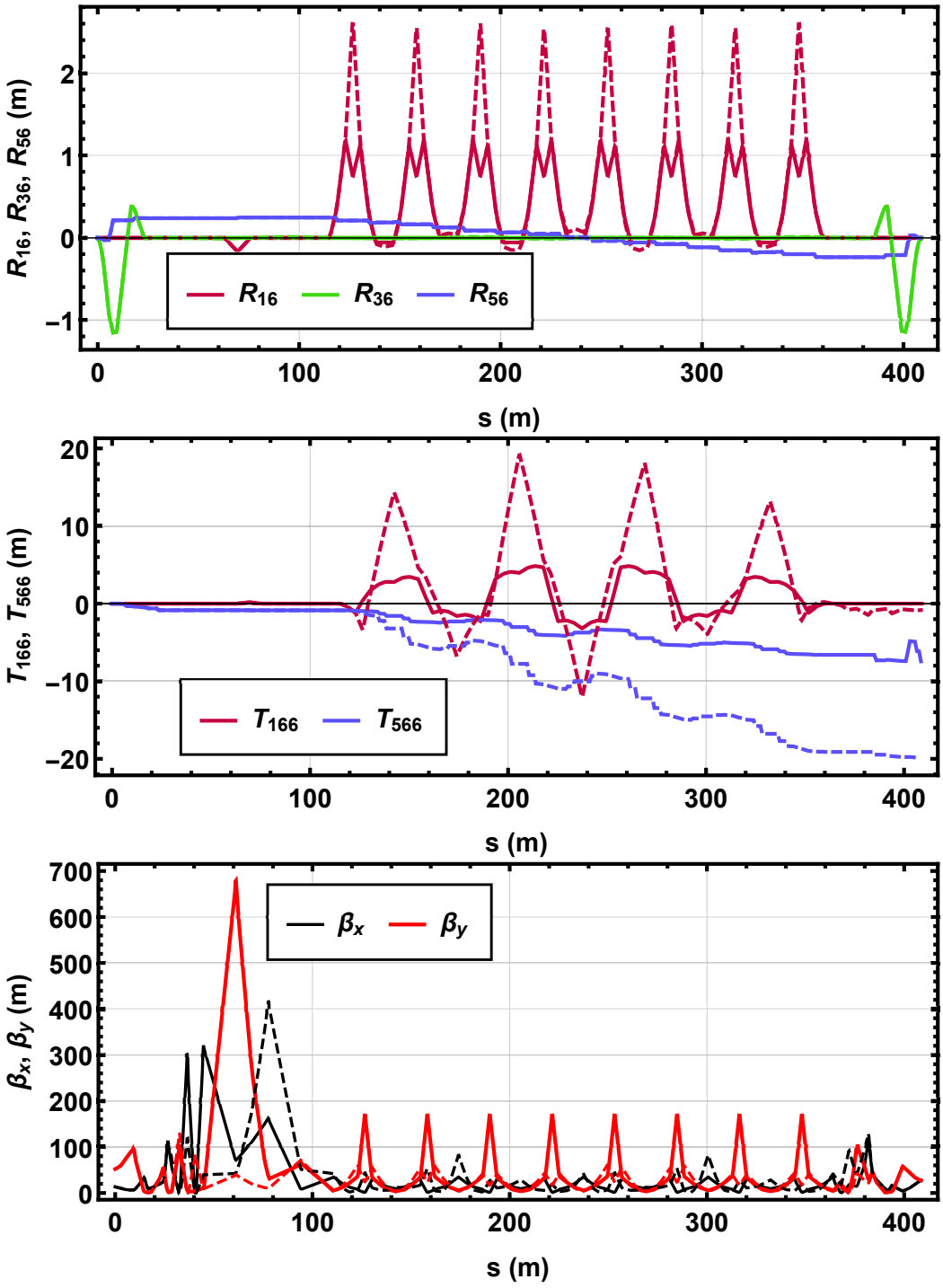

Figure A.2: Initial (dashed) and reduced dispersion configuration (solid), first and second-order dispersions and optics (top, middle and bottom respectively) of CEBAF's Arc 3.

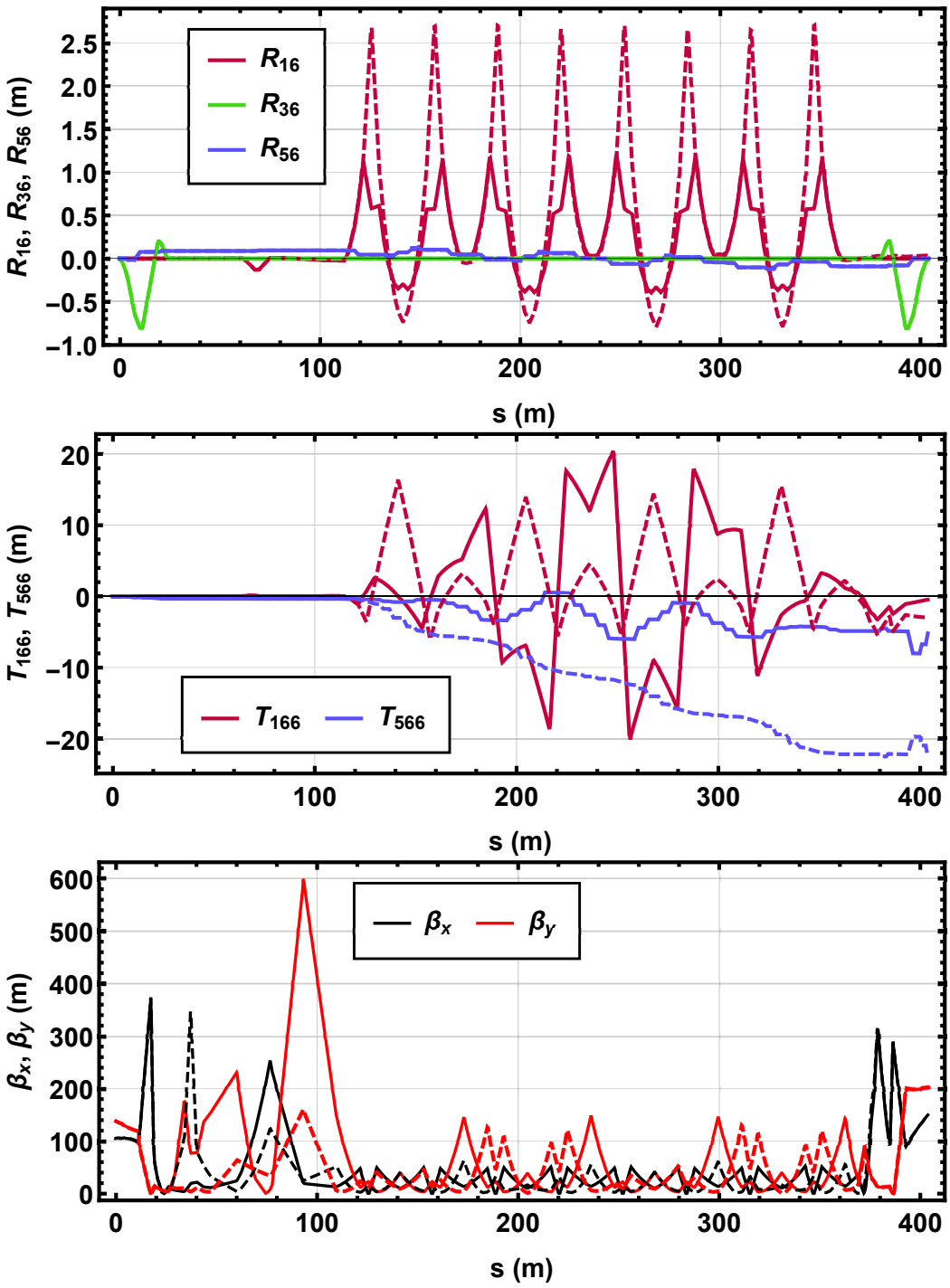

Figure A.3: Initial (dashed) and reduced dispersion configuration (solid), first and second-order dispersions and optics (top, middle and bottom respectively) of CEBAF's Arc 6.

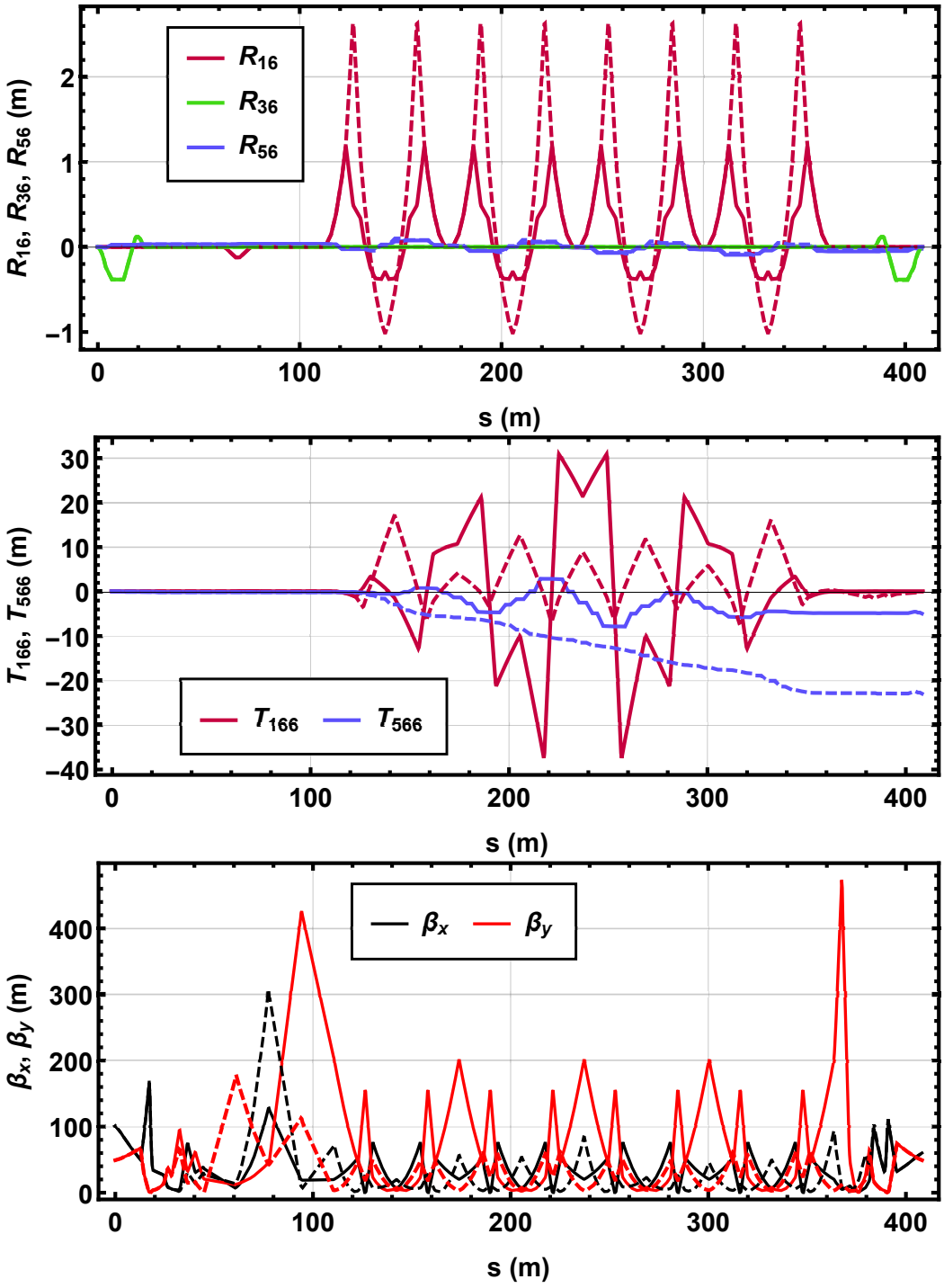

Figure A.4: Initial (dashed) and reduced dispersion configuration (solid), first and second-order dispersions and optics (top, middle and bottom respectively) of CEBAF's Arc 7.

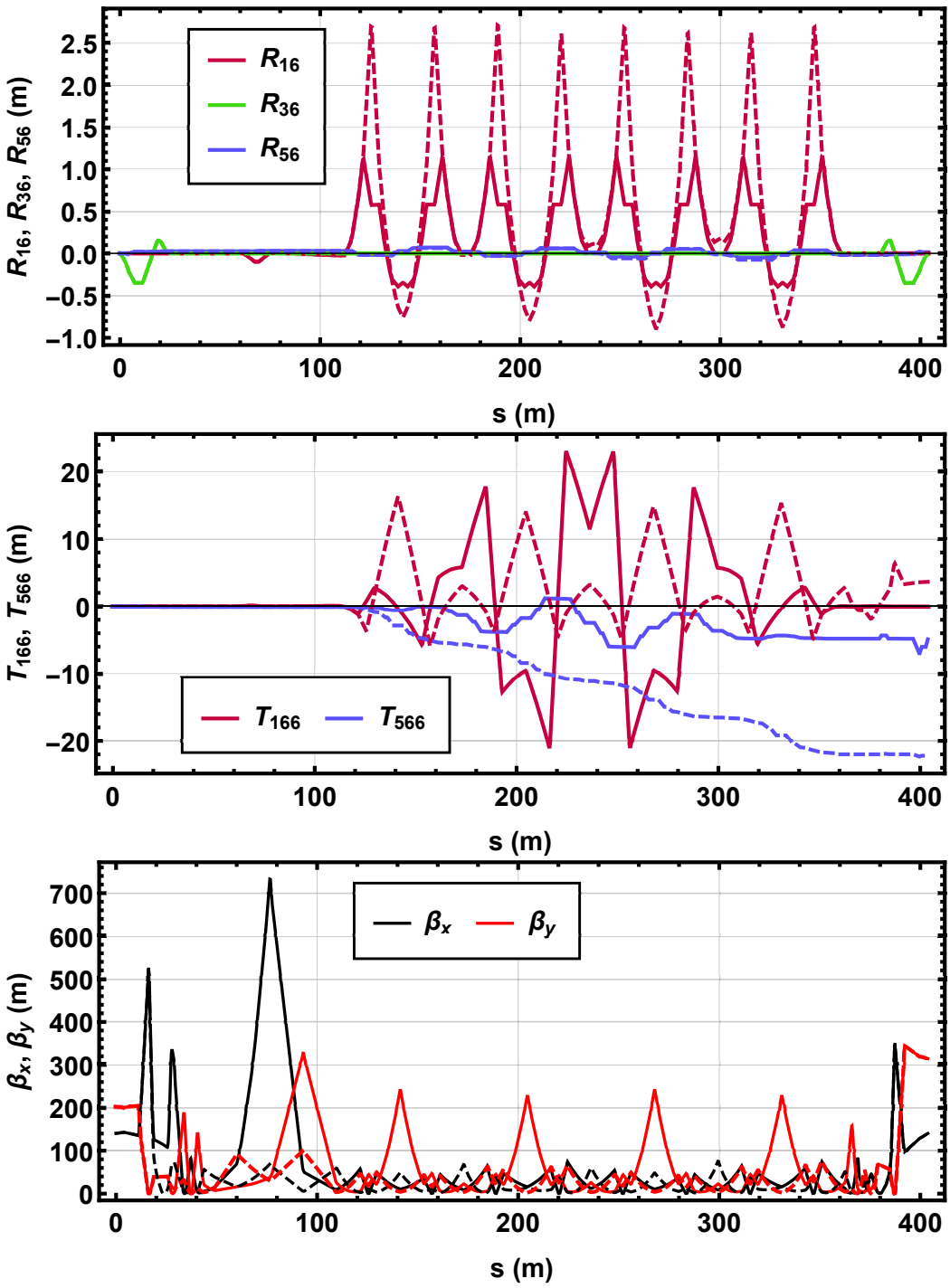

Figure A.5: Initial (dashed) and reduced dispersion configuration (solid), first and second-order dispersions and optics (top, middle and bottom respectively) of CEBAF's Arc 8.

Bibliography

[1] Christoph W. Leemann, David R. Douglas, and Geoffrey A. Krafft. "THE CONTINUOUS ELECTRON BEAM ACCELERATOR FACILITY: CEBAF at the Jefferson Laboratory". In: **Annual Review of Nuclear and Particle Science** 51.1 (Dec. 2001), pp. 413–450. ISSN: 0163-8998. DOI: 10.1146/annurev.nucl.51.101701.132327. URL: https://www.annualreviews.org/doi/10.1146/annurev.nucl.51.101701.132327.

[2] M. Tigner. "A possible apparatus for electron clashing-beam experiments". In: **Il Nuovo Cimento Series 10** 37.3 (1965), pp. 1228–1231. ISSN: 00296341. DOI: 10.1007/BF02773204.

[3] M. Klein et al. "Energy Recovery Linacs". In: **European Strategy for Particle Physics - Accelerator R&D Roadmap**. Ed. by N. Mounet. CERN, 2022, p. 187.

[4] F. Jackson et al. "Longitudinal transport measurements in an energy recovery accelerator with triple bend achromat arcs". In: **Physical Review Accelerators and Beams** 19.12 (Dec. 2016), p. 120701. ISSN: 2469-9888. DOI: 10.1103/PhysRevAccelBeams.19.120701. URL: https://link.aps.org/doi/10.1103/PhysRevAccelBeams.19.120701.

[5] C Tennant et al. "CEBAF-ER: Extending the Frontier of Energy Recovery At Jefferson Lab". In: 2003, pp. 249–253. URL: https://accelconf.web.cern.ch/SRF2003/papers/tuo08.pdf.

[6] P. Piot, D. R. Douglas, and G. A. Krafft. "Longitudinal phase space manipulation in energy recovering linac-driven free-electron lasers". In: **Physical Review Special**

Topics - Accelerators and Beams 6.3 (Mar. 2003), p. 030702. ISSN: 1098-4402. DOI: 10.1103/PhysRevSTAB.6.030702. URL: https://link.aps.org/doi/10.1103/PhysRevSTAB.6.030702.

[7] O. A. Shevchenko et al. "The Novosibirsk free electron laser facility". In: **AIP Conference Proceedings**. Vol. 2299. November. 2020, p. 020001. ISBN: 9780735440333. DOI: 10.1063/5.0031513. URL: http://aip.scitation.org/doi/abs/10.1063/5.0031513.

[8] Michaela Arnold et al. "First operation of the superconducting Darmstadt linear electron accelerator as an energy recovery linac". In: **Physical Review Accelerators and Beams** 23.2 (2020), p. 20101. ISSN: 24699888. DOI: 10.1103/PhysRevAccelBeams.23.020101. URL: https://doi.org/10.1103/PhysRevAccelBeams.23.020101.

[9] A. Bartnik et al. "CBETA: First Multipass Superconducting Linear Accelerator with Energy Recovery". In: **Physical Review Letters** 125.4 (2020), pp. 1–5. ISSN: 10797114. DOI: 10.1103/PhysRevLett.125.044803.

[10] Mitsuo Akemoto et al. "Construction and commissioning of the compact energy-recovery linac at KEK". In: **Nuclear Instruments and Methods in Physics Research Section A: Accelerators, Spectrometers, Detectors and Associated Equipment** 877.September 2015 (Jan. 2018), pp. 197–219. ISSN: 01689002. DOI: 10.1016/j.nima.2017.08.051. URL: http://dx.doi.org/10.1016/j.nima.2017.08.051%20https://linkinghub.elsevier.com/retrieve/pii/S0168900217309518.

[11] Takashi Obina et al. "1 mA STABLE ENERGY RECOVERY BEAM OPERATION WITH SMALL BEAM EMITTANCE". In: **Proc. 10th International Particle Accelerator Conference (IPAC'19)**. Melbourne, Australia: JACOW Publishing, Geneva, Switzerland, 2019, pp. 1482–1485. ISBN: 9783954502080. DOI: 10.18429/JACoW-IPAC2019-TUPGW036. URL: http://jacow.org/IPAC2018/papers/frzplm2.pdf.

[12] S. Friederich, K. Aulenbacher, and C. Matejcek. "STATUS OF THE POLARIZED SOURCE AND BEAM PREPARATION SYSTEM AT MESA". In: **Proceedings of IPAC2021**. JACOW Publishing, Geneva, Switzerland, 2021, pp. 2736–2739. ISBN: 9783954502141. DOI: 10.18429/JACoW-IPAC2021-WEPAB063. URL: https://www.jacow.org/IPAC2021/papers/WEPAB063.pdf.

[13] S A Bogacz et al. **ER@CEBAF: A test of 5-pass energy recovery at CEBAF**. Tech. rep. June. Upton, NY (United States): Brookhaven National Laboratory (BNL), June 2016. DOI: 10.2172/1336057. URL: http://www.osti.gov/servlets/purl/1336057/.

[14] Michael Abo-Bakr et al. **Conceptual Design Report BERLinPro**. Tech. rep. 2012.

[15] Ferdinand Willeke and J. Beebe-Wang. **Electron Ion Collider Conceptual Design Report 2021**. Tech. rep. February. Upton, NY (United States): Brookhaven National Laboratory (BNL), Feb. 2021. DOI: 10.2172/1765663. URL: https://www.osti.gov/servlets/purl/1765663/.

[16] D. Angal-Kalinin et al. "PERLE. Powerful energy recovery linac for experiments. Conceptual design report". In: **Journal of Physics G: Nuclear and Particle Physics** 45.6 (June 2018), p. 065003. ISSN: 0954-3899. DOI: 10.1088/1361-6471/aaa171. URL: https://iopscience.iop.org/article/10.1088/1361-6471/aaa171.

[17] Vladimir N. Litvinenko, Thomas Roser, and Maria Chamizo-Llatas. "High-energy high-luminosity e+e- collider using energy-recovery linacs". In: **Physics Letters, Section B: Nuclear, Elementary Particle and High-Energy Physics** 804 (2020), p. 135394. ISSN: 03702693. DOI: 10.1016/j.physletb.2020.135394. URL: https://doi.org/10.1016/j.physletb.2020.135394.

[18] LHeC and FCC-he Study Group. **The Large Hadron-Electron Collider at the HL-LHC**. Tech. rep. 2020.

[19] V. I. Telnov. "A high-luminosity superconducting twin e+e- linear collider with energy recovery". In: **International Workshop on Future Linear Colliders, LCWS 2021** (2021). ISSN: 17480221. DOI: 10.1088/1748-0221/16/12/P12025.

[20] C. Curatolo and L. Serafini. "GeV muon beams with picometer-class emittance from electron-photon collisions". In: Cm (2021), pp. 1–8. URL: http://arxiv.org/abs/2106.03255.

[21] B.S. Schlimme et al. "Operation and characterization of a windowless gas jet target in high-intensity electron beams". In: **Nuclear Instruments and Methods in Physics Research Section A: Accelerators, Spectrometers, Detectors and Associated Equipment** 1013.April (Oct. 2021), p. 165668. ISSN: 01689002. DOI: 10.1016/j.nima.2021.165668. URL: https://doi.org/10.1016/j.nima.2021.165668%20https://linkinghub.elsevier.com/retrieve/pii/S0168900221006537.

[22] Z. Nergiz et al. "Bright Ångstrom and picometer free electron laser based on the Large Hadron electron Collider energy recovery linac". In: **Physical Review Accelerators and Beams** 24.10 (2021), p. 100701. ISSN: 24699888. DOI: 10.1103/PhysRevAccelBeams.24.100701. URL: https://doi.org/10.1103/PhysRevAccelBeams.24.100701.

[23] Ilan Ben-Zvi. "Superconducting energy recovery linacs". In: **Superconductor Science and Technology** 29.10 (2016). ISSN: 13616668. DOI: 10.1088/0953-2048/29/10/103002.

[24] Sara Thorin et al. "The MAX IV Linac". In: **Linac2014** (2014), TUIOA03. URL: http://accelconf.web.cern.ch/AccelConf/LINAC2014/papers/tuioa03.pdf%0Ahttp://inspirehep.net/record/1363410/.

[25] J Andersen et al. "The Soft X-Ray Laser Project At MAX IV". In: **Proceedings of IPAC2017, Copenhagen, Denmark** (2017), pp. 3–5.

[26] Weilun Qin et al. "The FEL in the SXL project at MAX IV". In: **Journal of Synchrotron Radiation** 28 (2021), pp. 707–717. ISSN: 16005775. DOI: 10.1107/S1600577521003465.

[27] H.A. Grunder et al. "The continuous electron beam accelerator facility". In: vol. 478. Feb. 1988, pp. 831–846. DOI: 10.1016/0375-9474(88)90921-9. URL: https://linkinghub.elsevier.com/retrieve/pii/0375947488909219.

[28] A. Freyberger. "Commissioning and operation of 12GeV CEBAF". In: **6th International Particle Accelerator Conference, IPAC 2015** (2015), pp. 1–5. DOI: 10.18429/JACoW-IPAC2015-MOXGB2.

[29] David Douglas. "A Generic Energy-Recovering Bisected Asymmetric Linac (GERBAL)". In: **Beam Dynamics Newsletter** ICFA-BD-NL (2001), pp. 40–45. URL: https://icfa-usa.jlab.org/archive/newsletter/icfa_bd_nl_26.pdf.

[30] Peter H. Williams et al. "Recirculating linac free-electron laser driver". In: **Physical Review Special Topics - Accelerators and Beams** 14.5 (May 2011), p. 050704. ISSN: 1098-4402. DOI: 10.1103/PhysRevSTAB.14.050704. URL: https://link.aps.org/doi/10.1103/PhysRevSTAB.14.050704.

[31] R. C. York. "5 upgradable to 25 keV free electron laser facility". In: **Physical Review Special Topics - Accelerators and Beams** 17.1 (Jan. 2014), p. 010705. ISSN: 1098-4402. DOI: 10.1103/PhysRevSTAB.17.010705. URL: http://link.aps.org/doi/10.1103/PhysRevSTAB.17.010705%20https://link.aps.org/doi/10.1103/PhysRevSTAB.17.010705.

[32] Andrew Burnett et al. **UK-XFEL Science Case**. 2020.

[33] Dario Pellegrini et al. "Beam-dynamics driven design of the LHeC energy-recovery linac". In: **Physical Review Special Topics - Accelerators and Beams** 18.12 (Dec. 2015), p. 121004. ISSN: 1098-4402. DOI: 10.1103/PhysRevSTAB.18.121004. URL: https://link.aps.org/doi/10.1103/PhysRevSTAB.18.121004.

[34] K D J André et al. "STUDIES OF THE ENERGY RECOVERY PERFORMANCE OF THE PERLE PROJECT". In: **Proceedings of IPAC2021**. JACoW Publishing, 2021, pp. 2744–2747. ISBN: 9783954502141. DOI: 10.18429/JACoW-IPAC2021-WEPAB065. URL: https://www.jacow.org/IPAC2021/papers/WEPAB065.pdf.

[35] Andrei Seryi. **Unifying Physics of Accelerators, Lasers and Plasma**. Vol. 21. 2. CRC Press, July 2015. DOI: 10.1201/b18696. URL: https://www.taylorfrancis.com/books/9781482240597.

[36] A. Cianchi et al. "Challenges in plasma and laser wakefield accelerated beams diagnostic". In: **Nuclear Instruments and Methods in Physics Research, Section A: Accelerators, Spectrometers, Detectors and Associated Equipment** 720 (2013), pp. 153–156. ISSN: 01689002. DOI: 10.1016/j.nima.2012.12.012. URL: http://dx.doi.org/10.1016/j.nima.2012.12.012.

[37] M. Migliorati et al. "Intrinsic normalized emittance growth in laser-driven electron accelerators". In: **Physical Review Special Topics - Accelerators and Beams** 16.1 (2013), pp. 1–5. ISSN: 10984402. DOI: 10.1103/PhysRevSTAB.16.011302.

[38] Karl L. Brown and Roger V. Servranckx. "First- and second-order charged particle optics". In: **AIP Conference Proceedings**. Vol. 127. July. 1984, pp. 62–138. DOI: 10.1063/1.35177.

[39] V. Balandin et al. "Apochromatic Beam Transport in Drift-Quadrupole Systems". In: **Proceedings of IPAC'10, Kyoto, Japan**. May 2013, pp. 4476–4478. ISBN: 9789290833529. URL: https://accelconf.web.cern.ch/IPAC10/papers/thpd083.pdf.

[40] C. A. Lindstrøm and E. Adli. "Design of general apochromatic drift-quadrupole beam lines". In: **Physical Review Accelerators and Beams** 19.7 (July 2016), p. 071002. ISSN: 2469-9888. DOI: 10.1103/PhysRevAccelBeams.19.071002. URL: https://link.aps.org/doi/10.1103/PhysRevAccelBeams.19.071002.

[41] David Robin et al. "Quasi-isochronous storage rings". In: **Nuclear Inst. and Methods in Physics Research, A** 48 (1993). ISSN: 01689002. DOI: 10.1016/0168-9002(91)90734-8.

[42] Peter H. Williams et al. "Arclike variable bunch compressors". In: **Physical Review Accelerators and Beams** 23.10 (2020), pp. 1–8. ISSN: 24699888. DOI: 10.1103/PhysRevAccelBeams.23.100701.

[43] Karl L. Brown. **A First- and Second-Order Matrix Theory for the Design of Beam Transport Systems and Charged Particle Spectrometers**. Tech. rep. Stanford Linear Accelerator Center, Calif., 1982.

[44] S. Thorin et al. "Bunch compression by linearising achromats for the MAX IV Injector". In: **FEL 2010 - 32nd International Free Electron Laser Conference**. 2010, pp. 471–474. URL: https://epaper.kek.jp/FEL2010/papers/wepb34.pdf.

[45] Hywel L. Owen and Peter H. Williams. "A modular path length corrector for recirculating linacs". In: **Nuclear Instruments and Methods in Physics Research, Section A: Accelerators, Spectrometers, Detectors and Associated Equipment** (2012). ISSN: 01689002. DOI: 10.1016/j.nima.2011.09.043.

[46] S. Di Mitri and M. Cornacchia. "Electron beam brightness in linac drivers for free-electron-lasers". In: **Physics Reports** 539.1 (2014), pp. 1–48. ISSN: 03701573. DOI: 10.1016/j.physrep.2014.01.005. URL: http://dx.doi.org/10.1016/j.physrep.2014.01.005.

[47] Nils Martensson and Mikael Eriksson. "The saga of MAX IV, the first multi-bend achromat synchrotron light source". In: **Nuclear Instruments and Methods in Physics Research, Section A: Accelerators, Spectrometers, Detectors and Associated Equipment** 907.March (2018), pp. 97–104. ISSN: 01689002. DOI: 10.1016/j.nima.2018.03.018. URL: https://doi.org/10.1016/j.nima.2018.03.018.

[48] Brian William Montague. **Linear Optics for Improved Chromaticity Correction**. 1979. URL: https://cds.cern.ch/record/443342/files/cern-lep-note%20165.pdf.

[49] K. Flöttmann, T. Limberg, and Ph. Piot. "Generation of Ultrashort Electron Bunches by cancellation of nonlinear distortions in the longitudinal phase space". In: **TESLA-FEL Reports** 2001-06 (2001).

[50] Fengfeng Qi et al. "Breaking 50 Femtosecond Resolution Barrier in MeV Ultrafast Electron Diffraction with a Double Bend Achromat Compressor". In: **Physical Review Letters** 124.13 (2020), p. 134803. ISSN: 10797114. DOI: 10.1103/PhysRevLett.124.134803. URL: https://doi.org/10.1103/PhysRevLett.124.134803.

[51] Hyun Woo Kim et al. "Towards jitter-free ultrafast electron diffraction technology". In: **Nature Photonics** 14.4 (2020), pp. 245–249. ISSN: 17494893. DOI: 10.1038/s41566-019-0566-4. URL: http://dx.doi.org/10.1038/s41566-019-0566-4.

[52] Jonas Björklund Svensson et al. "Third-order double-achromat bunch compressors for broadband beams". In: **Physical Review Accelerators and Beams** 22.10 (2019), p. 104401. ISSN: 24699888. DOI: 10.1103/PhysRevAccelBeams.22.104401. URL: https://doi.org/10.1103/PhysRevAccelBeams.22.104401.

[53] Michael Borland, John Lewellen, and Steve Milton. "A Highly Flexible Bunch Compressor for the APS LEUTL FEL". In: (2000), pp. 8–10. URL: http://arxiv.org/abs/physics/0008114.

[54] A. Streun. "The anti-bend cell for ultralow emittance storage ring lattices". In: **Nuclear Instruments and Methods in Physics Research, Section A: Accelerators, Spectrometers, Detectors and Associated Equipment** 737 (2014), pp. 148–154. ISSN: 01689002. DOI: 10.1016/j.nima.2013.11.064. URL: http://dx.doi.org/10.1016/j.nima.2013.11.064.

[55] B. Riemann and A. Streun. "Low emittance lattice design from first principles: Reverse bending and longitudinal gradient bends". In: **Physical Review Accelerators and Beams** 22.2 (Feb. 2019). ISSN: 24699888. DOI: 10.1103/PhysRevAccelBeams.22.021601.

[56] Gustavo Pérez Segurana, Ian R. Bailey, and Peter H. Williams. "Construction of self-consistent longitudinal matches in multipass energy recovery linacs". In: **Physical Review Accelerators and Beams** 25.2 (Feb. 2022), p. 021003. ISSN: 2469-9888.

DOI: 10.1103/PhysRevAccelBeams.25.021003. URL: https://link.aps.org/doi/10.1103/PhysRevAccelBeams.25.021003.

[57] S. Benson et al. "First lasing of the Jefferson Lab IR Demo FEL". In: **Nuclear Instruments and Methods in Physics Research, Section A: Accelerators, Spectrometers, Detectors and Associated Equipment** 429.1 (1999), pp. 27–32. ISSN: 01689002. DOI: 10.1016/S0168-9002(99)00061-3. URL: https://www.osti.gov/biblio/791572.

[58] Matthew Sands. **PHYSICS OF ELECTRON STORAGE RINGS: AN INTRODUCTION.** Tech. rep. U.S. Atomic Energy Commission: Divison of Technical Information Extension, Jan. 1970, pp. 257–411. DOI: 10.2172/4064201. URL: http://www.osti.gov/servlets/purl/4064201/.

[59] S. Setiniyaz, R. Apsimon, and P. H. Williams. **Implications of beam filling patterns on the design of recirculating energy recovery linacs**. July 2020. DOI: 10.1103/PHYSREVACCELBEAMS.23.072002. URL: https://link.aps.org/doi/10.1103/PhysRevAccelBeams.23.072002.

[60] S. Setiniyaz, R. Apsimon, and P. H. Williams. "Filling pattern dependence of regenerative beam breakup instability in energy recovery linacs". In: **Physical Review Accelerators and Beams** 24.6 (2021), p. 61003. ISSN: 24699888. DOI: 10.1103/PhysRevAccelBeams.24.061003. URL: https://doi.org/10.1103/PhysRevAccelBeams.24.061003.

[61] R Ainsworth et al. "Asymmetric dual axis energy recovery linac for ultrahigh flux sources of coherent x-ray and THz radiation: Investigations towards its ultimate performance". In: **Physical Review Accelerators and Beams** 19.8 (Aug. 2016), p. 083502. ISSN: 2469-9888. DOI: 10.1103/PhysRevAccelBeams.19.083502. URL: https://link.aps.org/doi/10.1103/PhysRevAccelBeams.19.083502.

[62] I. V. Konoplev et al. "Ultimate energy recovery from spent relativistic electron beam in energy recovery linear accelerators". In: **Physical Review Accelerators and Beams** 23.7 (2020), p. 71601. ISSN: 24699888. DOI: 10.1103/PHYSREVACCELBEAMS.

23 . 071601. URL: https : / / doi . org / 10 . 1103 / PhysRevAccelBeams . 23 . 071601.

[63] R. Koscica et al. "Energy and rf cavity phase symmetry enforcement in multiturn energy recovery linac models". In: **Physical Review Accelerators and Beams** 22.9 (Sept. 2019). ISSN: 24699888. DOI: 10 . 1103 / PhysRevAccelBeams . 22 . 091602.

[64] F. Méot et al. "ER @ CEBAF - A HIGH-ENERGY , MULTIPLE-PASS ENERGY RECOVERY EXPERIMENT AT CEBAF". In: **IPAC 2016 - Proceedings of the 7th International Particle Accelerator Conference**. JACOW Publishing, Geneva, Switzerland, 2016, pp. 1022–1024. ISBN: 978-3-95450-147-2. DOI: 10 . 18429 / JACoW - IPAC2016 - TUOBA02. URL: http : / / jacow . org / ipac2016 / papers / tuoba02.pdf.

[65] C.-Y. Tsai et al. "Conditions for coherent-synchrotron-radiation-induced microbunching suppression in multibend beam transport or recirculation arcs". In: **Physical Review Accelerators and Beams** 20.2 (Feb. 2017), p. 024401. ISSN: 2469-9888. DOI: 10.1103/PhysRevAccelBeams.20.024401. URL: http://link.aps.org/doi/10.1103/PhysRevAccelBeams.20.024401.

[66] Igor Zagorodnov and Martin Dohlus. "Semianalytical modeling of multistage bunch compression with collective effects". In: **Physical Review Special Topics - Accelerators and Beams** 14.1 (2011), pp. 1–17. ISSN: 10984402. DOI: 10.1103/PhysRevSTAB.14.014403.

[67] K.L.F. Bane and P. Emma. "Litrack: A Fast Longitudinal Phase Space Tracking Code with Graphical User Interface". In: **Proceedings of the 2005 Particle Accelerator Conference**. Vol. 2005. IEEE, 2005, pp. 4266–4268. ISBN: 0-7803-8859-3. DOI: 10.1109/PAC.2005.1591786. URL: http://ieeexplore.ieee.org/document/1591786/.

[68] I.V. Konoplev et al. "Concept of circular-linear energy recovery accelerator to probe the energy frontier". In: **Journal of Instrumentation** 17.01 (Jan. 2022), P01011.

ISSN: 1748-0221. DOI: 10.1088/1748-0221/17/01/P01011. URL: https://iopscience.iop.org/article/10.1088/1748-0221/17/01/P01011.

[69] T. K. Charles, D. M. Paganin, and R. T. Dowd. "Caustic-based approach to understanding bunching dynamics and current spike formation in particle bunches". In: **Physical Review Accelerators and Beams** 19.10 (Oct. 2016), p. 104402. ISSN: 2469-9888. DOI: 10.1103/PhysRevAccelBeams.19.104402. URL: https://link.aps.org/doi/10.1103/PhysRevAccelBeams.19.104402.

[70] T. K. Charles et al. "Current-horn suppression for reduced coherent-synchrotron-radiation-induced emittance growth in strong bunch compression". In: **Physical Review Accelerators and Beams** 20.3 (Mar. 2017), p. 030705. ISSN: 2469-9888. DOI: 10.1103/PhysRevAccelBeams.20.030705. URL: http://link.aps.org/doi/10.1103/PhysRevAccelBeams.20.030705.

[71] A. Khan et al. "Beam matching with space charge in energy recovery linacs". In: **Nuclear Instruments and Methods in Physics Research Section A: Accelerators, Spectrometers, Detectors and Associated Equipment** 948.July (Dec. 2019), p. 162822. ISSN: 01689002. DOI: 10.1016/j.nima.2019.162822. URL: https://doi.org/10.1016/j.nima.2019.162822.

[72] D Douglas and P Williams. **How To (At Least) Double CEBAF Arc Momentum Acceptance**. Tech. rep. March. 2017.

[73] E. A. Schneidmiller and M. V. Yurkov. "Baseline parameters of the European XFEL". In: **Proceedings of the 38th International Free-Electron Laser Conference, FEL 2017**. JACOW Publishing, Geneva, Switzerland, 2018, pp. 109–112. ISBN: 978-3-95450-179-3. DOI: 10.18429/JACoW-FEL2017-MOP033.

[74] B Hounsell et al. "OPTIMIZATION OF A HIGH BUNCH CHARGE ERL INJECTION MERGER FOR PERLE". In: **Proceedings of IPAC2021** (2021), pp. 3983–3986. DOI: 10.18429/JACoW-IPAC2021-THPAB106. URL: https://www.jacow.org/IPAC2021/papers/THPAB106.pdf.